

The Effects of Curvature on Axial Flux Machine Cores

by

Andrew John Hewitt, B.Eng (Hons)

Dissertation

Submitted in Fulfillment

of the Requirements

for the Degree of

Doctor of Philosophy

at the

The University of Southern Queensland

Faculty of Engineering & Surveying

May 2005

Copyright

by

Andrew John Hewitt

2005

Abstract

This work is an investigation into the curvature related potential for flux to flow in the radial direction in the back-iron of laminated axial flux machine cores. Analytical and numerical models are presented. Analysis based on these models has shown that, in practical axial flux machines, the radial component of the flux density can be neglected with respect to the flux density distribution in the core back-iron. It has also been found that if the core permeability, core conductivity and number of poles are sufficiently high then power loss due to curvature related cross-lamination flux is negligible compared to normal eddy current losses. A closed form expression to predict losses due to curvature related radial flux is also presented. This expression allows axial flux machine designers to make quick assessment of the need to consider these losses when designing axial flux machines.

Certification of Thesis

I certify that the ideas, experimental work, results, analyses, software and conclusions reported in this dissertation are entirely my own effort, except where otherwise acknowledged. I also certify that the work is original and has not been previously submitted for any other award, except where otherwise acknowledged.

Signature of Candidate

Date

ENDORSEMENT

Signature of Supervisors

Date

Acknowledgments

I would sincerely like to thank and acknowledge the following people for their assistance, guidance and support throughout the duration of this project.

First of all I would like to thank my supervisor Dr Tony Ahfock. This study would not have been possible without his continued guidance, support and advice. Throughout the duration of this project he has been extremely patient, inspiring and has been a pleasure to work with.

I am also very grateful to Dr Sergey Suslov for his continued support, interest and assistance in this project. Without his support and advice some of this work would not have been completed.

I wish to thank the Faculty of Engineering and Surveying and the Office of Research and Higher Degrees for their support and assistance. My thanks also extends to all those at the university who made this such a pleasant experience.

Finally, I wish to thank my wife Elizabeth and my family for their continued support and encouragement.

Contents

Abstract	iii
Certification of Thesis	iv
Acknowledgments	v
List of Tables	x
List of Figures	xi
List of Symbols	xiv
Chapter 1 Introduction	1
1.1 Axial Flux Machines	1
1.2 Curvature related radial flux	3
1.3 Research Aims and Objectives	6
1.4 Literature Review	7
1.5 Dissertation Outline	9
1.6 Summary of Original Work	12
1.7 Publications	14
1.7.1 Publications:	14
1.7.2 Acknowledgement of Contributions by Co-Authors	14
Chapter 2 Curvature Related Radial Flux in Axial Flux Machine Cores	16

2.1	Analytical Model	17
2.1.1	Single-Phase Excitation	17
2.1.2	Three-Phase Excitation (Rotating Fields)	23
2.1.3	Air-gap Flux Density Distribution	24
2.1.4	The Effect of Curvature on the Radial Flux Density	25
2.2	Predicted Core Magnetic Flux Density Distribution	27
2.2.1	Experimental Results	30
2.2.2	Practical Implications	32
Chapter 3 The Coupled Network Method		35
3.1	Magnetostatic Analysis without Currents	37
3.1.1	The Permeance Matrix	39
3.1.2	Imposed Magnetic Flux	40
3.1.3	Solving the System of Equations	41
3.2	Eddy Current Analysis using the Coupled Network Method	42
3.2.1	Alternate Formulation	49
3.2.2	Postprocessing	50
3.3	Coupled Networks and the Finite Difference Method	51
3.3.1	Node Equations	52
3.3.2	Boundary Conditions	59
3.3.3	Loop Currents and the Electric Vector Potential	63
3.3.4	Comparing Formulations	64
3.4	Axiperiodic Formulation	65
3.4.1	The Magnetic Node Equation	65
3.4.2	The Electric Loop Equation	69
3.4.3	The Axiperiodic System of Equations	72

3.4.4	Calculating Induced Losses	73
Chapter 4	Core Losses and Magnetic Flux Density Distribution	76
4.1	Eddy Current Loss Separation	77
4.2	Main Flux Loss Prediction	79
4.3	Coupled Network Loss Prediction	83
4.4	Closed Form Expression for Power Loss	87
4.4.1	Rotating Fields	91
4.5	Laboratory Tests	94
4.6	Flux Density Distribution	97
4.7	Practical Axial Flux Machines	101
Chapter 5	Sub-domain Scaling for Finite Element Analysis of Electrical Machines	102
5.1	Finite Element Analysis and Scaling	103
5.1.1	The Finite Element Mesh	103
5.1.2	Quasi-Static Formulation	105
5.2	Scaling Equations	106
5.2.1	Axial Scaling	107
5.2.2	Axial Scaling Transformations	108
5.2.3	Energy and Power Invariance	115
5.2.4	Material Non-Linearity	115
5.3	Node and Element Reduction using the Axial Scaling Technique	116
Chapter 6	Conclusions	120
6.1	Curvature Related Radial Flux	121
6.2	Losses due to Radial Flux	121
6.3	Magnetic Flux Density Distribution	122
6.4	Sub-domain Scaling for Finite Element Analysis of Electric Machines	123

6.5 Further Work	124
References	126
Appendix A Bessel Function Orthogonality	132
Appendix B Air-Gap Flux Density Distribution	135
B.1 Air-Gap Magnetic Flux Density	135
B.2 Narrow Air-Gaps	141
Appendix C Two-Dimensional Magnetostatic Model	142
Appendix D Proof of Sinusoidal Periodicity in the Circumferential Direction	146
Appendix E The Circumferential and Axial Components of: $\nabla \times \sigma^{-1} \nabla \times \vec{T} = -j\omega \left[\mu \left(\vec{T} \times \nabla \Omega \right) \right]$	150
Appendix F Published Papers	153

List of Tables

4.1	Power loss due to cross-lamination flux.	84
4.2	Power losses due to main flux.	85
4.3	Comparison between power loss (F) predicted by equation (4.30) and that predicted by the axiperiodic coupled network method.	90
5.1	Axial Scaling Transformations	113
5.2	Axial Scaling Transformations continued	114

List of Figures

1.1	Main flux path in an axial and radial flux machine.	2
1.2	Axial Flux machine topologies.	3
1.3	Magnetic flux paths for zero radial flux (ACB) and significant radial flux (AB).	4
1.4	Magnetic flux path lengths at different radii.	6
1.5	Magnetic flux entering the core at different radii (the amount of flux being proportional to the shaded area).	6
2.1	Stator core geometry and coordinate system.	18
2.2	Solutions to the non-linear eigenvalue problem.	21
2.3	Integration contours for Amperes law.	24
2.4	The effect of curvature on the peak radial flux density.	26
2.5	Error in the truncated infinite series of equation (2.26).	28
2.6	Analytically predicted radial component of flux density along a pole-centre plane.	29
2.7	Normalised circumferential flux densities through planes half way between pole centre planes.	29
2.8	Experimental set-up.	30
2.9	Test-core voltage measurement.	31
2.10	Measured and predicted circumferential flux.	32
2.11	Normalised circumferential flux density found using the 2D and 3D models.	33

3.1	Core discretization.	38
3.2	Element shape and node position.	38
3.3	Element structure and associate permeance branches.	39
3.4	Radial permeance branches with their associated loop currents.	43
3.5	Norton equivalent circuit	43
3.6	Element structure including both the magnetic and electric networks.	45
3.7	Permeance branch and its associated loop current.	45
3.8	Permeance branch with its loop current replaced by an equivalent branch mmf.	46
3.9	Permeance branch and its modified node scalar potentials.	47
3.10	A general electric loop structure.	48
3.11	Radial connected permeance branches and their branch magnetic flux.	51
3.12	Permeance branches with their associated loop currents.	55
3.13	Relative positioning of elements.	58
3.14	Magnetic boundary conditions.	59
3.15	Axial symmetry plane and discretisation	66
3.16	Element structure.	66
3.17	r - z plane node configuration and permeance connections.	67
3.18	Electric network.	70
3.19	Branch current calculation.	73
4.1	Cross-section of a lamination sheet.	78
4.2	Lamination sheet cross-section.	80
4.3	Plot of integrand of equation (4.20).	82
4.4	Dependence of power loss on frequency.	84
4.5	Circumferential current distribution (integrated from r_i to r_o) along a pole centre plane (2-pole machine).	86
4.6	Circumferential current crossing the pole-centre plane in one direction.	86

4.7	Simplified representation of an axial flux machine core.	87
4.8	Core radial divisions used to derive a closed form loss equation.	89
4.9	Determination of k from hypothetical experimental data.	95
4.10	Experimental results ($\hat{B}_z = 0.5\text{T}$).	96
4.11	Experimental set-up for measuring core losses.	97
4.12	Normalised average radial flux density along a pole-centre plane.	99
4.13	Normalised average circumferential flux density half way between pole-centre planes.	100
5.1	Finite element 2D mesh	104
5.2	Axial scaling sub-domains.	107
5.3	Finite element mesh of a 2D geometry with narrow air-gap region.	117
5.4	Finite element mesh of a 2D geometry with scaled ($\times 5$) air-gap region.	117
5.5	3D model of the iron cores and air-gap region.	118
5.6	Finite element mesh of the geometry of Figure 5.5.	118
5.7	3D model of the iron cores and scaled ($\times 5$) air-gap region.	119
5.8	Finite element mesh of the geometry of Figure 5.7.	119

List of Symbols

Chapter 2

a	core inner radius
b	core outer radius
B'	magnetic flux density
H'	magnetic field intensity
J_m	Bessel function of the first kind of order m
k_θ	ratio of circumferential to radial permeability
k_z	ratio of axial to radial permeability
k_n	Solutions to the non-linear eigenvalue problem of equation (2.21)
l	the number of machine poles divided by two
l_g	air gap axial length
M	non-dimensional permeability tensor
M'	permeability tensor
p	the number of machine poles
P	peak imposed magnetic flux density
r'	radius
t	time in seconds
Y_m	Bessel function of the second kind of order m
'	denotes physical values or quantities

r	denotes the radial direction or component
θ	denotes the circumferential direction or component
z	denotes the axial direction or component
δ	core axial length
μ	material permeability
ϕ'	magnetic scalar potential
ϕ	non-dimensional magnetic scalar potential
ϕ_0	characteristic value of the magnetic scalar potential
ω	angular velocity in rad/s

Chapter 3

A	cross sectional area
B	magnetic flux density
\hat{B}_z	peak axial magnetic flux injection
E	electric field intensity
H	magnetic field intensity
I	loop current
\mathbf{I}	vector of loop currents
J	electric current density
l	path length
p	the number of machine poles
\mathbf{P}	permeance matrix
\mathbf{Q}	connectivity matrix
r	radius
r_i	element inner radius
r_i	core inner radius
r_o	element outer radius
r_o	core outer radius

\tilde{r}	element average radius
R	electric resistance
\mathbf{R}	matrix of electric resistance values
\mathbf{S}	matrix of permeances
$\tilde{\mathbf{S}}$	$j\omega\mathbf{S}$
t	time
T	electric vector potential
\mathbf{V}	vector of induced loop voltages
\mathbf{W}	matrix of permeances
$\tilde{\mathbf{W}}$	$j\omega\mathbf{W}$
r	denotes the radial direction or component
θ	denotes the circumferential direction or component
z	denotes the axial direction or component
'	denote values in the limit $\Delta\theta \rightarrow 0$
δ	core axial length
Δ	denotes elemental values
θ	angular position
μ	material permeability
ρ	branch permeance
ρ_{ro}	radial branch permeance at the element outer radius
ρ_{ri}	radial branch permeance at the element inner radius
σ	material conductivity
Φ_{imp}	vector of imposed magnetic flux at the nodes
$\Phi_{induced}$	vector of induced magnetic flux due to induced currents
ϕ	branch magnetic flux
ϕ	vector of branch flux
Φ	imposed node magnetic flux

ω	angular velocity in rad/s
Ω	magnetic scalar potential
$\mathbf{\Omega}$	vector of magnetic scalar potentials

Chapter 4

a	core inner radius
b	core outer radius
B	magnetic flux density
\hat{B}	peak imposed magnetic flux density
D	power loss density
E	electric field intensity
f_m	characteristic frequency
F	classical eddy current loss due to cross lamination flux
F	core classical eddy current loss
F_p	time averaged classical eddy current loss density due to main flux
$F(t)$	instantaneous classical eddy current loss
J	induced current density
k	constant
$k_{z\theta}$	ratio of circumferential to axial permeability
p	number of machine poles
P	peak imposed magnetic flux density
P	branch permeance
P	period of the spatially varying field
P_T	total core loss
p	denotes due to parallel running flux
r	radius
R	resistance
R	denotes a rotating field

S	skin depth
t	lamine thickness
\vec{T}	electric vector potential
r	radial component
θ	circumferential component
z	axial component
δ	core axial length
σ	material conductivity
ϕ	magnetic flux
ω	angular velocity in rad/s
Ω	magnetic potential

Chapter 5

B	magnetic flux density
E	electric field intensity
f	transformation function
g	transformation function
H	magnetic field intensity
J	electric current density
k_s	scaling factor
l_g	air gap axial length
t	time
T	denotes a transformed quantity
V	volume
W	magnetic energy per unit volume
r	denotes the radial direction or component
θ	denotes the circumferential direction or component
z	denotes the axial direction or component

μ material permeability

σ material conductivity

Chapter 1

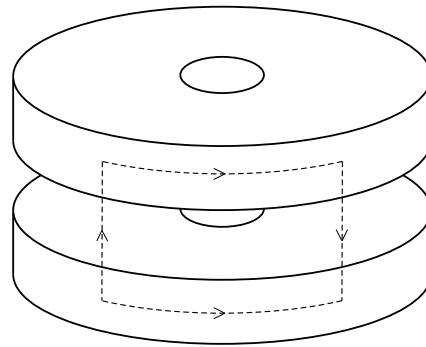
Introduction

1.1 Axial Flux Machines

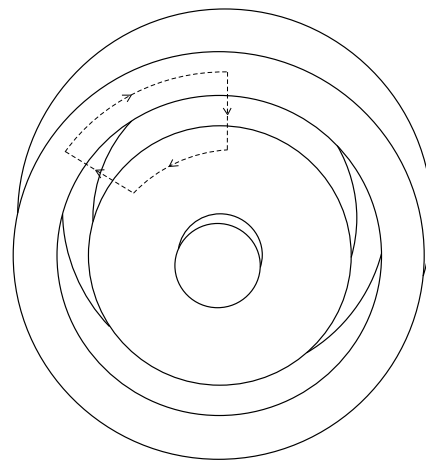
Although the vast majority of electrical motors are of the radial flux type, there is continued interest in axial flux machines (AFMs). The physical structure, especially the short axial length, gives AFMs an advantage in applications such as fans, disk drives, some electric vehicles and generators (Bumby et al., 2004; Patterson & Spee, 1995). There has also been claims that compared to radial flux machines (RFMs), AFMs have greater power to weight ratios (Brown et al., 2002; Bumby et al., 2004; Chan, 1987; Huang et al., 2002; Varga, 1986; Zhang et al., 1996).

The name “axial flux” machine comes from the fact that the air-gap flux in these machines is in the axial direction. Figure 1.1 shows a typical main flux path for both an axial and a radial flux machine.

One major disadvantage of the axial flux machine structure is the axial electromagnetic forces between the machine cores. Where necessary, multiple air-gap topologies can be used to overcome this problem with the added advantage of increasing the machine’s output per unit volume (Varga, 1986). A number of axial flux machine topologies have been proposed by authors such as Varga (1986) and Chan (1987), three of these are



(a) Main flux path in an axial flux machine.



(b) Main flux path in a radial flux machine.

Figure 1.1: Main flux path in an axial and radial flux machine.

shown in Figure 1.2.

The structure of axial flux machines is such that curvature is imposed on flux paths in the back-iron. This is also the case in radial flux machines (RFMs), however there is an important difference. In RFMs the direction of curvature is along the plane of the laminations whereas in AFMs the direction of curvature is perpendicular to the laminations. The effect of curvature on axial flux machine performance and behaviour has not been previously reported. It is now shown that core curvature can result in a radial component in the magnetic flux density distribution. This component has the potential to cause additional power loss in the core back-iron.

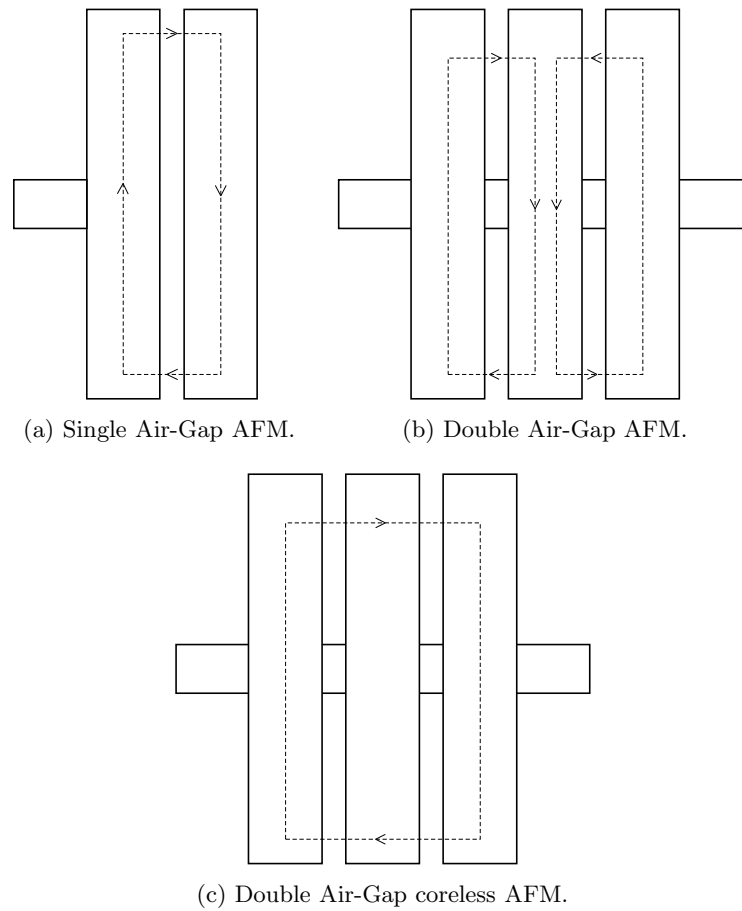


Figure 1.2: Axial Flux machine topologies.

1.2 Curvature related radial flux

Conventionally, design of axial flux machines assumes purely axial and circumferential flux flow within the laminated stator cores of the machine. This assumption implies that no radial and thus no cross lamination flux flow occurs within the machine back-iron. Investigation of flux distributions, based on the assumption of zero radial flux, results in a radially non-uniform distribution of circumferential flux. This non-uniform distribution would produce a potential for flux to flow in the radial direction which, if it occurs, would contradict the original assumption of zero radial flux flow. Thus there are three possible situations which can occur in the core back-iron:

- 1) no radial flux flows,

- 2) there is significant radial flux flow causing substantial circumferential flux redistribution. That is, the level of radial flux and its effects are such that they cannot be neglected,
- 3) the situation is somewhere between that of 1) and 2) but closer to 1). That is, there exists a radial component of flux density but its effects are small enough to be neglected.

A simplified representation of a magnetic flux path in an axial flux machine core is shown in Figure 1.3. The path ACB shown in Figure 1.3 represents situation 1) above. Substantial shortening of the flux path would occur in situation 2). This cannot happen without the existence of a radial component in the flux density. The tendency for magnetic flux to flow radially in the back-iron of AFMs does not seem to have been considered previously. The question then is whether or not the effects of a radial component of the magnetic flux density distribution can be ignored.

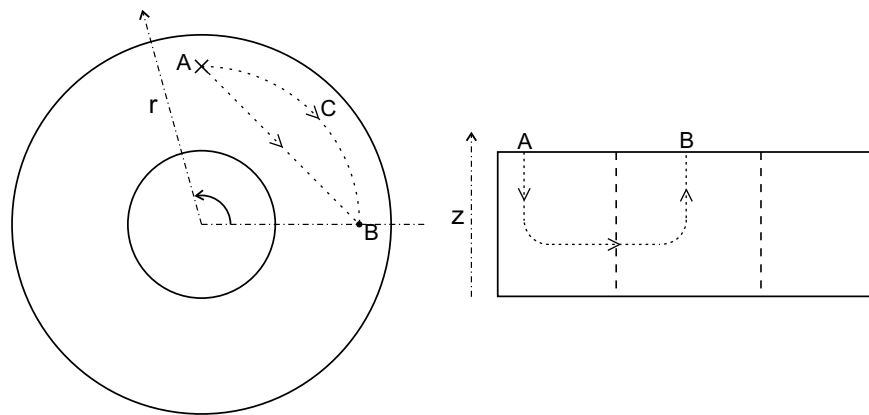


Figure 1.3: Magnetic flux paths for zero radial flux (ACB) and significant radial flux (AB).

The curvature related radial component of the magnetic flux density can be ignored only if its magnitude and distribution are such that:

- a) it does not cause significant additional losses due to induced eddy currents, and

- b) it does not have any significant influence on the distribution of both the circumferential and axial components of the flux density.

It seems likely that the above condition a) is satisfied in practice as there has been no theoretical or experimental work published which suggests that the laminated back-iron of AFMs suffers from noticeably higher iron losses. However, there is still a need for some theoretical basis to confirm this.

There are two main physical reasons why core curvature results in a radial component in the magnetic flux density distribution. First, flux paths are greater at larger radii due to longer circumferential arc-lengths, as shown in Figure 1.4. Second, if end effects are neglected then the magnetic flux enters the core from the air-gap axially with flux density constant in the radial direction and varying sinusoidally in the circumferential direction. As shown in Figure 1.5, this results in more flux entering the core at larger radii. These two factors produce a non-zero gradient of the magnetic potential in the radial direction. This potential may in turn cause a radial component in the flux density.

Whilst a laminated core is designed to reduce eddy current losses caused by flux flowing along the lamination planes, laminating cannot impede eddy currents caused by cross-lamination flux. Radial flux in an AFM core is cross-lamination flux and therefore can cause substantial amounts of eddy current to flow which may result in significant losses.

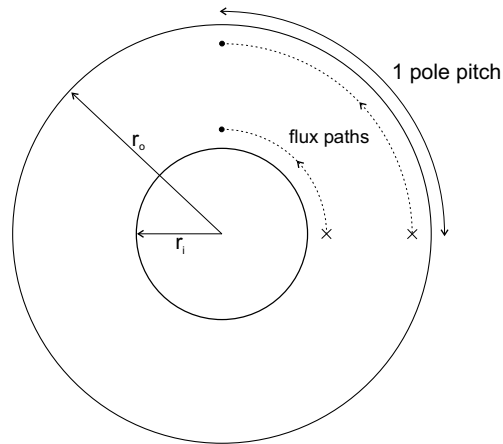


Figure 1.4: Magnetic flux path lengths at different radii.

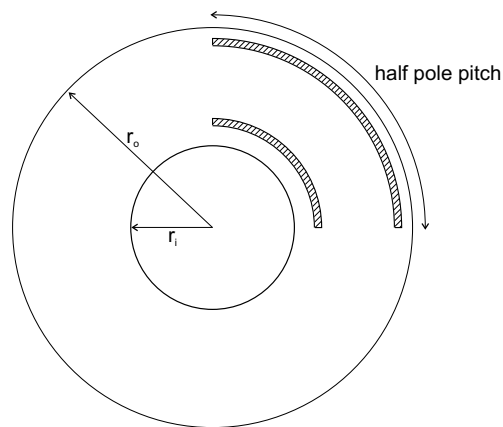


Figure 1.5: Magnetic flux entering the core at different radii (the amount of flux being proportional to the shaded area).

1.3 Research Aims and Objectives

Natural resources and energy savings relate directly to society's broader aims of sustainable living and curtailment of greenhouse gas emission. Electrical motors are significant consumers of fossil fuel generated energy and the search for lower cost but more efficient electrical motors is ongoing. Iron losses in electrical machines emanate as heat and thus influence machine efficiency and cooling requirements. Design of efficient machines

requires a thorough understanding of the loss and flux density distributions within a machine. This knowledge not only allows a machine designer to minimize losses but it can also result in savings in core materials.

With these broader goals in mind, the aim of this work was to develop mathematical models that would allow qualitative investigation of flux density and eddy current distributions in the back-iron of laminated axial flux machine cores.

Specific objectives were:

- 1) to develop an analytical model for a simplified axial flux machine core.
- 2) to develop a numerical model that would allow evaluation of power loss due to the tendency for flux to flow in the radial direction.
- 3) to design laboratory tests that would allow some of the predictions of 1) and 2) to be confirmed.

The rationale behind objective 1) was that an analytical model could be used to partially check the more practical model developed to fulfill the aim of objective 2).

1.4 Literature Review

A good understanding of the nature of the magnetic flux density distribution in the steel cores of axial flux machines would be an asset to engineers who are designing or analyzing these machines (Chandler & Patterson, 2001). Unfortunately, there is very little published work in this area. This is especially true for work that deals with the flux distribution in the back-iron of AFM cores. Some authors, (Bumby et al., 2004; Campbell, 1974; Chan, 1987; Zhilichev, 1998), have considered the flux density distribution in the air-gap region of AFMs, however flux densities in the iron cores have effectively been ignored since infinite core permeability was assumed. Boldea et al. (1975), derive expressions for the flux density in the air-gap and machine cores,

but ignore the effects of finite radius. Huang et al. (1999) derive sizing equations for AFMs with consideration of the core back-iron depth, which is a significant part of the axial length of AFMs. However, their approach seems to ignore non-uniformity in the flux density distribution in the back-iron.

Numerical techniques such as the finite difference and finite element methods have permitted machine designers to more accurately predict both flux and loss density distributions. Prediction of core losses in electric machines generally requires numerical quasi-static analysis. The finite element method has gained significant popularity over recent years and is possibly the most commonly used technique for electromagnetic analysis of electrical machines.

The difficulties in performing three-dimensional numerical analysis of electric machines are well known (Salon, 1995). This is especially true for machines with narrow air-gap regions (Abdel-Razek et al., 1982; DeBortoli et al., 1991; Feliachi et al., 1983; Guerin et al., 1994). In order to reduce the often significant computation times and resources required when performing finite element analysis of electrical machines, techniques such as the axisymmetric and axiperiodic formulations have been developed. These techniques, where applicable, have the potential to drastically reduce the problem size. Unfortunately, not all of these techniques are always available in commercial software packages.

Although not as popular as the finite element method, the use of coupled networks for electromagnetic analysis has also been widely reported on by authors such as Demenko (2000), Balchin & Davidson (1983), Davidson & Balchin (1983), Davidson & Balchin (1981), Balchin & Davidson (1980), Carpenter (1977), Carpenter (1975*a*), Carpenter (1975*b*), Carpenter (1975*c*), King (1966*a*) and King (1966*b*). From an engineering point of view, one significant advantage of this approach is the physical interpretation it readily lends itself to (Guo & Zhu, 2002; Carpenter, 1975*c*; King, 1966*a*).

The choice of technique used to solve a particular problem often depends on the problem type and characteristics as well as the availability of hardware and software resources.

Throughout most of this work, the “brute force” approach to numerical modeling was found to be unsuitable. This was primarily due to the three dimensional nature of the problem and limitations in available computing resources. As a result, it has been necessary to explore unconventional avenues in order to produce numerical models that were useful to the project.

1.5 Dissertation Outline

A brief outline of subsequent chapters is as follows:

Chapter 2 - The Effect of Curvature on Axial Flux Machine Cores, develops an analytical model of an axial flux machine core. This model confirms the presence of a curvature related radial component in the core magnetic flux density distribution. Three dimensional Finite Element Analysis is also performed to validate key results predicted by the analytical model.

The analytical model allows us to predict an upper limit for the magnitude of the radial flux component and determine its influence on the distribution of the axial and circumferential components of flux density in the core. It also provides some insight into the effects of varying physical dimensions and material properties on the flux density distribution in the core back-iron. The solution is an upper limit in the case of time-varying fields as induced currents will reduce the magnitude of the radial flux component.

Of practical significance is the prediction of greatest magnetic flux density in the circumferential direction in the laminations near the outer radius of the core. This should be taken into consideration if excessive saturation in this region of the core back-iron is to be avoided. Experimental results are presented which confirm the predictions of back-iron flux density distribution made by the model.

Chapter 3 - The Coupled Network Method, develops a coupled resistive-reluctive network for the purpose of predicting core losses due to radial flux flow in laminated cores. The periodicity of the fields in the circumferential direction in axial flux machine cores allows the core to be modeled using an axiperiodic formulation. Using this formulation has the significant advantage of reducing the problem size and thus the computation resources required to numerically model the core. The formulation presented is based on the magnetic scalar potential and a reduced electric vector potential. The term “reduced” is introduced to signify that only one of the components of the electric vector potential are non-zero.

The axiperiodic formulation is not widely available in commercial finite element software packages. Therefore, in order to exploit its advantages, all models were developed in-house. The coupled network method with regular elements was chosen because of the simple geometry of the core and because it lends itself to physical interpretation.

It is also shown that the coupled network formulation presented here is really just an application of the finite difference method.

Chapter 4 - Core Losses and Magnetic Flux Density Distribution, uses the restricted axiperiodic coupled network method developed in Chapter 3 to predict core losses due to the radial component of the magnetic flux density distribution. The coupled network formulation is based on a restricted resistive network formed by setting the core conductivity in the radial direction to zero. This restriction results in an induced loss calculation due only to the radial component of the core magnetic flux density. It is shown that the power loss due to radial flux is decoupled from that due to parallel running or main flux and therefore their theoretical evaluations can be performed separately. The axiperiodic model is also used to investigate the frequency dependence of the radial component of the magnetic flux density.

A closed form expression for the power loss due to radial flux is also derived. This expression can be used by axial flux machine designers to make a quick assessment of the requirement to consider power loss due to curvature related cross lamination flux.

Chapter 5 - Sub-domain Scaling for Finite Element Analysis of Electrical Machines, presents a sub-domain scaling technique for finite element analysis of axial flux machines with narrow air-gap regions. It is shown that this technique has the ability to both reduce the number of nodes required to mesh the domain as well as improving the mesh quality.

Whilst this technique does not directly contribute to the work presented in the previous chapters, it does provide a tool which could be used to extend the work beyond its current limitations.

Chapter 6 - Conclusion, reviews achievements of the research undertaken with respect to its aim and objectives. A section entitled “Further work” is also included which addresses some of the possible areas in which research could be performed to extend on the contributions made here. In this section it is argued that the scaling technique developed in Chapter 5 may prove very useful for further work in these areas.

Appendices:

Appendix A - Bessel Function Orthogonality, demonstrates the orthogonality property of Bessel functions with respect to a scaling coefficient over a fixed region when homogeneous derivative boundary conditions are imposed. This property is an integral part of the derivation of the analytical model presented in Chapter 2.

Appendix B - Air-Gap Flux Density Distribution, presents an analytical model of the air gap region of an axial flux machine. Using the derived model it is

shown that for narrow air-gaps the magnetic flux density becomes independent of radius.

Appendix C - Two-Dimensional Magnetostatic Analytical Model, derives a two-dimensional analytical model for the magnetic flux density distribution in the core of an axial flux machine. This model is compared with the three-dimensional model of Chapter 2, where it is shown that the two models agree in the limit of zero radial permeability.

The two-dimensional model is also used in Chapter 4 to provide an equation for the loss due to parallel running or main flux in axial flux machine cores.

1.6 Summary of Original Work

The original work presented in this dissertation focuses on the prediction of a radial component of the magnetic flux density in the back-iron of axial flux machine cores. The radial component investigated here is a direct consequence of the core curvature. It is shown that its magnitude is dependent on the core material properties and degree of core curvature. Analytical and numerical tools have been developed that allow the behaviour of the radial flux component to be investigated. These models also allow prediction of the induced losses caused by the tendency for flux to flow in the radial or cross laminate direction. A scaling technique has also been developed to assist in the finite element analysis of electrical machine with narrow air-gap regions. When used to analyse axial flux machines, this technique has the potential to reduce the computational resources required to perform finite element analysis.

It is concluded that in most practical axial flux machines the effects of curvature related radial flux on the iron loss and flux density distribution can be neglected. However, the effects of core curvature on the flux density distribution in the back-iron of these machines cannot be ignored. In this dissertation it is shown that core curvature results in a non-uniform flux density distribution with radius. Machine designers need to be aware of this distribution when sizing back-iron if excessive saturation is to be avoided.

Specifically the original contributions reported in this dissertation include:

- 1) Derivation of an analytical model of the magnetic flux density distribution in the core of axial flux machines. This model confirms the presence of a radial component in the flux density distribution. It also shows that the magnetic flux density is highest in the laminations near the outer radius of the core.
- 2) Development of an axiperiodic coupled network formulation for the prediction of induced losses caused by the tendency for flux to flow in the radial direction.
- 3) Derivation of a closed form expression for the power loss due to curvature related radial flux. This expression allows axial flux machine designers to make a quick assessment of the requirement to consider power loss due to curvature related cross lamination flux.
- 4) Development of a sub-domain scaling technique for finite element analysis of electrical machines with narrow air-gap regions. This technique has been developed as a general tool to assist in the finite element analysis (FEA) of axial flux machines. It has the potential to significantly reduce the computational resources required when performing FEA on these and other types of machines.

1.7 Publications

1.7.1 Publications:

- A. J. Hewitt, A. Ahfock and S. A. Suslov, “Magnetic flux density distribution in axial flux machine cores,” *IEE Proceedings - Electric Power Applications*, Vol. 152, No. 2, March 2005, pp 292-296.
- A. Hewitt and A. Ahfock, “Sub-domain scaling for finite element analysis of electrical machines,” *IEE Proceedings - Electric Power Applications*, Vol. 152, No. 2, March 2005, pp 149-156.
- A. Ahfock and A. Hewitt, “Curvature related eddy current losses in laminated axial flux machine cores,” *IEE Proceedings - Electric Power Applications*, Vol. 152, No. 5, September 2005, pp 1350-1358.

1.7.2 Acknowledgement of Contributions by Co-Authors

Firstly I wish to acknowledge the significant contributions made by my supervisor Dr Tony Ahfock in the preparation and production of this thesis. Not only was the topic of this project proposed by Dr Ahfock but throughout the course of the research he maintained a constant interest and provided invaluable assistance and guidance in the development of this work. Much of the work developed and presented herein was discussed with and reviewed by Dr Ahfock and for this support I will always be grateful.

I would also like to take this opportunity to acknowledge the contributions made by my co-authors in producing the aforementioned publications. More specifically;

- 1) for the publication entitled “Magnetic flux density distribution in axial flux machine cores” I would like to thank and acknowledge the guidance provided by Dr Sergey Suslov in developing the analytical solution. I would also like to thank and acknowledge Dr Ahfock’s assistance in developing the section on experimental

results.

- 2) for the publication entitled “Sub-domain scaling for finite element analysis of electrical machines” I would like to acknowledge the contributions made by Dr Tony Ahfock in proposing the idea and providing his guidance in the development of the section on material non-linearity.
- 3) for the publication entitled “Curvature related eddy current losses in laminated axial flux machine cores” I would like to acknowledge the contributions made by Dr Tony Ahfock in developing the sections on loss separation, closed form expression for power loss and laboratory tests.

Chapter 2

Curvature Related Radial Flux in Axial Flux Machine Cores

The two main physical reasons for the existence of a curvature related radial component of the magnetic flux density are longer flux path lengths at larger radii and the amount of flux being greater at larger radii. The tendency for magnetic flux to flow radially in the back-iron of AFMs does not seem to have been considered previously. A three-dimensional (3D) analytical model of the AFM back-iron is presented in this chapter. An important purpose of the model is to allow investigation of the radial component of the magnetic flux density.

Determining the magnitude of the radial component will allow us to predict the influence it has on the distribution of the axial and circumferential components of the flux density in the core. This will also answer the key question of whether or not the radial component can be ignored with respect to the flux density distribution. Determination of the flux density in AFM cores is greatly simplified if the radial component and its effects can be ignored.

2.1 Analytical Model

An analytical model is now derived for the core of an axial flux machine. This model provides some insight to the nature of the magnetic flux density distribution inside the core of these machines and identifies a previously unreported curvature related radial component of the flux density.

2.1.1 Single-Phase Excitation

For simplicity the following assumptions have been made:

- a) magnetic saturation, hysteresis and induced currents can be ignored;
- b) magnetic permeabilities in the radial, axial and circumferential directions may differ from each other, but are all constant;
- c) the core is uniform rather than laminated. However a significantly lower permeability is used in the radial direction to account for the effect of the low permeability electrical insulation separating the laminations (Reece & Preston, 2000);
- d) the regions outside the core (see Figure 2.1) have zero permeability;
- e) the core surface adjacent to the air-gap is smooth, that is the effects of teeth and slots are ignored;
- f) magnetic flux enters the core from the air-gap axially with flux density constant along the radial direction and varying sinusoidally in the circumferential direction.

Assumptions d) and f) imply that end-effects are ignored in the model. In practice end-effects will result in an increase in the magnetic flux density at the core edges (Bumby et al., 2004). Whilst it is acknowledged that end-effects need to be considered when investigating the magnetic flux distribution in the core back-iron, the focus of this research is on the effect of core curvature on the distribution.

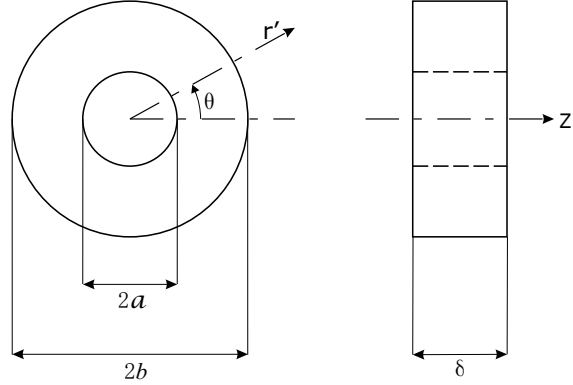


Figure 2.1: Stator core geometry and coordinate system.

The problem is formulated based on Maxwell's equations and the assumptions listed above. The assumption of no currents in the core allows the magnetic field intensity \vec{H}' to be defined in terms of a magnetic scalar potential ϕ' using

$$\vec{H}' = -\nabla\phi'. \quad (2.1)$$

The constitutive relationship between the magnetic flux density \vec{B}' and \vec{H}' can now be used to produce the defining model equation

$$\nabla \cdot (M'\nabla\phi') = 0, \quad (2.2)$$

where M' is the permeability tensor given by

$$M' = \begin{bmatrix} \mu_r & 0 & 0 \\ 0 & \mu_\theta & 0 \\ 0 & 0 & \mu_z \end{bmatrix}. \quad (2.3)$$

The boundary conditions are:

- 1) Magnetic insulation along the lower z' -plane boundary,

$$B'_z|_{z'=0} = 0 \quad (2.4)$$

- 2) The magnetic flux injection boundary,

$$B'_z|_{z'=\delta} = P \sin\left(\frac{p\theta}{2}\right) \quad (2.5)$$

3) Magnetic insulation at the inner and outer radial surfaces,

$$B'_r \Big|_{r'=a \text{ and } r'=b} = 0 \quad (2.6)$$

where B'_z and B'_r are the axial and radial magnetic flux densities respectively, P is the peak imposed flux density, a and b are the inner and outer core radii, respectively, δ is the core thickness, and $0 \leq \theta \leq 2\pi$ is the angular coordinate.

In coordinate form equation (2.2) becomes

$$\mu_r \frac{\partial^2 \phi'}{\partial r'^2} + \frac{\mu_r}{r'} \frac{\partial \phi'}{\partial r'} + \frac{\mu_\theta}{r'^2} \frac{\partial^2 \phi'}{\partial \theta^2} + \mu_z \frac{\partial^2 \phi'}{\partial z'^2} = 0. \quad (2.7)$$

The problem is non-dimensionalised as follows

$$\begin{aligned} r' &= r b \\ \phi' &= \phi \phi_0 \\ z' &= z \delta \end{aligned} \quad (2.8)$$

where b is the core outer radius δ the iron axial length and ϕ_0 , the characteristic value of the potential, is defined in equation (2.14). The permeability tensor (2.3) becomes

$$M = \begin{bmatrix} 1 & 0 & 0 \\ 0 & k_\theta & 0 \\ 0 & 0 & k_z \end{bmatrix} \quad (2.9)$$

where $k_\theta = \mu_\theta / \mu_r$, and $k_z = \mu_z / \mu_r$. The non-dimensional form of equation (2.7) is

$$\frac{\partial^2 \phi}{\partial r^2} + \frac{1}{r} \frac{\partial \phi}{\partial r} + \frac{k_\theta}{r^2} \frac{\partial^2 \phi}{\partial \theta^2} + \frac{b^2 k_z}{\delta^2} \frac{\partial^2 \phi}{\partial z^2} = 0 \quad (2.10)$$

and the non-dimensional boundary conditions are

$$\left. \frac{\partial \phi}{\partial z} \right|_{z=0} = 0, \quad (2.11)$$

$$\begin{aligned} k_z \mu_r \frac{\phi_0}{\delta} \left. \frac{\partial \phi}{\partial z} \right|_{z=1} &= P \sin \left(\frac{p\theta}{2} \right) \\ \Rightarrow \left. \frac{\partial \phi}{\partial z} \right|_{z=1} &= \sin \left(\frac{p\theta}{2} \right), \end{aligned} \quad (2.12)$$

and

$$\left. \frac{\partial \phi}{\partial r} \right|_{r=s \text{ and } r=1} = 0 \quad (2.13)$$

where $s = (a/b)$. Equations (2.11), (2.12) and (2.13) arise from the dimensional boundary conditions (2.4), (2.5) and (2.6), respectively, and we choose

$$\phi_0 = \frac{P\delta}{k_z \mu_r} = \frac{P\delta}{\mu_z} \quad (2.14)$$

to simplify the boundary condition (2.12).

We now use separation of variables to solve (2.10). Substituting

$$\phi = R(r) \cdot \varphi(\theta) \cdot Z(z)$$

in equation (2.10) gives

$$\frac{R''}{R} + \frac{1}{r} \frac{R'}{R} + \frac{k_\theta \varphi''}{r^2 \varphi} + \frac{k_z b^2 Z''}{\delta^2 Z} = 0 \quad (2.15)$$

where the primes denote the respective derivatives. Consistency within equation (2.15) requires that

$$\frac{Z''}{Z} = k_n^2 \frac{\delta^2}{b^2 k_z}, \quad n = 1, 2, 3, \dots \quad (2.16)$$

and

$$\frac{\varphi''}{\varphi} = -l^2 \quad (\text{to ensure angular periodicity}) \quad (2.17)$$

where k_n are real constants and $l = (p/2)$. Substituting (2.16) and (2.17) into (2.15) gives

$$r^2 R'' + rR' + (r^2 k_n^2 - k_\theta l^2)R = 0. \quad (2.18)$$

We now make the following simplifying substitution

$$m = l\sqrt{k_\theta} \quad (2.19)$$

which reduces (2.18) to

$$rR'' + rR' + (r^2 k_n^2 - m^2)R = 0. \quad (2.20)$$

Equation (2.20) is a Bessel Differential Equation (BDE), the solution of which is of the form $R_m(k_n r) = c_1 J_m(k_n r) + c_2 Y_m(k_n r)$ where J_m and Y_m are Bessel functions of the

first and second kind of order m , respectively. Enforcing the radial boundary condition (2.13) leads to the nonlinear eigenvalue problem for k_n

$$F_m(k_n) = J'_m(k_n s) Y'_m(k_n) - J'_m(k_n) Y'_m(k_n s) = 0, \quad (2.21)$$

the solutions of which are shown in Figure 2.2.

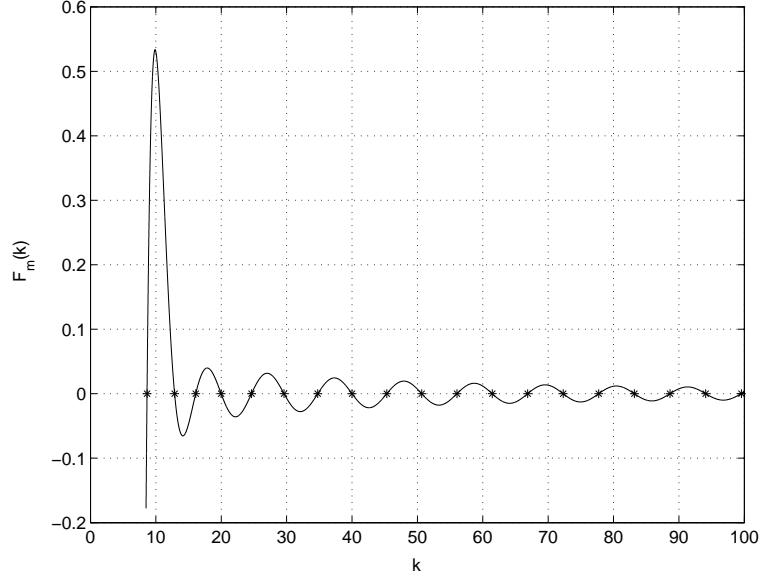


Figure 2.2: Solutions to the non-linear eigenvalue problem of equation (2.21) shown by * for $m = \sqrt{50}$ (i.e. $l = 1$, $\mu_\theta = 1000\mu_o$ and $\mu_r = 20\mu_o$) and $s = 75/175$.

Equation (2.16) is now solved using boundary condition (2.11) as follows:

$$\begin{aligned} \frac{Z''}{Z} &= k_n^2 \frac{\delta^2}{b^2 k_z} \equiv g_n^2 \\ \Rightarrow Z &= A \cosh(g_n z) + B \sinh(g_n z) \\ \Rightarrow Z' &= g_n A \sinh(g_n z) + g_n B \cosh(g_n z). \end{aligned} \quad (2.22)$$

where A is some constant and $g_n = \left[(k_n \delta) / (b \sqrt{k_z}) \right]$. Enforcing (2.11) reduces (2.22) to

$$Z = A \cosh(g_n z). \quad (2.23)$$

The solution for ϕ is now

$$\phi = \sum_{n=1}^{\infty} C_n \left[J_m(k_n r) - \frac{J'_m(k_n s)}{Y'_m(k_n s)} Y_m(k_n r) \right] \sin(l\theta) \cosh(g_n z). \quad (2.24)$$

In order to algebraically simplify the solution (2.24) we redefine the coefficient C_n so that

$$\begin{aligned}\phi &= \sum_{n=1}^{\infty} C_n \left[J_m(k_n r) - \frac{J'_m(k_n s)}{Y'_m(k_n s)} Y_m(k_n r) \right] \frac{\sin(l\theta) \cosh(g_n z)}{g_n \sinh(g_n)} \\ &= \sum_{n=1}^{\infty} C_n \left[J_m(k_n r) - \frac{J'_m(k_n s)}{Y'_m(k_n s)} Y_m(k_n r) \right] \frac{\sin(l\theta)}{g_n} \left[\frac{e^{g_n(z-1)} + e^{-g_n(z+1)}}{1 - e^{-2g_n}} \right] \quad (2.25)\end{aligned}$$

Applying boundary condition (2.12) to equation (2.25) results in the following infinite series

$$\sum_{n=1}^{\infty} C_n \left[J_m(k_n r) - \frac{J'_m(k_n s)}{Y'_m(k_n s)} Y_m(k_n r) \right] = 1. \quad (2.26)$$

The orthogonality properties

$$\int_s^1 r R_m^2 dr = \frac{1}{2k_n^2} [(m^2 - k_n^2 s^2) R_m^2(k_n s) - (m^2 - k_n^2) R_m^2(k_n)] \quad (2.27)$$

and

$$\int_s^1 r R_m(k_n r) R_m(k_e r) dr = 0, \quad n \neq e, \quad (2.28)$$

where

$$R_m(k_n r) = J_m(k_n r) - \frac{J'_m(k_n s)}{Y'_m(k_n s)} Y_m(k_n r)$$

and k_n and k_e satisfy the nonlinear eigenvalue problem (2.21) are shown in Appendix A. Using the orthogonality relationships (2.27) and (2.28) the unknown coefficients in (2.25) are found to be

$$C_n = \frac{2k_n^2 \int_s^1 r \left[J_m(k_n r) - \frac{J'_m(k_n s)}{Y'_m(k_n s)} Y_m(k_n r) \right] dr}{m^2 (R_m^2(k_n s) - R_m^2(k_n)) + k_n^2 (R_m^2(k_n) - s^2 R_m^2(k_n s))} \quad (2.29)$$

where:

$$R_m(k_n s) = J_m(k_n s) - \tilde{k} Y_m(k_n s).$$

In accordance with equations (2.1),(2.2), (2.3) and (2.8) the components of the dimensional magnetic flux density within the core are given by

$$B'_r = \frac{\mu_r P \delta}{\mu_z b} \frac{\partial \phi}{\partial r}, \quad (2.30)$$

$$B'_\theta = \frac{\mu_\theta P \delta}{\mu_z b r} \frac{\partial \phi}{\partial \theta}, \quad (2.31)$$

$$B'_z = P \frac{\partial \phi}{\partial z}. \quad (2.32)$$

2.1.2 Three-Phase Excitation (Rotating Fields)

The solution to a balanced three phase system is of the same form as that of the single phase system and can be found by modifying the injection boundary condition (2.5) to become

$$\begin{aligned} B'_z &= P \left[\sin(l\theta) \sin(\omega t) + \sin\left(l\theta + \frac{2\pi}{3}\right) \sin\left(\omega t - \frac{2\pi}{3}\right) \right. \\ &\quad \left. + \sin\left(l\theta - \frac{2\pi}{3}\right) \sin\left(\omega t + \frac{2\pi}{3}\right) \right] \\ &= \frac{3}{2} P \cos(\omega t + l\theta) \end{aligned} \quad (2.33)$$

where $\omega = 2\pi f$, f is the supply frequency and t represents time. The solution for ϕ is then

$$\phi = \frac{3}{2} \cos(\omega t + l\theta) \sum_{n=1}^{\infty} \frac{C_n}{g_n} \left[J_m(k_n r) - \frac{J'_m(k_n t)}{Y'_m(k_n t)} Y_m(k_n r) \right] \left[\frac{e^{g_n(z-1)} + e^{-g_n(z+1)}}{1 - e^{-2g_n}} \right] \quad (2.34)$$

Equations (2.30),(2.31) and (2.32) can then be used to predict the magnetic flux density distribution in the core.

Such a rotating field could be produced by either a static three-phase set of windings or by a set of rotating magnets.

2.1.3 Air-gap Flux Density Distribution

The analytical model developed in Section 2.1.1 is based on an assumption of magnetic flux entering the core from the air-gap axially with the flux density being constant in the radial direction and varying sinusoidally in the circumferential direction. Previous work performed by Chan & Leung (1980), Chan (1987) and Zhilichev (1998) show that this is a good approximation when end effects are neglected. Chan (1987) gives an expression for the air-gap flux density however the assumptions and boundary conditions used are not clear. A complete derivation of the air-gap flux density is presented in Appendix B. The prediction of constant axial magnetic flux density with radius is not surprising for narrow air gaps. This can be seen by applying Ampere's law for a contour defined over the angular displacement of one pole pitch as shown in Figure 2.3. For practical core permeabilities the magnetic field intensity H can be neglected inside the cores making the integral equal to $2H_z l_g$ where H_z is the axial component of field intensity in the air-gap and l_g the air-gap length. The current enclosed by any such constant radius contour will be constant and therefore H_z is also constant with radius. Thus the magnitude of the axial component of the magnetic flux density will be independent of radius.

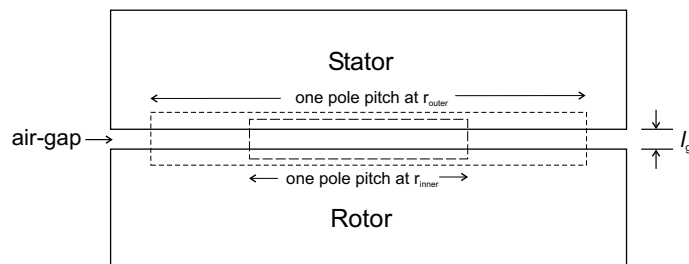


Figure 2.3: Integration contours for Amperes law.

2.1.4 The Effect of Curvature on the Radial Flux Density

The static three-dimensional solution of Section 2.1.1 predicts a radial component of the magnetic flux density B'_r in the core of axial flux machines. The magnitude of this component is given by equation (2.30) where ϕ is fully defined by equations (2.25) and (2.29). It is apparent from equations (2.30) and (2.25) that the magnitude of B'_r is influenced by the material permeabilities in the axial and radial directions, the core axial length, the imposed magnetic flux density and the core outer radius. The differential term in equation (2.30) seems to obscure the influence of the circumferential permeability and the curvature of the core. However, inspection of equation (2.19) reveals that the Bessel function order is determined by $k_\theta = \mu_\theta/\mu_r$ and $l = p/2$. There is also a measure of curvature present in the term $s = a/b$ in equation (2.29). Qualitatively we would expect the circumferential permeability to play an important role in determining B'_r as it is a significant component of the main flux path reluctance. As discussed earlier, the two main reasons for the existence of B'_r are the variations in the main flux path reluctance or length with radius and the greater amount of flux at larger radii. Both of these variations are influenced by the core curvature and thus it is worth investigating the effect of curvature on the peak magnitude of B'_r .

If the core curvature is defined as the inverse of the average core radius, then variations in the curvature are achieved by varying the values of a and b in the analytical solution of Section 2.1.1. Isolation of the curvature effect is achieved by maintaining a constant value for the imposed magnetic flux per pole pitch. The radial and axial lengths of the core as well as the pole pitch should also be kept constant. This can be achieved by considering a single pole pitch of a machine in which the number of poles is varied in order to keep these values constant. For a constant imposed flux per pole pitch

$$k = \int_a^b \int_0^{\frac{\pi}{p}} \cos\left(\frac{p\theta}{2}\right) r \partial\theta \partial r = \left(\frac{a+b}{p}\right) (b-a),$$

the average pole pitch $k_1 = \pi(a+b)/p$ and the core radial length $k_2 = (b-a)$ are kept constant. Varying core curvature in the model whilst keeping the desired variables

constant is achieved by first choosing practical values for k_1 and k_2 . These constants along with an arbitrary starting value for the number of poles are then used to determine the core inner and outer radii. The number of poles is varied to give modified values for the inner and outer radii which in turn change the core curvature. The influence of core curvature on the the peak radial flux density component is shown in Figure 2.4. The curves in Figure 2.4 also show the variation in the peak value of B'_r for differing circumferential permeabilities over a range of curvature values.

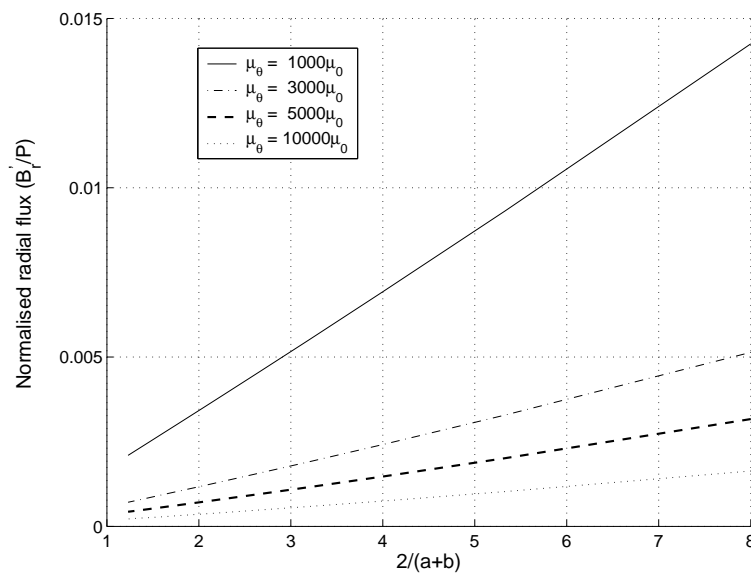


Figure 2.4: The effect of curvature on the peak radial flux density.

It can be seen from Figure 2.4 that the magnitude of the B'_r is small in comparison to the peak air-gap flux density. This is true even when a core exhibits a relatively large amount of curvature and low magnetic permeability; the potential for radial flux to flow increasing with curvature and lower permeabilities.

2.2 Predicted Core Magnetic Flux Density Distribution

The model proposed in Section 2.1.1 was evaluated for the following realistic physical parameters

$$\begin{aligned} a &= 0.075 \text{ m}, \\ b &= 0.175 \text{ m}, \\ \delta &= 0.1 \text{ m}, \\ p &= 2, \\ \mu_\theta &= \mu_z = 1000\mu_o, \end{aligned}$$

where μ_o is the permeability of free space. A laminate stacking factor $sf = 0.95$ is assumed resulting in an effective radial permeability (μ_r) (Reece & Preston, 2000) of

$$\mu_r = \frac{\mu_{air}}{(1 - sf)} = 20\mu_o. \quad (2.35)$$

The convergence results of the infinite series given in equation (2.26) at the magnetic flux injection boundary for a truncated number of terms is shown in Figure 2.5. All numerical results presented here are obtained using 60 terms in the series which guarantees errors of less than 10^{-5} .

The model predicts the existence of a radial component in the magnetic flux density with peak values along the pole-centre planes, shown in Figure 2.6. Finite element analysis using FEMLAB (COMSOL, 2004) makes practically the same prediction.

It can be seen from Figure 2.6 that the peak radial flux densities are small compared to the peak air-gap flux density P . The predicted radial flux component under the assumption of no induced currents should be regarded as an upper limit. In practice levels of radial flux will be smaller, possibly by as much as an order of magnitude, due to the shielding effect of the eddy currents induced as a result of the tendency for flux to flow radially.

Figure 2.7 shows theoretically predicted flux densities through planes half way between

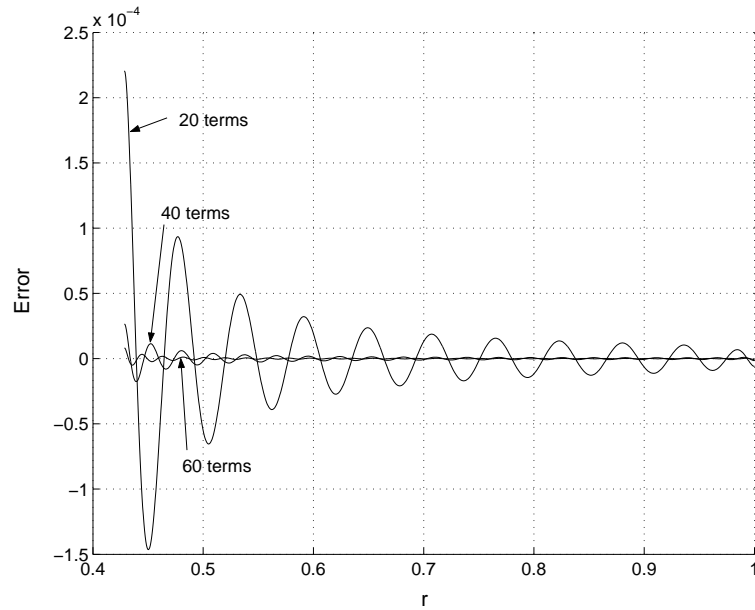


Figure 2.5: Error in the truncated infinite series of equation (2.26).

pole-centre planes. Only the circumferential flux density component is non-zero on these planes. An economically designed core will have an axial length such that the back-iron experiences its overall peak flux density on those planes. The top and bottom curves in Figure 2.7 show that there is a significant difference between peak flux densities experienced by laminations at different radii. The presence of a radial component in the flux density causes this difference to be reduced. This is to be expected as radial flux results in a redistribution of the flux. However, as pointed out previously, the magnitude of radial flux assumed in Figure 2.7 should be regarded as an upper limit since the shielding effect of induced eddy currents is likely to be significant. A safe approach when sizing the axial length of the core back-iron is to assume that the radial component of the flux density is equal to zero. Under this assumption, flux redistribution cannot occur and the lamination near the outer radius will experience the greatest overall circumferential flux density. Figure 2.7 also shows that the circumferential flux density near the outer radius is much higher than the average core back-iron circumferential flux density.

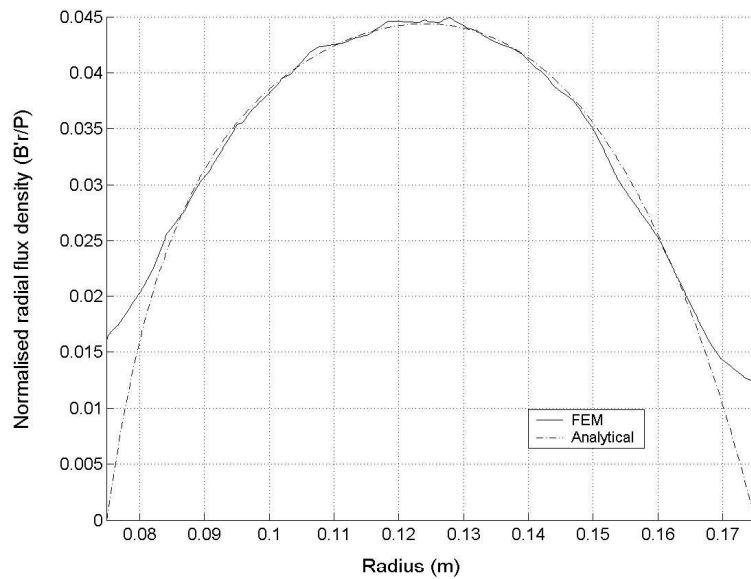


Figure 2.6: Radial component of flux density along the pole-centre plane using $n = 50$ modes for the analytical solution given in equation (2.25) .

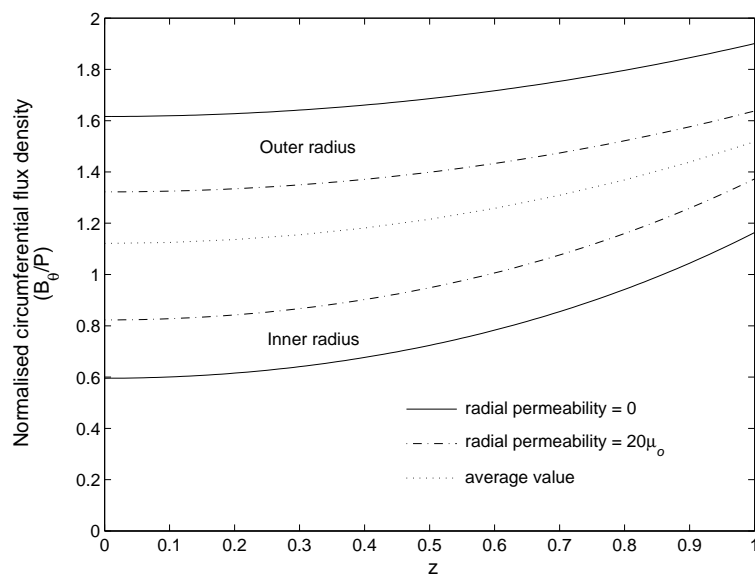


Figure 2.7: Normalised circumferential flux densities through planes half way between pole centre planes.

2.2.1 Experimental Results

Direct physical measurement of the flux density in the core of an electrical machine is impossible. Measurements of the amount of flux crossing areas in planes perpendicular to laminations (r - z planes) have been made. The experimental set-up used is shown in Figure 2.8. This set-up was constructed specifically for the purpose of investigating the flux distribution in the test core. The slotted bottom core was wound as a 2-pole single phase stator and was energized from a 50 Hz sinusoidal a.c. supply. There was a uniform air-gap of approximately 1 mm between the bottom core and the unslotted test-core. The test-core remained magnetically unsaturated during testing.

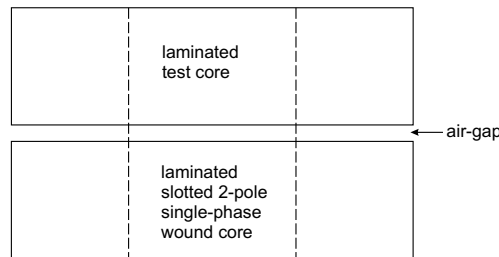


Figure 2.8: Experimental set-up.

Measurements were made using two probes P1 and P2, as shown in Figure 2.9. The measurement points Z1 and Z2 are at the same radial distance from the central axis. Point Z2 was located on the air-gap side of the test-core. Access to point Z2 was via one of the slots in the bottom core. All the slots were filled to about eighty percent making it possible to both insert a specially made probe in the selected slot and to make good electrical contact with the test-core at measurement point Z2. The selected slot was positioned so that Z1 and Z2 were located on the plane half way between pole centre planes. Careful removal of insulating material was necessary to ensure good electrical contact at Z1 and Z2.

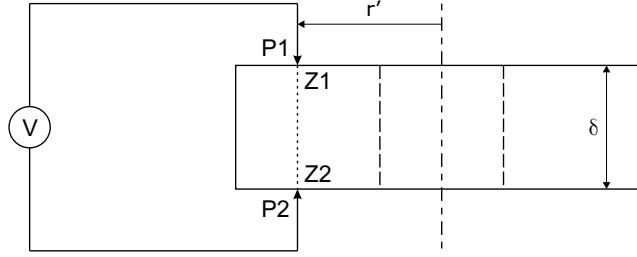


Figure 2.9: Test-core voltage measurement.

Measurements were made at ten different locations between $r' = a$ and $r' = b$. The normalized amount of flux at r' was calculated as the ratio

$$\frac{\text{net measured voltage } (r')}{\text{net measured voltage } (r' = a)}, \quad (2.36)$$

where the net measured voltage is the difference between the actual measured voltage and the measured voltage due to end flux per turn. Net measured voltage rather than actual voltage is used in equation (2.36) so that there is consistency with theoretical predictions which assume zero end flux. Voltage due to end flux was measured by means of a coil spanning one pole pitch of the test core and located so that it links all the end flux entering the core.

The normalised amounts of measured flux are shown in Figure 2.10. Equation (2.31) is used to compare theoretical predictions with measured values. The solid line in Figure 2.10 represents a two-dimensional analytical solution obtained in the limit $\mu_r \rightarrow 0$. The assumed value of P in equation (2.31) is such that the total circumferential flux through the plane half way between pole centre-planes was equal to the measured value.

If flux density was independent of radius, then the graph shown in Figure 2.10 would be a straight line passing through the origin. However, it is clear that both the theoretical curves and the measured data suggest greater flux densities at larger radii. Since flux density is proportional to the gradient of the curves, the experimental results can be used to obtain an estimate of the ratio of the flux density near the outer radius to the average flux density. This is found to be approximately 1.37 for the considered geometry and is in good agreement with the theoretical prediction if the radial component of

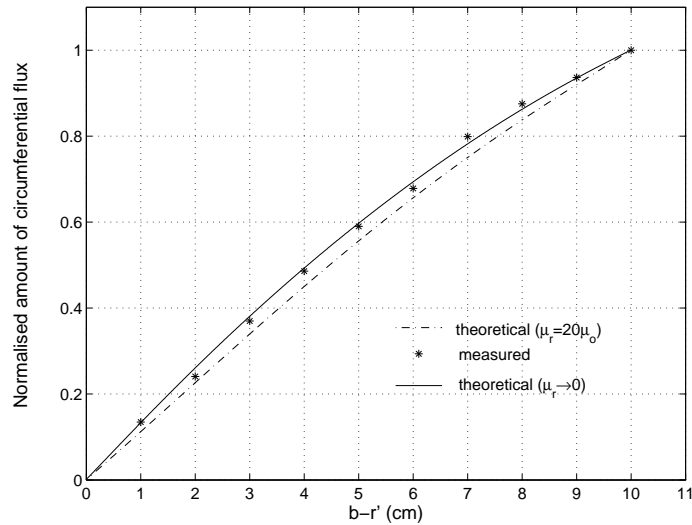


Figure 2.10: Measured and predicted circumferential flux.

the flux density is assumed to be zero (which would be the case if there was ‘perfect shielding’ due to induced eddy currents). If there were no shielding effect, in theory B_r would assume the levels shown in Figure 2.6. Figure 2.10 gives theoretical curves corresponding to both the ‘perfect shielding’ ($\mu_r \rightarrow 0$) and ‘no shielding’ ($\mu_r = 20\mu_0$) situations. These curves are relatively close to each other and therefore, while the experimental results provide convincing evidence that the flux density is significantly greater at larger radii, they cannot be used to confirm that shielding due to eddy currents has a dramatic effect on the amount of the radial flux component.

2.2.2 Practical Implications

Both theoretical and experimental results show that the magnetic flux density in the circumferential direction is highest in the laminations near the outer radius of the core of AFMs. This should be taken into consideration if excessive saturation in this region of the core back-iron is to be avoided (Hewitt et al., 2005).

In RFM cores, if end effects are neglected, the use of 2D models for purposes such as prediction of tooth saturation level and electromagnetic torque is justified because

of the absence of axial flux. On the condition that the radial component of the flux density B'_r can be ignored, 2D modeling is also justified for AFMs. However for a given AFM, several 2D models would be required. Assuming slot-width does not vary with radius, laminations closer to the inner radius would be modeled with relatively smaller slot-pitch and tooth-width compared to laminations closer to the outer radius.

The magnitudes of B'_r shown in Figure 2.4 suggest that in practice the radial component of the magnetic flux density can be ignored with respect to its influence on the distribution of the circumferential and axial components of the flux density in the core. This offers the significant advantage of being able to use 2D models as suggested above. The removal of the radial flux density component also significantly simplifies the analytical solution for the flux density distribution in the core. A 2D analytical solution is presented in Appendix C. Comparing the 3D and 2D solutions for the non-dimensional magnetic scalar potential ϕ given by equations (2.25) and (C.19), respectively, it can be seen that the 2D solution is of a much simpler form and is thus easier to evaluate. A comparison of the normalised circumferential flux density component through planes half way between the pole centre planes found using the 2D and 3D solutions are shown in Figure 2.11.

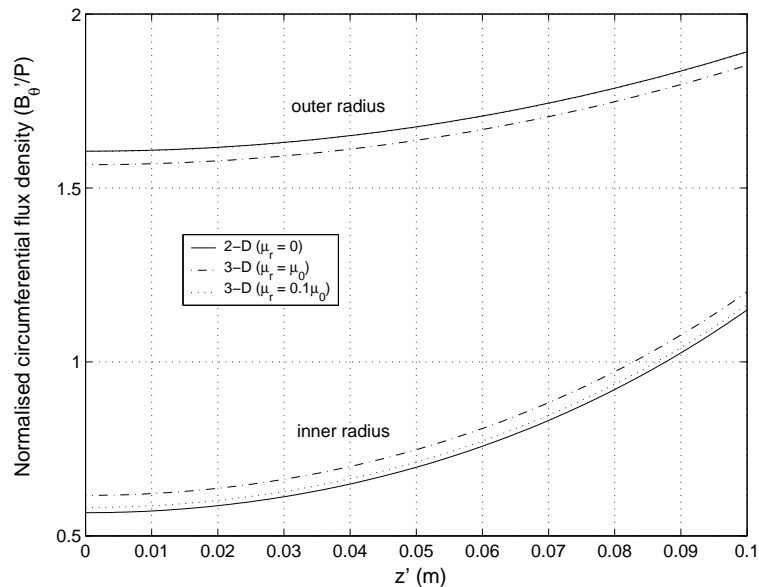


Figure 2.11: Normalised circumferential flux density found using the 2D and 3D models.

These curves show that in the limit $\mu_r \rightarrow 0$ the 3D model will produce the same results as that of the 2D model.

While the magnitude of B'_r is significantly less than that of the main flux components the question of induced losses caused by this component still needs to be addressed. It has long been standard engineering practice to use laminated cores to reduce eddy current losses. Unfortunately the radial component of the flux density flows in a cross laminate direction and thus induced losses may be significant, even for relatively low values of B'_r . In Chapters 3 and 4 numerical techniques are developed and the losses caused by the tendency for radial flux to flow are investigated.

Chapter 3

The Coupled Network Method

Predicting losses due to the radial component of the magnetic flux density in the stator back-iron requires numerical quasi-static analysis of the core. There exists a number of techniques to perform such an analysis including the Finite Element Method (FEM), Integral equation methods and Finite difference methods (Chari & Salon, 2000).

The finite element method has gained significant popularity over recent years and is possibly the most commonly used technique for electromagnetic analysis of electrical machines. There has also been a number of different formulations developed based on the finite element technique (Ratnajeevan & Hoole, 1995). Finite element formulations have been extensively implemented in a number of commercially available software packages.

A less common technique for electromagnetic analysis is the coupled network method. This method uses a coupled magnetic and electric circuit representation of the domain. The magnetic or reluctance network has been comprehensively reported on by a number of authors and has been compared with the finite difference and finite element methods (Balchin & Davidson, 1980; Carpenter, 1975*c*; Chari & Salon, 2000; Demenko et al., 1998; Sykulski, 1995; King, 1966*a*; King, 1966*b*). The coupled network formulation is based on two physically separate but electromagnetically coupled networks.

The magnetic and electric networks are commonly referred to as the reluctance and resistance networks respectively. The use of coupled networks for electromagnetic analysis has also been widely reported on in published papers such as Demenko (2000), Balchin & Davidson (1983), Davidson & Balchin (1983), Davidson & Balchin (1981), Balchin & Davidson (1980), Carpenter (1977), Carpenter (1975*a*), Carpenter (1975*b*), Carpenter (1975*c*), King (1966*a*) and King (1966*b*). Roisse et al. (1998) and King (1966*b*) used coupled networks to analyse synchronous and induction machines respectively, including the effects of saturation and motion. One important advantage of the coupled network approach is the physical interpretation which the network formulation provides (Carpenter, 1975*c*; Guo & Zhu, 2002; King, 1966*a*).

In general, three dimensional numerical quasi-static electromagnetic analysis of regions involving currents requires the solution to be formulated in terms of a scalar and vector potential. These formulations require the solution of four unknowns per node in a discretised system. In order to reduce computation times and resources, techniques and formulations have been developed to reduce the number of degrees of freedom for some problems. In some instances it is possible and practical to model a three dimensional domain as a two dimensional problem with appropriate boundary conditions. The axisymmetric and axiperiodic formulations are examples of these. Where commercially available software does not include these formulations the user is required to either modify existing code or to generate in-house code to solve their particular problem.

The analytical model presented in Chapter 2 showed that the core magnetic flux density varies sinusoidally in the circumferential direction. This is a direct consequence of the angular periodicity in the imposed magnetic flux density at the core-air gap boundary. The periodicity in the circumferential direction allows a slotless axial flux machine core to be modeled using the axiperiodic formulation. This formulation is not widely available in commercial finite element software packages. For this reason and because of the simple geometry of the core as well as the physical interpretation offered, the coupled network method has been chosen to provide quasi-static analysis of an AFM core.

In the following sections a coupled resistance-reluctance network formulation will be presented. We begin with a generic three dimensional coupled network formulation. The resistive network is then restricted to a series of planar networks, the purpose of which is to determine the losses due to and frequency dependence of the radial component of the core magnetic flux density. It is also show in Section 3.3 that the coupled network formulation derived here is in fact just an application of the finite difference method.

An axiperiodic coupled network formulation is presented in Section 3.4. This formulation is used in Chapter 4 to predict the induced losses in axial flux machine cores caused by the tendency for flux to flow radially.

3.1 Magnetostatic Analysis without Currents

In magnetostatic analysis where no electric currents are present the magnetic field intensity \vec{H} can be defined in terms of a magnetic scalar potential Ω . In a current free region

$$\nabla \times \vec{H} = 0,$$

and thus the magnetic scalar potential Ω can be introduced through

$$\vec{H} = -\nabla\Omega. \quad (3.1)$$

The magnetic flux density \vec{B} is related to the magnetic field intensity through the constitutive relation

$$\vec{B} = \mu\vec{H}$$

where μ is the material permeability. Consequently \vec{B} can be expressed as

$$\vec{B} = -\mu\nabla\Omega. \quad (3.2)$$

The magnetic flux density distribution in the core of an axial flux machine can be determined by solving equation (3.1) and imposing appropriate boundary conditions. The

reluctance network formulation presented here numerically solves for Ω by discretising the core using regular elements. Magnetic nodes are assumed at the element centroid as shown in Figures 3.1 and 3.2.

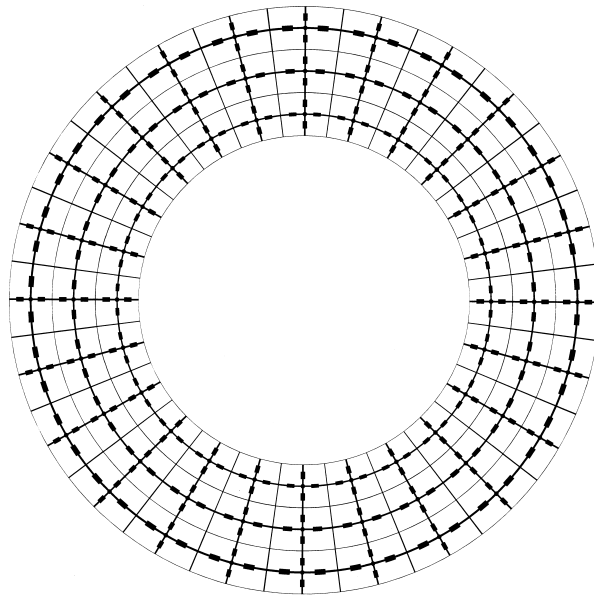


Figure 3.1: Core discretization.

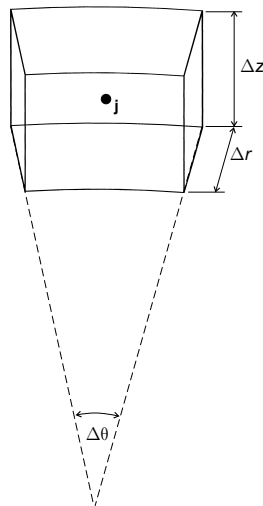


Figure 3.2: Element shape and node position.

The formulation is based on the equation

$$\mathbf{P}\boldsymbol{\Omega} = \boldsymbol{\phi}_{imp} \quad (3.3)$$

where \mathbf{P} is the permeance matrix, $\boldsymbol{\Omega}$ is a vector of magnetic scalar potentials at the nodes and $\boldsymbol{\phi}_{imp}$ is a vector of the imposed magnetic flux at the nodes. The resulting system of equations is solved to determine $\boldsymbol{\Omega}$. The derivation of the permeance matrix \mathbf{P} and the imposed magnetic flux vector $\boldsymbol{\phi}_{imp}$ will now be shown.

3.1.1 The Permeance Matrix

The system of equations is derived by considering magnetic Ohms law and the solenoidal condition of the magnetic flux density $\nabla \cdot \vec{B} = 0$ at each node in the discretized space. The resulting system of equations are the same as those used in electric circuit node analysis where electrical admittances are replaced by magnetic permeances. Magnetic branch permeances are calculated on an element by element basis using element lengths, areas and material permeabilities. Figure 3.3 shows a typical element structure with its associated node and permeance branches.

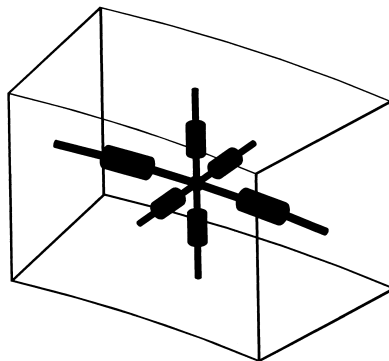


Figure 3.3: Element structure and associate permeance branches.

The magnetic scalar potential Ω is calculated at the nodes. Each node is connected to its six surrounding neighbors by permeance branches. The branch permeances ρ are

defined by

$$\rho = \frac{\mu A}{l} \quad (3.4)$$

where l is the path length, μ the material permeability and A the cross sectional area of the flux path. In order to simplify permeance calculations elements have been chosen such that material boundaries lie either at nodes or coincide with element boundaries. The resulting permeance matrix \mathbf{P} is sparse with the diagonal entries equal to the sum of all permeances connected to a node and the off-diagonal entries the negative of the permeances connecting the nodes.

3.1.2 Imposed Magnetic Flux

Based on the assumption of the magnetic flux entering the core from the air-gap axially with the flux density being constant in the radial direction and varying sinusoidally in the circumferential direction, the magnetic flux injection vector ϕ_{imp} can be found. The imposed magnetic flux for nodes located at the injection boundary of the core are found using the element axial areas (see Figure 3.1).

At an average element radius of

$$\tilde{r} = \frac{r_i + r_o}{2} \quad (3.5)$$

where r_i and r_o are the element inner and outer radii, respectively, the element axial injection area is given by

$$\begin{aligned} A &= \Delta\theta \tilde{r} (r_o - r_i) \\ &= \Delta\theta \left(\frac{r_o^2 - r_i^2}{2} \right). \end{aligned} \quad (3.6)$$

Here $\Delta\theta$, shown in Figure 3.2, is given by $\Delta\theta = 2\pi/n_\theta$, where n_θ is the number of divisions used to discretise the core in the circumferential direction. The imposed

magnetic flux over an arbitrary element j is given by

$$\begin{aligned}
\phi_{imp_j} &= \int_{r_{1j}}^{r_{2j}} \int_{\theta_{1j}}^{\theta_{2j}} \hat{B}_z \cos\left(\frac{p\theta}{2}\right) r \partial\theta \partial r \\
&= \frac{\hat{B}_z}{p} (r_{2j}^2 - r_{1j}^2) \left[\sin\left(\frac{p\theta_{2j}}{2}\right) - \sin\left(\frac{p\theta_{1j}}{2}\right) \right] \\
&= \frac{2\hat{B}_z}{p} \frac{A}{\Delta\theta} \left[\sin\left(\frac{p\theta_{2j}}{2}\right) - \sin\left(\frac{p\theta_{1j}}{2}\right) \right]
\end{aligned} \tag{3.7}$$

where r_{1j} and r_{2j} are the inner and outer radii of the j th element, θ_{1j} and θ_{2j} are the angular limits of the element, \hat{B}_z is the peak axial magnetic flux injection at the core surface and p the number of machine poles. The element angular limits θ_{1j} and θ_{2j} can be replaced by the constant $\Delta\theta = (\theta_{2j} - \theta_{1j})$ and the node angular position θ_j by rewriting the trigonometric difference in equation (3.7) as

$$\begin{aligned}
\sin\left(\frac{p\theta_{2j}}{2}\right) - \sin\left(\frac{p\theta_{1j}}{2}\right) &= \sin\left(\frac{p\theta_j}{2} + \frac{p\Delta\theta}{4}\right) - \sin\left(\frac{p\theta_j}{2} - \frac{p\Delta\theta}{4}\right) \\
&= 2 \sin\left(\frac{p\Delta\theta}{4}\right) \cos\left(\frac{p\theta_j}{2}\right).
\end{aligned} \tag{3.8}$$

Substituting equation (3.8) into (3.7) results in

$$\phi_{imp_j} = \frac{4\hat{B}_z}{p} \frac{A}{\Delta\theta} \sin\left(\frac{p\Delta\theta}{4}\right) \cos\left(\frac{p\theta_j}{2}\right). \tag{3.9}$$

For small angular discretization $\Delta\theta \rightarrow 0$ the approximation

$$\sin\left(\frac{p\Delta\theta}{4}\right) \approx \frac{p\Delta\theta}{4}$$

can be used to reduce equation (3.9) to

$$\phi_{imp_j} = \hat{B}_z A \cos\left(\frac{p\theta_j}{2}\right). \tag{3.10}$$

3.1.3 Solving the System of Equations

Having constructed the permeance matrix \mathbf{P} and the vector of imposed magnetic flux ϕ_{imp} equation (3.3) can be solved to determine the values of the scalar potential $\mathbf{\Omega}$ at the nodes. Solving this matrix equation requires the permeance matrix to be inverted

which may cause difficulties if the matrix is very large. The size of \mathbf{P} will depend on the number of elements (or nodes) used in the core discretization. Discretization needs to be sufficiently fine to describe variations in the magnetic field. Sparse matrices and numerical inversion techniques can be used where required.

3.2 Eddy Current Analysis using the Coupled Network Method

The system of equations for a coupled magnetic and electric networks is now derived. These equations are derived based on the interaction between the two networks as described by Faraday's and Ampere's laws. The formulation derived here is restricted to that required to predict curvature related power loss in laminated axial flux machine cores. This is achieved by setting the conductivity in the radial direction σ_r to zero. Imposing this restriction results in only axial and circumferential components in the current density and only the coupling between induced currents and radial permeance branches need be considered.

Consider the modified magnetic or reluctance network described by

$$P\Omega = \phi_{imposed} + \phi_{induced} \quad (3.11)$$

where $\phi_{imposed}$ is a vector applied or imposed magnetic flux at the nodes and $\phi_{induced}$ a vector of induced magnetic flux at the nodes due to induced currents. Let $\phi_{induced}$ be represented by a vector of loop currents \mathbf{I} and a connectivity matrix \mathbf{Q} which links the loop currents to node flux injections to give

$$P\Omega = \phi_{imposed} - Q\mathbf{I} \quad (3.12)$$

or equivalently

$$P\Omega + Q\mathbf{I} = \phi_{imposed}. \quad (3.13)$$

The connectivity matrix \mathbf{Q} can be derived by considering two magnetic branches connected to a common node j as shown in Figure 3.4. Let each magnetic permeance

branch be enclosed by an associated current loop, also shown in Figure 3.4. The source of this current being the emf induced by a time varying magnetic flux in the permeance branch. This will be discussed further in the following sections.

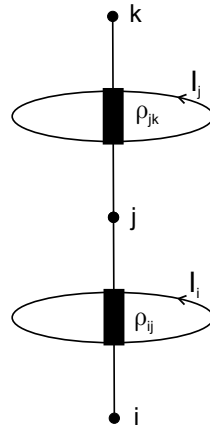


Figure 3.4: Radial permeance branches with their associated loop currents.

The loop currents of each of the magnetic branches can be replaced by Norton equivalent circuits as shown in Figure 3.5.

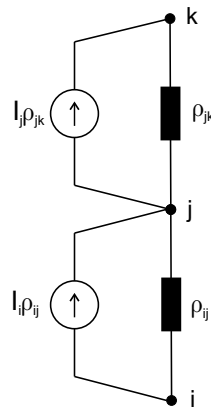


Figure 3.5: Norton equivalent circuit .

The Norton equivalent circuit of Figure 3.5 shows how the magnetic branch loop current modifies the magnetic flux entering node j , which is the basis for the derivation of the

\mathbf{Q} matrix. For any arbitrary node j the \mathbf{Q} matrix will have two entries

$$\mathbf{Q}(j, j) = \rho_{jk} \quad (3.14)$$

$$\mathbf{Q}(j, i) = -\rho_{ij}. \quad (3.15)$$

The permeance matrix \mathbf{P} and the vector of imposed magnetic flux ϕ_{imp} of equation (3.13) is found in the same way as described in Sections 3.1.1 and 3.1.2.

We now derive a system of equations for the unknown loop currents. As stated earlier these loop currents are the result of the induced emf given by Faraday's law

$$\oint \vec{E} \cdot d\vec{l} = - \iint \frac{\partial \vec{B}}{\partial t} \cdot d\vec{s}.$$

The element structure which includes both magnetic permeance branches and electric loop resistances is shown in Figure 3.6. The electric network is formed by a system of resistive loops surrounding the magnetic branches. Resistance values are found using element lengths, areas and material conductivity σ in a similar way to that used to calculate the magnetic permeances. The branch resistances being defined by

$$R = \frac{l}{\sigma A},$$

where l is the path length and A the path cross sectional area.

The resistance values are not calculated using the same element dimensions as those used for the permeances. This is because the elements which define the electric network effectively lie between the elements of the magnetic network. The elements in both instances have the same shape and share common axial and radial lengths. Only the element average radii differ. If the magnetic elements have average radii denoted by r_j for $j = 1, 2, 3, \dots$ and the element radial length is Δr then the electric elements have average radii given by $(r_j + \Delta r/2)$. In the magnetic network the nodes lie at the element average radii in the radial direction, and similarly this can be considered the case for the electric network. The resulting discretization can then be considered as a radially staggered mesh between the magnetic and electric networks.

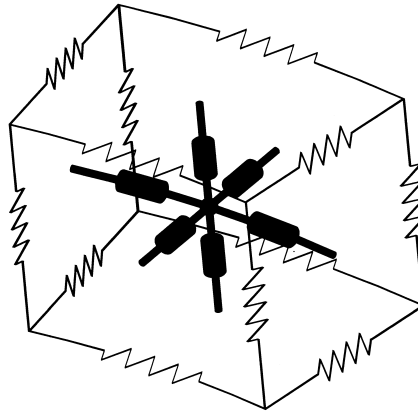


Figure 3.6: Element structure including both the magnetic and electric networks.

The loop current equations are derived by expressing the magnetic flux in a permeance branch in terms of the magnetic scalar potential at the branch nodes and the branch loop current. For the general branch shown in Figure 3.7 the loop current can be represented as a branch $mmf = I_j$ as shown in Figure 3.8.

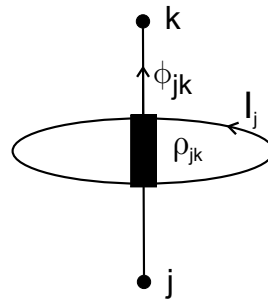


Figure 3.7: Permeance branch and its associated loop current.

It should be noted that in order to satisfy Ampere's law for all contours the loop current must be associated with the magnetic branch flux to which the loop current is linked. This requirement is further discussed in Section 3.3.3.

The branch magnetic flux ϕ_{jk} is now expressed in terms of the branch loop current I_j and the node scalar potentials Ω_j and Ω_k . From equation (3.2) the branch flux can be

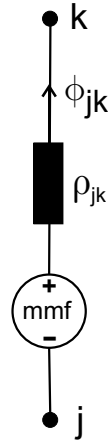


Figure 3.8: Permeance branch with its loop current replaced by an equivalent branch mmf.

written as

$$\begin{aligned}\phi_{jk} &= BA = -A\mu\nabla\Omega \\ &= \frac{\mu A}{l} (\Omega_j - \Omega_k)\end{aligned}\quad (3.16)$$

where B is the branch magnetic flux density, A is the element cross sectional area and l the branch length. Comparing equation (3.16) with equation (3.4) it is seen that (3.16) can be rewritten as

$$\phi_{jk} = \rho_{jk} (\Omega_j - \Omega_k). \quad (3.17)$$

Figure 3.8 shows that the branch loop current modifies the node magnetic potentials. The modified node potential are shown in Figure 3.9.

Adding the loop current term given in equation (3.17) results in

$$\begin{aligned}\phi_{jk} &= \rho_{jk} [(\Omega_j + I_j) - \Omega_k] \\ &= \rho_{jk} (\Omega_j - \Omega_k) + \rho_{jk} I_j.\end{aligned}\quad (3.18)$$

In matrix form this system of equations is written as

$$\phi = \mathbf{W}\Omega + \mathbf{S}\mathbf{I}, \quad (3.19)$$

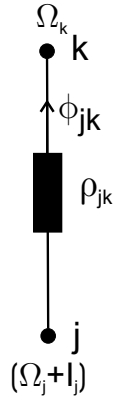


Figure 3.9: Permeance branch and its modified node scalar potentials.

where ϕ is a vector of branch flux, Ω a vector of magnetic scalar potentials, \mathbf{I} a vector of loop currents and \mathbf{W} and \mathbf{S} are matrices of permeance values given by

$$\mathbf{W}(j, j) = \rho_{jk} \quad (3.20)$$

$$\mathbf{W}(j, k) = -\rho_{jk} \quad (3.21)$$

and

$$\mathbf{S}(j, j) = \rho_{jk}, \quad (3.22)$$

respectively. The loop voltages V_j can be found using Faraday's law. For fields varying harmonically in time the loop voltages are defined by

$$V_j = -\frac{\partial \phi_{jk}}{\partial t} = -j\omega \phi_{jk}, \quad (3.23)$$

where $\omega = 2\pi f$ and f is the frequency of the harmonic time variation. Substituting equation (3.18) into (3.23) in matrix form gives

$$\mathbf{V} = -j\omega \phi = -j\omega \mathbf{W} \Omega - j\omega \mathbf{S} \mathbf{I} \quad (3.24)$$

where \mathbf{V} is a vector of induced loop voltages. The loop currents can be determined by using loop analysis theory. Loop analysis produces the system of equations

$$\mathbf{V} = \mathbf{R} \mathbf{I} \quad (3.25)$$

where \mathbf{R} is a matrix of loop resistances.

The resistance matrix \mathbf{R} is found by applying Kirchhoff's voltage law around each loop (i.e. loop analysis). For the arbitrary loop i, j, k , shown in Figure 3.10, the loop equation is given by

$$R_\theta (I_{i,j,k} - I_{i,j,k+1}) + R_z (I_{i,j,k} - I_{i,j+1,k}) + R_\theta (I_{i,j,k} - I_{i,j,k-1}) + R_z (I_{i,j,k} - I_{i,j-1,k}) = V \quad (3.26)$$

where V is the distributed loop emf and the loop branch resistances are defined by

$$R_\theta = \frac{r\Delta\theta}{\sigma_\theta\Delta r\Delta z}, \quad (3.27)$$

$$R_z = \frac{\Delta z}{\sigma_z r\Delta\theta\Delta r}. \quad (3.28)$$

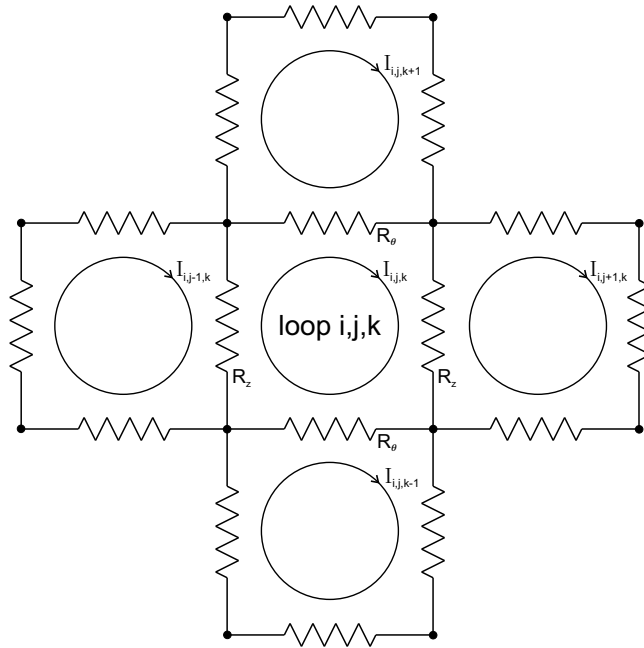


Figure 3.10: A general electric loop structure.

The resulting \mathbf{R} matrix will be a sparse matrix with diagonal entries equal to the sum of the branch resistances forming the individual loops, and off-diagonal entries equal to the negative of the resistance of the common branch.

Substituting equation (3.25) into equation (3.24) results in

$$\begin{aligned} \mathbf{R}\mathbf{I} &= -j\omega(\mathbf{W}\boldsymbol{\Omega} + \mathbf{S}\mathbf{I}) \\ \Rightarrow \tilde{\mathbf{W}}\boldsymbol{\Omega} + (\mathbf{R} + \tilde{\mathbf{S}})\mathbf{I} &= 0 \end{aligned} \quad (3.29)$$

where $\tilde{\mathbf{W}} = j\omega\mathbf{W}$ and $\tilde{\mathbf{S}} = j\omega\mathbf{S}$. Quasi-static analysis requires the system of equations defined by equations (3.13) and (3.29) to be solved simultaneously. The resulting system of equations is then

$$\left[\begin{array}{c|c} \mathbf{P} & \mathbf{Q} \\ \hline \tilde{\mathbf{W}} & (\mathbf{R} + \tilde{\mathbf{S}}) \end{array} \right] \left[\begin{array}{c} \boldsymbol{\Omega} \\ \mathbf{I} \end{array} \right] = \left[\begin{array}{c} \boldsymbol{\phi} \\ \mathbf{0} \end{array} \right]. \quad (3.30)$$

3.2.1 Alternate Formulation

The quasi-static formulation given in equation (3.30) solves for both the vector of magnetic scalar potentials $\boldsymbol{\Omega}$ and the vector of loop currents \mathbf{I} simultaneously. The system of equations can be rewritten such that only the magnetic scalar potentials are solved for. The derivation is the same as that presented previously up to equation (3.24). Using equation (3.25), equation (3.24) can be rewritten as

$$\begin{aligned} \mathbf{R}\mathbf{I} &= -j\omega\mathbf{W}\boldsymbol{\Omega} - j\omega\mathbf{S}\mathbf{I} \\ &= -\tilde{\mathbf{W}}\boldsymbol{\Omega} - \tilde{\mathbf{S}}\mathbf{I} \\ \Rightarrow \mathbf{I} &= -[\mathbf{R} + \tilde{\mathbf{S}}]^{-1} \tilde{\mathbf{W}}\boldsymbol{\Omega}. \end{aligned} \quad (3.31)$$

Substituting (3.31) into equation (3.13) results in

$$\begin{aligned} \phi_{imp} &= \mathbf{P}\boldsymbol{\Omega} - \mathbf{Q}[\mathbf{R} + \tilde{\mathbf{S}}]^{-1} \tilde{\mathbf{W}}\boldsymbol{\Omega} \\ \Rightarrow \boldsymbol{\Omega} &= \left[\mathbf{P} - \mathbf{Q}[\mathbf{R} + \tilde{\mathbf{S}}]^{-1} \tilde{\mathbf{W}} \right]^{-1} \phi_{imp} \end{aligned} \quad (3.32)$$

which permits $\boldsymbol{\Omega}$ to be solved for without solving for \mathbf{I} . Having solved for $\boldsymbol{\Omega}$ the loop currents can subsequently be calculated using equation (3.31).

The choice of formulation will depend on the type of matrix solver used. The augmented matrix system given by equation (3.30) is constructed from sparse and diagonal matrices. For models requiring very fine discretization the number of node can be quite

large and, unless sparse techniques are used, computing memory requirements will be large. Matrix inversion is also required which may cause matrices to become full. The formulation given in equation (3.32) does not require the augmented matrix of equation (3.30) however it does require multiple matrix inversions and more computational steps. The choice of formulation should be based on the model size (number of nodes) and the type of solution technique chosen.

3.2.2 Postprocessing

Having solved for $\mathbf{\Omega}$ and \mathbf{I} the magnetic flux density distribution and induced core losses can be found. The magnetic flux density in any magnetic branch can be calculated using equations (3.16) and (3.18). If desired, the magnetic flux density at the nodes can be found by taking the average of the branch magnetic flux densities connected to that node. For example, the radial component of the magnetic flux density at node j can be found using

$$B_{r_j} = \frac{\phi_{ij} + \phi_{jk}}{2A},$$

where the magnetic branch flux are as shown in figure 3.11 and A is the element cross-sectional area in the radial direction. As magnetic flux density is a vector quantity averaging must be performed over magnetic branches in the coordinate directions.

The induced losses in the core are calculated using loop current differences. The loop current difference or electric branch current (i.e. the current in the common branch resistance between adjacent loops) can then be used in an $I_j^2 R_j$ calculation over the domain. The summation of all these losses giving the total induced core losses. Current density distribution can also be calculated using the branch currents.



Figure 3.11: Radial connected permeance branches and their branch magnetic flux.

3.3 Coupled Networks and the Finite Difference Method

The finite difference method replaces the describing electromagnetic partial differential equations by difference equations. The domain is divided into cells (of finite area or volume) by a grid and the equations are written for the unknowns at the nodes. This process replaces the original partial differential equations with a set of simultaneous equations which are solved to give the unknown variables at the nodes. The finite difference method was one of the first numerical methods developed and is a well known and accepted technique for solving differential equations (Chari & Salon, 2000).

It will now be shown that the coupled network formulation of Section 3.2 is in fact just a finite difference formulation to the quasi-static problem. This is demonstrated for the restricted coupled network used to predict induced losses due to the radial component of the magnetic flux density. Justification for isolating this component of the losses is discussed in Chapter 4.

3.3.1 Node Equations

Most electromagnetic analysis is based on solving the differential form of Maxwell's equations on a domain with specified boundary conditions. There are a number of different formulations which permit these equations to be solved whilst offering a reduced number of unknowns. One way of achieving this is to express the system of differential equations in terms of scalar and vector potentials. Here we choose to rewrite Maxwell's equations in terms of an electric vector potential \vec{T} and a magnetic scalar potential Ω . The $(T - \Omega)$ formulation is derived from the quasi-static approximations to Maxwell's equations

$$\nabla \times \vec{H} = \vec{J}, \quad (3.33)$$

$$\nabla \cdot \vec{B} = 0, \quad (3.34)$$

$$\nabla \times \vec{E} = -\frac{\partial \vec{B}}{\partial t}, \quad (3.35)$$

$$\nabla \cdot \vec{J} = 0, \quad (3.36)$$

and the constitutive relations

$$\vec{B} = \mu \vec{H} \quad (3.37)$$

$$\vec{J} = \sigma \vec{E}. \quad (3.38)$$

The solenoidal condition of equation (3.36) allows \vec{J} to be defined in terms of an electric vector potential \vec{T} by

$$\vec{J} = \nabla \times \vec{T}. \quad (3.39)$$

Substituting (3.39) into equation (3.33) allows us to express \vec{H} in terms of \vec{T} and a magnetic scalar potential Ω by

$$\vec{H} = \vec{T} - \nabla \Omega. \quad (3.40)$$

Using the constitutive relation given in equation (3.37), equation (3.34) can be written in terms of \vec{T} and Ω as

$$\nabla \cdot \mu \left(\vec{T} - \nabla \Omega \right) = 0. \quad (3.41)$$

Equation (3.35) is also rewritten in terms of \vec{T} and Ω using equations (3.37), (3.38) and (3.40) to produce

$$\nabla \times (\sigma^{-1} \nabla \times \vec{T}) = -\frac{\partial}{\partial t} \left[\mu (\vec{T} - \nabla \Omega) \right]. \quad (3.42)$$

For sinusoidally varying quantities taking the partial derivative with respect to time is equivalent to multiplying by $j\omega$, where $j = \sqrt{-1}$, and ω is the angular frequency in radians per second. Thus equation (3.42) can be written in complex phasor notation as

$$\nabla \times (\sigma^{-1} \nabla \times \vec{T}) = -j\omega \left[\mu (\vec{T} - \nabla \Omega) \right]. \quad (3.43)$$

The partial differential equations (3.41) and (3.43) are now expressed in difference form and compared with the system of equations produced by the coupled network method.

For algebraic simplicity we rewrite equation (3.41) as

$$\nabla \cdot \mu \vec{T} - \nabla \cdot \mu \nabla \Omega = 0. \quad (3.44)$$

We now restrict our analysis to those terms required to predict the losses due to the radial component of the magnetic flux density. As stated in Section 3.2, this is achieved by setting the conductivity in the radial direction σ_r to zero and results in only axial and circumferential components in the current density. The induced current density can thus be fully described by choosing an electric vector potential of the form

$$\vec{T} = T_r \hat{r} + 0\hat{\theta} + 0\hat{z} \quad (3.45)$$

Using the central difference approximation and equation (3.45) the first term in equation (3.44) can be written as

$$\mu_r \frac{T_{i+1,j,k} - T_{i-1,j,k}}{2\Delta r} + \frac{\mu_r}{r} T_{i,j,k} \quad (3.46)$$

and the second term as

$$\begin{aligned} & \mu_r \frac{2\Omega_{i,j,k} - \Omega_{i+1,j,k} - \Omega_{i-1,j,k}}{\Delta r^2} + \mu_r \frac{\Omega_{i-1,j,k} - \Omega_{i+1,j,k}}{2r\Delta r} \\ & + \mu_\theta \frac{2\Omega_{i,j,k} - \Omega_{i,j+1,k} - \Omega_{i,j-1,k}}{r^2 \Delta \theta^2} + \mu_z \frac{2\Omega_{i,j,k} - \Omega_{i,j,k+1} - \Omega_{i,j,k-1}}{\Delta z^2} \end{aligned} \quad (3.47)$$

where the subscripts i, j and k represent variations in the radial, circumferential and axial directions, respectively. These two equations are represented in the coupled network formulation by the equation

$$\mathbf{P}\boldsymbol{\Omega} + \mathbf{Q}\mathbf{I} = \boldsymbol{\phi}_{imposed} \quad (3.48)$$

where the $\boldsymbol{\phi}_{imposed}$ terms of equation (3.48) are non-zero only at nodes located at an imposed magnetic flux boundary. For nodes not at the imposed magnetic flux boundary equation (3.48) is reduced to

$$\mathbf{P}\boldsymbol{\Omega} + \mathbf{Q}\mathbf{I} = 0. \quad (3.49)$$

The $\mathbf{P}\boldsymbol{\Omega}$ term in equation (3.49) at a magnetic node i, j, k is given by

$$\begin{aligned} & (\Omega_{i,j,k} - \Omega_{i+1,j,k}) \rho_{ro} + (\Omega_{i,j,k} - \Omega_{i-1,j,k}) \rho_{ri} + (\Omega_{i,j,k} - \Omega_{i,j+1,k}) \rho_{\theta} + (\Omega_{i,j,k} - \Omega_{i,j-1,k}) \rho_{\theta} \\ & + (\Omega_{i,j,k} - \Omega_{i,j,k+1}) \rho_z + (\Omega_{i,j,k} - \Omega_{i,j,k-1}) \rho_z, \end{aligned} \quad (3.50)$$

where the permeances are defined by

$$\rho_{ro} = \frac{\mu_r \left(r + \frac{\Delta r}{2}\right) \Delta \theta \Delta z}{\Delta r}, \quad (3.51)$$

$$\rho_{ri} = \frac{\mu_r \left(r - \frac{\Delta r}{2}\right) \Delta \theta \Delta z}{\Delta r}, \quad (3.52)$$

$$\rho_{\theta} = \frac{\mu_{\theta} \Delta r \Delta z}{r \Delta \theta}, \quad (3.53)$$

$$\rho_z = \frac{\mu_z r \Delta \theta \Delta r}{\Delta z}. \quad (3.54)$$

Substituting (3.51), (3.52), (3.53) and (3.54) into equation (3.50) and simplifying results in the expression

$$\begin{aligned} & \mu_r \frac{(2\Omega_{i,j,k} - \Omega_{i+1,j,k} - \Omega_{i-1,j,k}) r \Delta \theta \Delta z}{\Delta r} + \mu_r \frac{(\Omega_{i-1,j,k} - \Omega_{i+1,j,k}) \Delta \theta \Delta z}{2} \\ & + \mu_{\theta} \frac{(2\Omega_{i,j,k} - \Omega_{i,j+1,k} - \Omega_{i,j-1,k}) \Delta r \Delta z}{r \Delta \theta} + \mu_z \frac{(2\Omega_{i,j,k} - \Omega_{i,j,k+1} - \Omega_{i,j,k-1}) r \Delta \theta \Delta r}{\Delta z}, \end{aligned} \quad (3.55)$$

and dividing each term of (3.55) by $r \Delta \theta \Delta r \Delta z$ gives

$$\begin{aligned} & \mu_r \frac{(2\Omega_{i,j,k} - \Omega_{i+1,j,k} - \Omega_{i-1,j,k})}{\Delta r^2} + \mu_r \frac{(\Omega_{i-1,j,k} - \Omega_{i+1,j,k})}{2r \Delta r} \\ & + \mu_{\theta} \frac{(2\Omega_{i,j,k} - \Omega_{i,j+1,k} - \Omega_{i,j-1,k})}{r^2 \Delta \theta^2} + \mu_z \frac{(2\Omega_{i,j,k} - \Omega_{i,j,k+1} - \Omega_{i,j,k-1})}{\Delta z^2}. \end{aligned} \quad (3.56)$$

Comparing the expressions given in (3.56) and (3.47) it can be seen that $\mathbf{P}\Omega/(r\Delta r\Delta\theta\Delta z)$ and the finite difference form of $-\nabla \cdot \mu\nabla\Omega$ result in the same nodal expressions for Ω .

In the coupled network formulation setting σ_r to zero results in a series of isolated electric planar networks. Using equations (3.14) and (3.15) the \mathbf{QI} term of equation (3.49) expressed about magnetic node i, j, k is given by

$$\rho_{ro}I_{i,j,k} - \rho_{ri}I_{i-1,j,k} \quad (3.57)$$

where the loop currents are as shown in Figure 3.12 and the permeances are those given by equations (3.51) and (3.52).

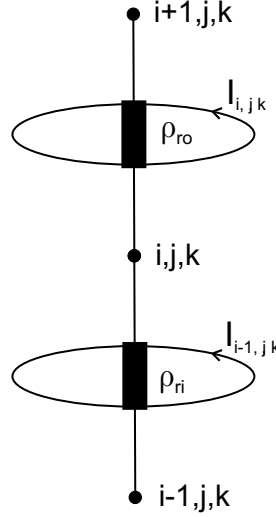


Figure 3.12: Permeance branches with their associated loop currents.

Substituting the permeance expressions given in (3.51) and (3.52) into equations (3.57) and simplifying gives

$$\frac{\mu_r}{\Delta r} (I_{i,j,k} - I_{i-1,j,k}) r\Delta\theta\Delta z + \mu_r \frac{(I_{i,j,k} + I_{i-1,j,k})}{2} \Delta\theta\Delta z \quad (3.58)$$

and dividing by $r\Delta\theta\Delta r\Delta z$ results in

$$\frac{\mu_r}{\Delta r} \frac{(I_{i,j,k} - I_{i-1,j,k})}{\Delta r} + \frac{\mu_r}{2r} \frac{(I_{i,j,k} + I_{i-1,j,k})}{\Delta r}. \quad (3.59)$$

The coupled network formulation is based on a series of “magnetic nodes” (at which we solve for Ω) and a series of loop currents which enclose the magnetic branches connecting

these nodes. The finite difference method however is based only on a discretising grid and its associated nodes. For consistency between the two methods we define a “branch electric vector potential” \tilde{T} in terms of the adjacent node potentials as

$$\tilde{T}_{i,j,k} = \frac{(T_{i,j,k} + T_{i+1,j,k})}{2}. \quad (3.60)$$

Equation (3.46) is rewritten in terms of branch potentials to give

$$\frac{\mu_r}{\Delta r} \left(\tilde{T}_{i,j,k} - \tilde{T}_{i-1,j,k} \right) + \frac{\mu_r}{2r} \left(\tilde{T}_{i,j,k} + \tilde{T}_{i-1,j,k} \right). \quad (3.61)$$

Comparing equations (3.59) and (3.61) it can be seen that these equations are the same where

$$I_{i,j,k} = \tilde{T}_{i,j,k} \Delta r \quad (3.62)$$

It should be noted that in order to write equation (3.61) from equation (3.46) the approximation

$$\frac{\mu_r T_{i,j,k}}{r} = \frac{\mu_r (T_{i+1,j,k} + T_{i-1,j,k})}{2r} \quad (3.63)$$

was made. The error introduced by making this approximation is given by

$$\begin{aligned} E &= \frac{\mu_r (T_{i+1,j,k} + T_{i-1,j,k})}{2r} - \frac{2\mu_r T_{i,j,k}}{2r} \\ &= \frac{\mu_r (T_{i+1,j,k} - 2T_{i,j,k} + T_{i-1,j,k})}{2r} \\ &\approx \frac{\mu_r \Delta r^2}{2r} \frac{\partial^2 T}{\partial r^2}. \end{aligned} \quad (3.64)$$

It can be seen from equation (3.64) that using such an approximation will result in a system which is second order accurate. This is reasonable as the central difference approximation used in the finite difference formulations is of the same order of accuracy.

We now compare the finite difference and coupled network solutions to equation (3.43).

Substituting (3.45) into equation (3.43) and expanding the left hand side gives

$$\begin{aligned} \hat{r} \left(-\frac{1}{r^2 \sigma_z} \frac{\partial^2 T_r}{\partial \theta^2} - \frac{1}{\sigma_\theta} \frac{\partial^2 T_r}{\partial z^2} \right) + \hat{\theta} \left(\frac{1}{r \sigma_z} \frac{\partial^2 T_r}{\partial \theta \partial r} - \frac{1}{r^2 \sigma_z} \frac{\partial T_r}{\partial \theta} + \lim_{\sigma_r \rightarrow 0} \left[\frac{1}{r \sigma_r} \frac{\partial^2 T_z}{\partial z \partial \theta} - \frac{1}{\sigma_r} \frac{\partial^2 T_\theta}{\partial z^2} \right] \right) + \\ \hat{z} \left(\frac{1}{\sigma_\theta} \frac{\partial^2 T_r}{\partial z \partial r} + \frac{1}{r \sigma_\theta} \frac{\partial T_r}{\partial z} + \lim_{\sigma_r \rightarrow 0} \left[\frac{1}{r \sigma_r} \frac{\partial^2 T_\theta}{\partial \theta \partial z} - \frac{1}{r^2 \sigma_r} \frac{\partial^2 T_z}{\partial \theta^2} \right] \right) \end{aligned} \quad (3.65)$$

and similarly the right hand side of equation (3.43) becomes

$$-j\omega\mu_r T_r \hat{r} + j\omega \left[\mu_r \frac{\partial \Omega}{\partial r} \hat{r} + \frac{\mu_\theta}{r} \frac{\partial \Omega}{\partial \theta} \hat{\theta} + \mu_z \frac{\partial \Omega}{\partial z} \hat{z} \right]. \quad (3.66)$$

For losses due to the radial component of the magnetic flux density we only need to consider the radial components of (3.65) and (3.66). This means that we do not need to use the limit terms of equation (3.65). However, as shown in Appendix E, if the circumferential or axial components of equation (3.65) are to be used then these terms cannot be neglected.

Equation (3.43) is represented in the coupled network formulation by equation (3.29) which can be rewritten as

$$\begin{aligned} \mathbf{RI} &= -j\omega(\mathbf{SI} + \mathbf{W}\Omega) \\ &= -\tilde{\mathbf{S}}\mathbf{I} - \tilde{\mathbf{W}}\Omega. \end{aligned}$$

The electric vector potential term T_r in equation (3.66) is accounted for in the coupled network formulation by the $\tilde{\mathbf{S}}\mathbf{I}$ matrix equations. The resulting system of equations given by

$$-\mathbf{SI} = -\rho_{ij} I_i \quad (3.67)$$

where the radial permeances ρ_{ij} are defined by

$$\rho_{ij} = \rho_r = \frac{\mu_r \left(r_i + \frac{\Delta r}{2} \right) \Delta \theta \Delta z}{\Delta r} \quad (3.68)$$

and I_i is a loop current circulating around the radial permeance branch between nodes i and j . Substituting (3.68) into (3.67) gives

$$\begin{aligned} -\mathbf{SI} &= -\mu_r \frac{I_i}{\Delta r} (r \Delta \theta \Delta z) \\ &= -\mu_r \tilde{T}_i (r \Delta \theta \Delta z) \end{aligned} \quad (3.69)$$

and thus

$$-\tilde{\mathbf{S}}\mathbf{I} = -j\omega\mathbf{SI} = -j\omega\mu_r \tilde{T}_i (r \Delta \theta \Delta z). \quad (3.70)$$

The substitution $I_i/\Delta r = \tilde{T}_i$ in equation (3.69) can be made as \tilde{T}_i can be interpreted as the loop current per unit length in the radial direction over element \tilde{i} (see Figure 3.13). This relationship was shown in equation (3.62).

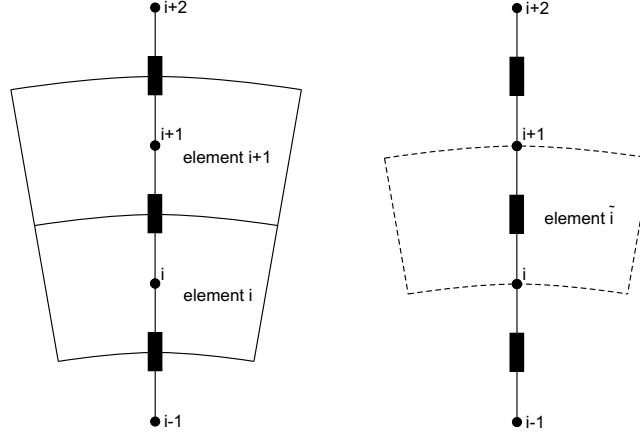


Figure 3.13: Relative positioning of elements.

The radial component of the gradient of the magnetic scalar potential given in (3.66) is accounted for in the coupled network formulation by the $\tilde{\mathbf{W}}\Omega$ terms. For the reduced formulation ($\sigma_r = 0$) the \mathbf{W} matrix contains only radial permeances. The resulting system of equations given by $-\tilde{\mathbf{W}}\Omega$ is

$$-j\omega\rho_r (\Omega_{i,j,k} - \Omega_{i+1,j,k}) = j\omega\mu_r \frac{(\Omega_{i+1,j,k} - \Omega_{i,j,k})}{\Delta r} (r\Delta\theta\Delta z). \quad (3.71)$$

Dividing equation (3.71) by $r\Delta\theta\Delta z$ gives

$$j\omega\mu_r \frac{(\Omega_{i+1,j,k} - \Omega_{i,j,k})}{\Delta r} \quad (3.72)$$

which is the central difference approximation of the $j\omega\mu_r\partial\Omega/\partial r$ term in equation (3.66) expressed about a mid-way node \tilde{i} .

The radial component of expression (3.65) is represented by the term \mathbf{RI} in the coupled network formulation. This can be seen by first expressing the radial component of (3.65) in difference form as shown in equation (3.73).

$$\frac{-1}{r^2\sigma_z} \frac{\tilde{T}_{i,j+1,k} - 2\tilde{T}_{i,j,k} + \tilde{T}_{i,j-1,k}}{\Delta\theta^2} - \frac{1}{\sigma_\theta} \frac{\tilde{T}_{i,j,k+1} - 2\tilde{T}_{i,j,k} + \tilde{T}_{i,j,k-1}}{\Delta z^2} \quad (3.73)$$

By substituting the resistance expressions given in equations (3.27) and (3.28) into equation (3.26) and simplifying gives

$$-\frac{r\Delta\theta}{\sigma_\theta\Delta z} \frac{(I_{i,j,k+1} - 2I_{i,j,k} + I_{i,j,k-1})}{\Delta r} - \frac{\Delta z}{\sigma_z r\Delta\theta} \frac{(I_{i,j+1,k} - 2I_{i,j,k} + I_{i,j-1,k})}{\Delta r}. \quad (3.74)$$

Dividing (3.74) by $r\Delta\theta\Delta z$ and writing in terms of T_r reduces the equation to

$$\frac{-1}{\sigma_\theta} \frac{\tilde{T}_{i,j,k+1} - 2\tilde{T}_{i,j,k} + \tilde{T}_{i,j,k-1}}{\Delta z^2} - \frac{1}{r^2\sigma_z} \frac{\tilde{T}_{i,j+1,k} - 2\tilde{T}_{i,j,k} + \tilde{T}_{i,j-1,k}}{\Delta\theta^2} \quad (3.75)$$

which shows that the resulting nodal equations given by $\nabla \times (\sigma^{-1} \nabla \times \tilde{T}_r)$ using the finite difference method (3.73) and the coupled network formulation (3.75) are the same.

3.3.2 Boundary Conditions

The magnetic boundary conditions are as follows,

- 1) magnetic insulation for $r < r_i$ and $r > r_o$,
- 2) magnetic insulation for $z < 0$ and
- 3) imposed magnetic flux density at $z = \delta$.

These boundary conditions are the same as those used in Section 2.1.1. The boundary conditions and domain are shown in Figure 3.14.

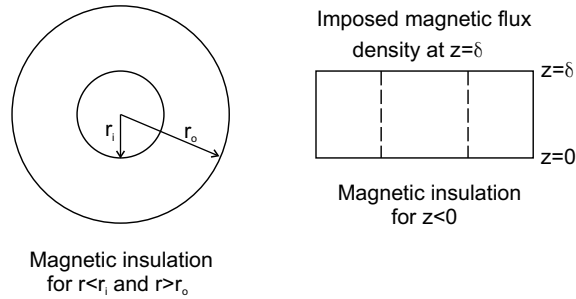


Figure 3.14: Magnetic boundary conditions.

The magnetic insulation boundaries are enforced in the coupled network formulation by the removal of all nodes and permeance branches beyond the domain. This is equivalent to assuming zero permeability outside the domain. In the finite difference formulation the magnetic network is formulated in terms of the magnetic scalar potential Ω which

is solved for at the nodes. A magnetic insulation boundary condition is described by a zero gradient in Ω normal to the boundary. This is equivalent to having an extra node just beyond the domain with the same potential as that of the node at the boundary. For example consider the insulation boundary at the outer radial limit of the domain. If we place an additional node radially outside the boundary and set its potential equal to that of the boundary node then the derivative in the radial direction will equal zero. Substituting $\Omega_{i+1,j,k} = \Omega_{i,j,k}$ into (3.47) and considering only those terms which are differentiated with respect to the radial direction we get

$$\mu_r \frac{\Omega_{i,j,k} - \Omega_{i-1,j,k}}{\Delta r^2} + \mu_r \frac{\Omega_{i-1,j,k} - \Omega_{i,j,k}}{2r\Delta r}, \quad (3.76)$$

Equation (3.76) coupled with the circumferential and axial components of equation (3.47) then defines the finite difference method node equations at the magnetic insulation boundaries. The equivalent coupled network system of equations is given in equation (3.50). Setting ρ_{ro} to zero, substituting (3.52), (3.53) and (3.54) into equation (3.50) and simplifying gives the node boundary equation

$$\begin{aligned} & \mu_r \frac{(\Omega_{i,j,k} - \Omega_{i-1,j,k}) r \Delta \theta \Delta z}{\Delta r} - \mu_r \frac{(\Omega_{i,j,k} - \Omega_{i-1,j,k}) \Delta r \Delta \theta \Delta z}{2\Delta r} \\ & + \mu_\theta \frac{(2\Omega_{i,j,k} - \Omega_{i,j+1,k} - \Omega_{i,j-1,k}) \Delta r \Delta z}{r \Delta \theta} + \mu_z \frac{(2\Omega_{i,j,k} - \Omega_{i,j,k+1} - \Omega_{i,j,k-1}) r \Delta \theta \Delta r}{\Delta z}. \end{aligned} \quad (3.77)$$

Dividing the radial terms of (3.77) by $r \Delta \theta \Delta r \Delta z$ gives

$$\mu_r \frac{\Omega_{i,j,k} - \Omega_{i-1,j,k}}{\Delta r^2} + \mu_r \frac{\Omega_{i-1,j,k} - \Omega_{i,j,k}}{2r\Delta r}. \quad (3.78)$$

Comparing equations (3.76) and (3.78) it is seen that the magnetic insulation boundary condition is imposed in the same way in both the finite difference and coupled network formulations. These same arguments can be used to show that the magnetic insulation boundary conditions at the inner radius ($r = r_i$) and the at lower axial limit ($z = 0$) of the domain also result in the same boundary equations for the two formulations.

In the coupled network formulation the imposed magnetic flux boundary is enforced using a known magnetic flux injection $\phi_{imposed}$ at the nodes located on the boundary $z = \delta$. The imposed magnetic flux at the nodes being calculated as shown in Section

3.1.2. Imposing a node magnetic flux in the finite difference formulation can be achieved by considering an extra set of nodes Δz axially above the boundary $z = \delta$. The scalar potential of these nodes being chosen such that they give a desired gradient in the scalar potential. For an axially imposed magnetic flux density at the boundary the finite difference boundary node equations are derived using the general node equation given by (3.47). For the imposed axial magnetic flux boundary condition we need only consider the axial components of (3.47), i.e.

$$\mu_z \frac{2\Omega_{i,j,k} - \Omega_{i,j,k+1} - \Omega_{i,j,k-1}}{\Delta z^2}. \quad (3.79)$$

Let the boundary node be designated i, j, k and the node Δz axially above be $i, j, k+1$. We choose this node to have a potential $\Omega_{i,j,k+1}$ which will result in the desired imposed magnetic flux at the boundary node. The electric vector potential \vec{T} is zero outside the domain and thus the axial component of the electric field strength \vec{H} is defined by

$$H_z = -\nabla\Omega$$

where the gradient of Ω is taken in the axial direction. This allows the imposed axial magnetic flux density B_z to be expressed as

$$-B_z = \mu_z H_z = -\mu_z \frac{\partial\Omega}{\partial z}. \quad (3.80)$$

The differential term in equation (3.80) is approximated in the region outside the domain by

$$B_z = \mu_z \frac{\Omega_{i,j,k+1} - \Omega_{i,j,k}}{\Delta z}. \quad (3.81)$$

We can now write an expression for the imposed axial magnetic flux ϕ_z at a boundary node in terms of the gradient of the scalar potential. The elementary area normal to the imposed flux density is given by $r\Delta\theta\Delta r$ and thus the imposed axial magnetic flux over an element is given by

$$\begin{aligned} \phi_z &= B_z r \Delta\theta \Delta r \\ &= \mu_z r \Delta\theta \Delta r \frac{\Omega_{i,j,k+1} - \Omega_{i,j,k}}{\Delta z}, \end{aligned} \quad (3.82)$$

which is rearranged to obtain

$$\frac{(\Omega_{i,j,k} - \Omega_{i,j,k+1})}{\Delta z} = \frac{-\phi_z}{\mu_z r \Delta\theta \Delta r}, \quad (3.83)$$

where the left hand side of equation (3.83) is the negative of the difference approximation of the gradient of the scalar potential at the boundary. Expanding (3.79) results in

$$\frac{\mu_z}{\Delta z} \frac{(\Omega_{i,j,k} - \Omega_{i,j,k+1})}{\Delta z} + \mu_z \frac{(\Omega_{i,j,k} - \Omega_{i,j,k-1})}{\Delta z^2}$$

and replacing $(\Omega_{i,j,k} - \Omega_{i,j,k+1})/\Delta z$ with the expression found in equation (3.83) gives

$$\frac{-\phi_z}{r\Delta\theta\Delta r\Delta z} + \mu_z \frac{(\Omega_{i,j,k} - \Omega_{i,j,k-1})}{\Delta z^2}. \quad (3.84)$$

In the coupled network formulation the imposed magnetic flux boundary nodes are defined by equation (3.48). Outside the domain no loop current exist and thus equation (3.48) reduces to

$$P\Omega = \phi_{imposed}. \quad (3.85)$$

For a boundary node i, j, k , with an imposed axial magnetic flux ϕ_z , the axial component of equation (3.85) is

$$\rho_z (\Omega_{i,j,k} - \Omega_{i,j,k-1}) - \phi_z \quad (3.86)$$

where ρ_z is defined by equation (3.54). Substituting equation (3.54) into (3.86) and dividing by $r\Delta\theta\Delta r\Delta z$ gives

$$\mu_z \frac{(\Omega_{i,j,k} - \Omega_{i,j,k-1})}{\Delta z^2} - \frac{\phi_z}{r\Delta\theta\Delta r\Delta z} \quad (3.87)$$

which is the same boundary node equation as that imposed by the finite difference method (see equation (3.84)).

Electric insulation is assumed everywhere outside the domain. The mid-node equations for the electric vector potential \tilde{T}_r using the finite difference and coupled network formulations are given in equations (3.73) and (3.75), respectively. In the coupled network an electric insulation boundary condition is equivalent to setting all loop currents to zero outside the domain. It was shown in Section 3.3.1 that the reduced electric vector potential \tilde{T}_r can be thought of as the loop currents per unit length in the radial direction over each element. This means that \tilde{T}_r is also zero outside the domain which is not surprising since \vec{J} will be equal to zero in this region. At the domain boundaries $z = 0$ and $z = \delta$ this is enforced in equations (3.73) and (3.75) by setting $\tilde{T}_{i,j,k+1}$ to

zero at $z = \delta$ and $\tilde{T}_{i,j,k-1}$ to zero at $z = 0$. At both boundaries the resulting boundary node equations for the two formulations are the same.

It was shown in equations (3.76) and (3.78) that the magnetic insulation boundary conditions at the domain radial limit $r = r_o$ results in the same boundary node equation for the magnetic scalar potential Ω in both the finite difference and coupled network formulations. We must now consider the influence of the electric vector potential terms on the node equations at the radial boundaries. These additional terms are given by equations (3.59) and (3.61) for the coupled network and finite difference methods, respectively. In both formulations an electric insulation boundary at $r = r_o$ can be imposed by setting $I_{i,j,k} = \tilde{T}_{i,j,k} = 0$ where the subscript i denotes the mid-node radially outside the domain boundary. In either case it can be seen from equations (3.59) and (3.61) that this will result in the same boundary node equation. This will also be the case at the inner radial boundary $r = r_i$ in which case we would set $I_{i-1,j,k} = \tilde{T}_{i-1,j,k} = 0$. It should also be noted that due to the decoupling of the electric networks in the radial direction equations (3.73) and (3.75) do not contain $\tilde{T}_{i\pm 1,j,k}$ terms. This means that these equations do not contain boundary terms.

3.3.3 Loop Currents and the Electric Vector Potential

For the reduced electric vector potential $\vec{T} = \tilde{T}_r \hat{r}$ the radial component of the magnetic flux density is described by

$$B_r = \mu_r H_r = \mu_r \left(\tilde{T}_r - \nabla_r \Omega \right) \quad (3.88)$$

in accordance with equation (3.40) and the constitutive relationship (3.37). The radial magnetic flux ϕ_r flowing in an elementary area $r\Delta\theta\Delta z$ is given by

$$\begin{aligned} \phi_r &= B_r r \Delta\theta \Delta z \\ &= \mu_r r \Delta\theta \Delta z \left(\tilde{T}_r - \nabla_r \Omega \right) \\ &= \mu_r r \Delta\theta \Delta z \tilde{T}_r - \frac{\mu_r r \Delta\theta \Delta z}{\Delta r} (\Omega_{i+1,j,k} - \Omega_{i,j,k}) \\ &= \rho_r \Delta r \tilde{T}_r + \rho_r (\Omega_{i,j,k} - \Omega_{i+1,j,k}). \end{aligned} \quad (3.89)$$

The relationship between the electric vector potential \tilde{T}_r , the magnetic scalar potential Ω and the magnetic branch flux ϕ_r can be seen from equation (3.89). In the coupled network formulation \tilde{T}_r are loop currents per unit length in the radial direction. These loop currents modify the branch magnetic flux as shown in Figures 3.7 and 3.8. Equation (3.18) defines the interaction between the magnetic and electric circuits used in the coupled network formulation. Comparing equations (3.18) and (3.89) it can be seen that these are the same if the substitution $I = \Delta r \tilde{T}_r$ is made in equation (3.18).

3.3.4 Comparing Formulations

It was shown in Section 3.3.1 that the node equations for the magnetic scalar potential Ω and the reduced electric vector potential $\vec{T} = \tilde{T}_r$ given by:

- 1) $\frac{\mathbf{P}\Omega}{r\Delta r\Delta\theta\Delta z}$ and $-\nabla \cdot \mu\nabla\Omega$,
- 2) $\frac{\mathbf{Q}\mathbf{I}}{r\Delta r\Delta\theta\Delta z}$ and $\nabla \cdot \mu\tilde{\mathbf{T}}_r$,
- 3) $\frac{\mathbf{R}\mathbf{I}}{r\Delta\theta\Delta z}$ and $\nabla \times (\sigma^{-1}\nabla \times \tilde{\mathbf{T}}_r)$,
- 4) $\frac{-\tilde{\mathbf{S}}\mathbf{I} - \tilde{\mathbf{W}}\Omega}{r\Delta\theta\Delta z}$ and $-j\omega\mu(\tilde{\mathbf{T}}_r - \nabla\Omega)$

are the same. The $T - \Omega$ quasi-static formulation requires equations (3.41) and (3.43) to be solved simultaneously. The coupled network formulation requires equations (3.13) and (3.29) to be solved simultaneously. Thus the coupled network formulation and the finite difference method result in practically the same system of equations for both the magnetic scalar potential and the electric vector potential at the nodes. It was also shown in Section 3.3.2 that the two methods result in the same set of node equations for the imposed boundary conditions. Thus it can be concluded that the reduced coupled network formulation presented here is really just an application of the finite difference method.

3.4 Axiperiodic Formulation

A slotless axial flux machine core can be modeled by considering only a single plane of fixed angular position. This simplification can be made because of the angular periodicity in the core-air gap boundary condition and the uniformity of the core in the circumferential direction. It is shown in Appendix D that if the boundary condition (excitation) is sinusoidal in the circumferential direction then all resulting fields are also sinusoidal in the circumferential direction. Reducing the three dimensional problem to a two dimensional axiperiodic problem offers significant savings in the number of nodes and thus unknowns required to describe the fields in the core. The $T - \Omega$ formulation is chosen here and is expressed in terms of a coupled network (or finite difference) system

An axiperiodic model of a restricted coupled network formulation is used. The restricted network being formed by a full three dimensional magnetic reluctance network coupled with a series of planar resistance networks. This formulations is chosen to provide a prediction of the induced core losses caused by the radial component of the magnetic flux density. The planar resistive network is the result of setting the radial component of the core conductivity σ_r to zero. A validation of this restriction is provided in Chapter 4.

3.4.1 The Magnetic Node Equation

We will now derive the axiperiodic coupled network formulation for the magnetic node equation

$$\mathbf{P}\boldsymbol{\Omega} + \mathbf{Q}\mathbf{I} = \phi_{\text{imposed}}.$$

The core is discretised in the radial and axial directions within a chosen cutting plane as shown in Figure 3.15. Figure 3.16 shows the elementary volumes used in the discretisation as well as the magnetic node associated with elementary volume j .

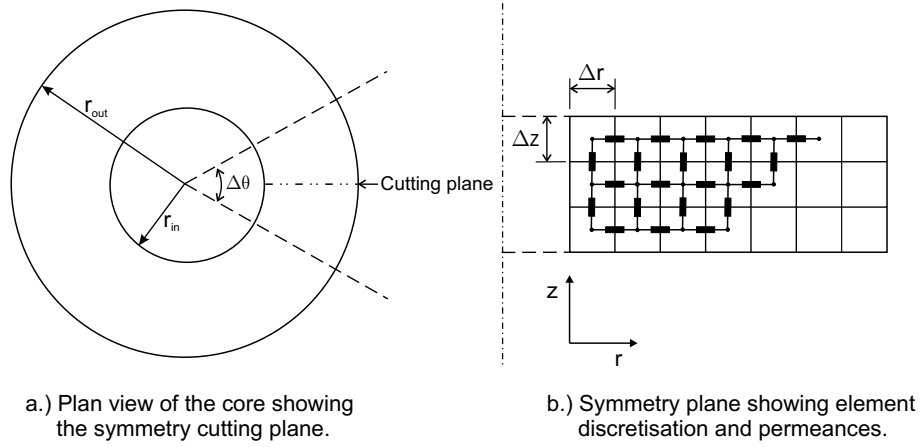


Figure 3.15: Axial symmetry plane and discretisation

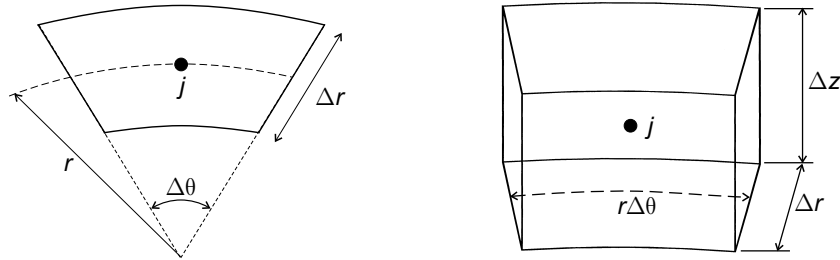


Figure 3.16: Element structure.

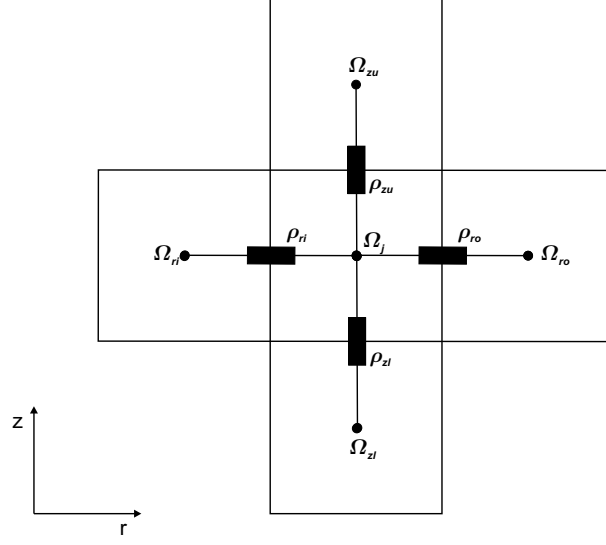
Volume elements are considered in the limit of $\Delta\theta \rightarrow 0$. Element permeances in the limit are defined as

$$\Delta\rho_r = \frac{\mu_r r \Delta\theta \Delta z}{\Delta r}, \quad (3.90)$$

$$\Delta\rho_\theta = \frac{\mu_\theta \Delta r \Delta z}{r \Delta\theta}, \quad (3.91)$$

$$\Delta\rho_z = \frac{\mu_z r \Delta\theta \Delta r}{\Delta z}, \quad (3.92)$$

where the subscripts r, θ, z denote the radial, circumferential and axial directions, respectively. The permeances connected from node j to adjacent nodes are shown in Figure 3.17. Circumferentially displaced nodes located in planes at $\theta \pm \Delta\theta$ (not shown in Figure 3.17) are represented by $\Omega_{\theta l}$ at $(\theta - \Delta\theta)$ and $\Omega_{\theta r}$ at $(\theta + \Delta\theta)$.

Figure 3.17: r - z plane node configuration and permeance connections.

Conservation of magnetic flux at node j requires that

$$(\Omega_j - \Omega_{ri}) \Delta\rho_{ri} + (\Omega_j - \Omega_{ro}) \Delta\rho_{ro} + (\Omega_j - \Omega_{zu}) \Delta\rho_{zu} + (\Omega_j - \Omega_{zl}) \Delta\rho_{zl} \\ + (\Omega_j - \Omega_{\theta l}) \Delta\rho_{\theta l} + (\Omega_j - \Omega_{\theta r}) \Delta\rho_{\theta r} - I_{ri} \Delta\rho_{ri} + I_j \Delta\rho_{ro} = \Delta\Phi_j, \quad (3.93)$$

where I_{ri} and I_j are the loop currents circulating around permeance branches ρ_{ri} and ρ_{ro} , respectively, and $\Delta\Phi_j$ is the imposed magnetic flux at node j . For regular elements of a fixed volume (i.e. constant Δr , $\Delta\theta$ and Δz) the radial and axial permeances shown in Figure 3.17 are given by the permeance expressions of equations (3.90) and (3.92). In the circumferential direction the permeances $\Delta\rho_{\theta l}$ and $\Delta\rho_{\theta r}$ are equal to $\Delta\rho_{\theta}$ given in (3.91), and thus equation (3.93) becomes

$$(\Omega_j - \Omega_{ri}) \Delta\rho_r|_{r-\frac{\Delta r}{2}} + (\Omega_j - \Omega_{ro}) \Delta\rho_r|_{r+\frac{\Delta r}{2}} + (\Omega_j - \Omega_{zu}) \Delta\rho_z + (\Omega_j - \Omega_{zl}) \Delta\rho_z - \\ I_{ri} \Delta\rho_r|_{r-\frac{\Delta r}{2}} + I_j \Delta\rho_r|_{r+\frac{\Delta r}{2}} + (2\Omega_j - \Omega_{\theta l} - \Omega_{\theta r}) \Delta\rho_{\theta} = \Delta\Phi_j. \quad (3.94)$$

A Taylor series expansion is taken about θ to express $\Omega_{\theta l}$ and $\Omega_{\theta r}$ as

$$\Omega_{\theta l} = \Omega_j - \frac{\partial\Omega_j}{\partial\theta} \Delta\theta + \frac{\partial^2\Omega_j}{\partial\theta^2} \frac{\Delta\theta^2}{2} + \dots \quad (3.95)$$

and

$$\Omega_{\theta r} = \Omega_j + \frac{\partial\Omega_j}{\partial\theta} \Delta\theta + \frac{\partial^2\Omega_j}{\partial\theta^2} \frac{\Delta\theta^2}{2} + \dots, \quad (3.96)$$

respectively. Substituting these expressions into equation (3.94) and dividing by $\Delta\theta$ we obtain

$$\begin{aligned} (\Omega_j - \Omega_{ri}) \rho'_r \Big|_{r-\frac{\Delta r}{2}} + (\Omega_j - \Omega_{ro}) \rho'_r \Big|_{r+\frac{\Delta r}{2}} + (\Omega_j - \Omega_{zu}) \rho'_z \Big|_r + (\Omega_j - \Omega_{zl}) \rho'_z \Big|_r - \\ I_{ri} \rho'_r \Big|_{r-\frac{\Delta r}{2}} + I_j \rho'_r \Big|_{r+\frac{\Delta r}{2}} - \frac{\partial^2 \Omega_j}{\partial \theta^2} \rho'_\theta \Big|_r = \frac{\Delta \Phi_j}{\Delta \theta}, \end{aligned} \quad (3.97)$$

where

$$\rho'_r = \frac{\mu_r r \Delta z}{\Delta r}, \quad (3.98)$$

$$\rho'_\theta = \frac{\mu_\theta \Delta r \Delta z}{r}, \quad (3.99)$$

$$\rho'_z = \frac{\mu_z r \Delta r}{\Delta z}. \quad (3.100)$$

The imposed magnetic flux at node j is given by

$$\Delta \Phi_j = B(\theta) r \Delta \theta \Delta r, \quad (3.101)$$

where $B(\theta)$ is the imposed axial magnetic flux density. The right-hand term of equation (3.94) is then

$$\Phi'_j = B(\theta) r \Delta r \quad (3.102)$$

and thus equation (3.97) becomes

$$\begin{aligned} (\Omega_j - \Omega_{ri}) \rho'_r \Big|_{r-\frac{\Delta r}{2}} + (\Omega_j - \Omega_{ro}) \rho'_r \Big|_{r+\frac{\Delta r}{2}} + (\Omega_j - \Omega_{zu}) \rho'_z \Big|_r + (\Omega_j - \Omega_{zl}) \rho'_z \Big|_r - \\ I_{ri} \rho'_r \Big|_{r-\frac{\Delta r}{2}} + I_j \rho'_r \Big|_{r+\frac{\Delta r}{2}} - \frac{\partial^2 \Omega_j}{\partial \theta^2} \rho'_\theta \Big|_r = B(\theta) r \Delta r. \end{aligned} \quad (3.103)$$

Sinusoidal variation in the angular component θ is assumed and thus the second derivative of the scalar potential with respect to θ at node j will be given by

$$\frac{\partial^2 \Omega_j}{\partial \theta^2} = -\Omega_j \left(\frac{p}{2}\right)^2. \quad (3.104)$$

Substituting (3.104) into equation (3.103) leads to

$$\begin{aligned} (\Omega_j - \Omega_{ri}) \rho'_r \Big|_{r-\frac{\Delta r}{2}} + (\Omega_j - \Omega_{ro}) \rho'_r \Big|_{r+\frac{\Delta r}{2}} + (\Omega_j - \Omega_{zu}) \rho'_z \Big|_r + (\Omega_j - \Omega_{zl}) \rho'_z \Big|_r - \\ I_{ri} \rho'_r \Big|_{r-\frac{\Delta r}{2}} + I_j \rho'_r \Big|_{r+\frac{\Delta r}{2}} + \Omega_j \left(\frac{p}{2}\right)^2 \rho'_\theta \Big|_r = B(\theta) r \Delta r, \end{aligned} \quad (3.105)$$

which is rearranged to give

$$\begin{aligned} \Omega_j \left(\rho'_r \Big|_{r-\frac{\Delta r}{2}} + \rho'_r \Big|_{r+\frac{\Delta r}{2}} + 2 \rho'_z \Big|_r + \left(\frac{p}{2}\right)^2 \rho'_\theta \Big|_r \right) - \Omega_{ri} \rho'_r \Big|_{r-\frac{\Delta r}{2}} - \Omega_{ro} \rho'_r \Big|_{r+\frac{\Delta r}{2}} - \\ \Omega_{zu} \rho'_z \Big|_r - \Omega_{zl} \rho'_z \Big|_r - I_{ri} \rho'_r \Big|_{r-\frac{\Delta r}{2}} + I_j \rho'_r \Big|_{r+\frac{\Delta r}{2}} = B(\theta) r \Delta r, \end{aligned} \quad (3.106)$$

From equation (3.106) it can be seen that the diagonal entries of the permeance matrix \mathbf{P} for the axiperiodic formulation are given by

$$\mathbf{P}(j, j) = \rho'_r \Big|_{r-\frac{\Delta r}{2}} + \rho'_r \Big|_{r+\frac{\Delta r}{2}} + 2\rho'_z \Big|_r + \left(\frac{p}{2}\right)^2 \rho'_\theta \Big|_r \quad (3.107)$$

and the off-diagonal entries will be the negative of the branch permeance connecting node j to its adjacent nodes, where all branch permeances are found using equations (3.98) through (3.100).

It can also be seen from equation (3.106) that the \mathbf{Q} matrix will be formed using

$$Q(j, j) = \rho'_r \Big|_{r+\frac{\Delta r}{2}} \quad (3.108)$$

and

$$Q(j, ri) = -\rho'_r \Big|_{r-\frac{\Delta r}{2}}. \quad (3.109)$$

3.4.2 The Electric Loop Equation

We now consider the electric loop equation

$$\tilde{\mathbf{W}}\mathbf{\Omega} + (\mathbf{R} + \tilde{\mathbf{S}})\mathbf{I} = \mathbf{0}$$

for the axiperiodic formulation. Nodes in the electric network are regularly spaced with distances between adjacent nodes equal to Δr , Δz and $\Delta\theta$ in the radial, axial and circumferential directions, respectively. Because a radially staggered grid between the magnetic and electric networks is used, if the coordinates of the magnetic nodes are (r_m, θ_m, z_m) , then the coordinates of the electric nodes will be given by $(r_m \pm \Delta r/2, \theta_m \pm \Delta\theta/2, z_m \pm \Delta z/2)$.

As was the case in the magnetic node equation, the volume elements of the electric network are considered in the limit $\Delta\theta \rightarrow 0$. Element resistances are defined by

$$\Delta R_z = \frac{\Delta z}{\sigma_z r \Delta\theta \Delta r}, \quad (3.110)$$

$$\Delta R_\theta = \frac{r \Delta\theta}{\sigma_\theta \Delta z \Delta r}, \quad (3.111)$$

where the subscripts r, θ, z denote the radial, circumferential and axial directions, respectively. The path in which loop current I_j flows is shown in Figure 3.18.

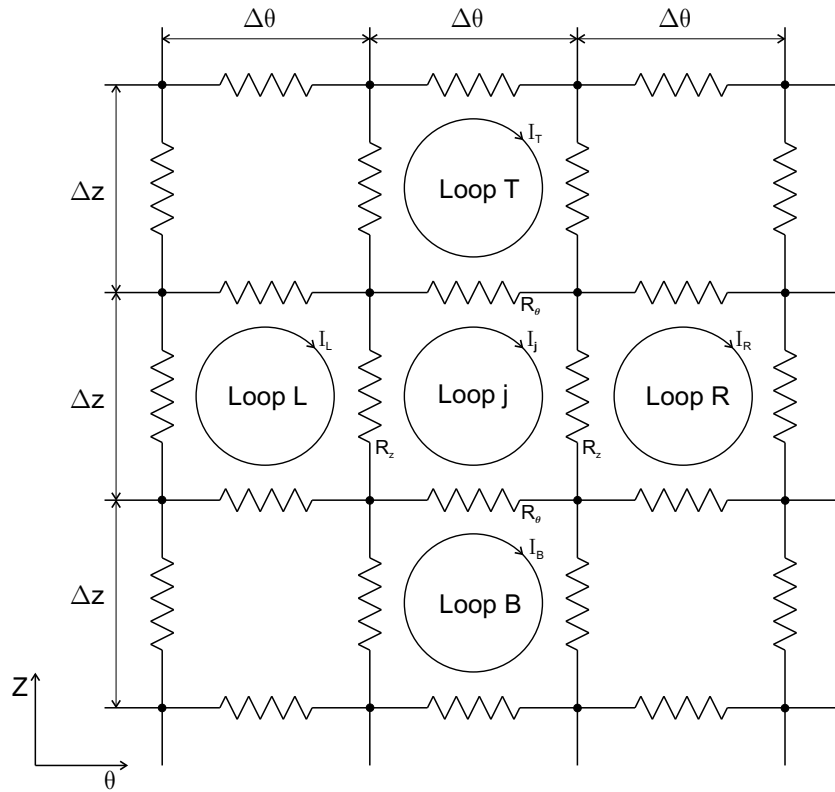


Figure 3.18: Electric network.

Applying Kirchhoff's voltage law and Faraday's law around loop j gives the loop equation

$$(I_j - I_T) \Delta R_\theta + (I_j - I_B) \Delta R_\theta + (I_j - I_L) \Delta R_z + (I_j - I_R) \Delta R_z = -\frac{\partial \Delta\phi_j}{\partial t}, \quad (3.112)$$

where $\Delta\phi_j$ is the flux flowing magnetic branch j which links electric loop j taken in the limit $\Delta\theta \rightarrow 0$.

It was shown in Section 3.2 that the electric loop equation used in the coupled network formulation can be used to rewrite equation (3.112) as

$$\mathbf{RI} = -j\omega(\mathbf{W}\boldsymbol{\Omega} + \mathbf{SI}), \quad (3.113)$$

where \mathbf{RI} is the left hand side of equation (3.112) and the right hand side is represented by $-j\omega(\mathbf{W}\boldsymbol{\Omega} + \mathbf{SI})$. The elements of the \mathbf{W} and \mathbf{S} matrices are defined in equations (3.20) through (3.22). Equation (3.112) can thus be rewritten as

$$(I_j - I_T) \Delta R_\theta + (I_j - I_B) \Delta R_\theta + (I_j - I_L) \Delta R_z + (I_j - I_R) \Delta R_z = -j\omega [(\Omega_j - \Omega_{ro}) \Delta \rho_{ro} + I_j \Delta \rho_{ro}], \quad (3.114)$$

where $\Delta \rho_{ro}$ is defined by equation (3.90) at $r = r_j + \Delta r/2$.

A Taylor series expansion is taken about θ to express I_R and I_L as

$$I_R = I_j + \frac{\partial I_j}{\partial \theta} \Delta \theta + \frac{\partial^2 I_j}{\partial \theta^2} \frac{\Delta \theta^2}{2} + \dots \quad (3.115)$$

and

$$I_L = I_j - \frac{\partial I_j}{\partial \theta} \Delta \theta + \frac{\partial^2 I_j}{\partial \theta^2} \frac{\Delta \theta^2}{2} + \dots, \quad (3.116)$$

respectively. Substituting equations (3.115) and (3.116) into equation (3.114) and dividing by $\Delta \theta$ we obtain

$$(I_j - I_T) R'_\theta + (I_j - I_B) R'_\theta - \frac{\partial^2 I_j}{\partial \theta^2} R'_z = -j\omega (\Omega_j - \Omega_{ro} + I_j) \rho'_r \Big|_{r+\frac{\Delta r}{2}}, \quad (3.117)$$

where

$$R'_\theta = \frac{r}{\sigma_\theta \Delta z \Delta r}, \quad (3.118)$$

$$R'_z = \frac{\Delta z}{\sigma_z r \Delta r} \quad (3.119)$$

and ρ'_r is defined by equation (3.98).

Due to the sinusoidal variations in the loop currents I_j with angular displacement θ we can write the second derivative term in equation (3.117) as

$$\frac{\partial^2 I_j}{\partial \theta^2} = -\left(\frac{p}{2}\right)^2 I_j, \quad (3.120)$$

where p is the number of machine poles. Substituting equation (3.120) into equation (3.117) leads to

$$(I_j - I_T) R'_\theta + (I_j - I_B) R'_\theta + \left(\frac{p}{2}\right)^2 I_j R'_z = -j\omega (\Omega_j - \Omega_{ro} + I_j) \rho'_r \Big|_{r+\frac{\Delta r}{2}}. \quad (3.121)$$

It can be seen from equation (3.121) that the diagonal entries of the resistance matrix \mathbf{R} for the axiperiodic formulation are given by

$$\mathbf{R}(j, j) = 2R'_\theta + \left(\frac{p}{2}\right)^2 R'_z. \quad (3.122)$$

where R'_θ and R'_z are given by equations (3.118) and (3.119), respectively. The off-diagonal entries of \mathbf{R} being equal to $-R'_\theta$ (i.e. the negative of the resistances common to the adjacent loops).

It can also be seen from equation (3.121) that the \mathbf{W} and \mathbf{S} matrices for the axiperiodic formulation are given by

$$W(j, j) = \rho'_r \Big|_{r+\frac{\Delta r}{2}}, \quad (3.123)$$

$$W(j, ro) = -\rho'_r \Big|_{r+\frac{\Delta r}{2}} \quad (3.124)$$

and

$$S(j, j) = \rho'_r \Big|_{r+\frac{\Delta r}{2}}. \quad (3.125)$$

3.4.3 The Axiperiodic System of Equations

The coupled network formulation was described in Section 3.2 and is defined by equation (3.30). The \mathbf{P} , \mathbf{Q} , \mathbf{R} , \mathbf{W} and \mathbf{S} matrices required to write the system of equations for an axiperiodic formulation have been derived in Sections 3.4.2 and 3.4.1. The imposed magnetic flux vector ϕ can be found by using equation (3.102).

Using these matrices, equation (3.30) and the sinusoidal variation in the circumferential direction the magnetic fields and induced currents can be found/approximated at any point within the domain.

3.4.4 Calculating Induced Losses

Induced losses in the coupled network method are calculated using an $I_b^2 R_b$ calculation, where I_b are the resistance network branch currents and R_b the branch resistances in which the current flows. Figure 3.19 shows the relationship between the loop and branch currents.

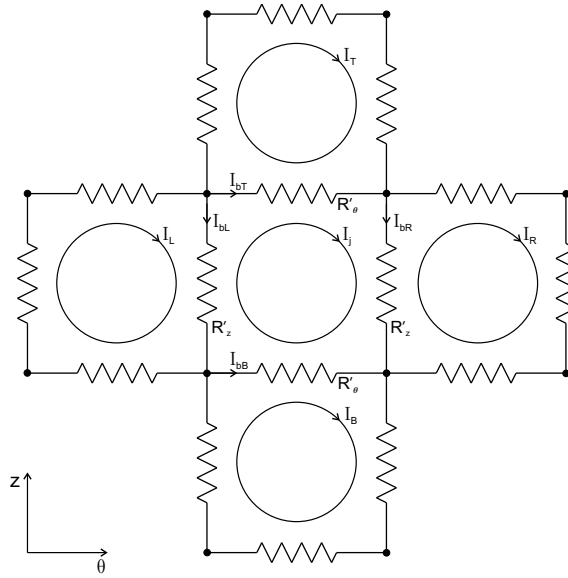


Figure 3.19: Branch current calculation.

The branch currents are calculated using the superposition of the loop currents in common branch resistances. From Figure 3.19 it can be seen that the resulting branch currents are given by

$$I_{bR} = I_j - I_R,$$

$$I_{bB} = I_j - I_B,$$

$$I_{bL} = I_j - I_L,$$

$$I_{bT} = I_j - I_T$$

and the induced losses associated with loop j are thus

$$(I_{bR}^2 + I_{bL}^2) R'_z + (I_{bT}^2 + I_{bB}^2) R'_\theta.$$

For the axiperiodic formulation, we solve for loop currents in the $r - z$ plane with variation in the circumferential direction assumed sinusoidal. The branch currents in the axial resistances are found using the Taylor series expansion given by equation (3.115). The resulting branch current I_{bR} using this expansion can be approximated by

$$\begin{aligned} I_{bR} &= I_j - I_R \\ &\approx \frac{\partial I}{\partial \theta} \Delta \theta. \end{aligned} \quad (3.126)$$

The general form of the loop currents I_j in the circumferential direction are given by

$$I_j = \hat{I}_j \sin\left(\frac{p\theta}{2}\right), \quad (3.127)$$

where p is the number of machine poles and \hat{I}_j is the peak value of I_j . Substituting equation (3.127) into equation (3.126) gives the branch current expression

$$I_{bR} \approx -\hat{I}_j \frac{p\Delta\theta}{2} \cos\left(\frac{p\theta}{2}\right). \quad (3.128)$$

From equations (3.119) and (3.128) the induced losses due to an axial branch resistance R'_z is given by

$$I_{bR}^2 R'_z \approx \hat{I}_j^2 \left(\frac{p}{2}\right)^2 \cos^2\left(\frac{p\theta}{2}\right) \frac{\Delta z \Delta \theta}{\sigma_z r \Delta r} \quad (3.129)$$

and due to a circumferential branch resistance R'_θ by

$$I_{bT}^2 R'_\theta = (I_j - I_T)^2 \frac{r \Delta \theta}{\sigma_\theta \Delta r \Delta z}. \quad (3.130)$$

Using the circumferential periodicity, for a given radius and axial position, the total losses due to axial branch resistances are found by the integral

$$\int_0^{2\pi} \hat{I}_j^2 \left(\frac{p}{2}\right)^2 \cos^2\left(\frac{p\theta}{2}\right) \frac{\Delta z}{\sigma_z r \Delta r} \partial \theta = \frac{\hat{I}_j^2 \pi p^2 \Delta z}{4 \sigma_z r \Delta r} \quad (3.131)$$

and similarly, the losses due to circumferential resistances are found by

$$\int_0^{2\pi} (\hat{I}_j - \hat{I}_T)^2 \sin^2\left(\frac{p\theta}{2}\right) \frac{r}{\sigma_\theta \Delta r \Delta z} \partial \theta = \frac{\pi r}{\sigma_\theta \Delta r \Delta z} (\hat{I}_j - \hat{I}_T)^2. \quad (3.132)$$

The total core losses due to the radial component of the magnetic flux density are calculated using the summation of the values given by equations (3.131) and (3.132)

for all planar resistive networks. This requires a summation over all radii and axial elements used in the discretization.

The restricted axiperiodic coupled network formulation presented here is used in Chapter 4 to predict the induced losses due to the radial flux component as well as its dependence on frequency.

Chapter 4

Core Losses and Magnetic Flux Density Distribution

In Chapter 2 it was concluded that curvature related radial flux density is relatively small compared to the peak axial and circumferential flux densities even when the shielding effect of induced eddy currents is ignored. However, the model used in Chapter 2 was a magnetostatic one and thus could not address the question of power loss resulting from curvature related radial flux.

We will now use a quasi-static electromagnetic model in the form of the axiperiodic coupled network formulation, derived in Chapter 3, to predict classical eddy current loss due to the radial flux component as well as its dependence on frequency. The classical eddy current power loss due to curvature related radial or cross-lamination flux will also be compared with classical eddy current loss due to the main or parallel running flux to show that in most practical instances it can be neglected.

For simplicity and brevity, classical eddy current loss will now be simply referred to as either induced loss, eddy current loss or power loss. In Section 4.5 we will investigate experimental techniques which allow classical eddy current loss to be separated from hysteresis and excess loss.

4.1 Eddy Current Loss Separation

The coupled network formulation derived in Chapter 3 is based on a restricted resistive network formed by setting the core conductivity in the radial direction σ_r to zero. This restriction results in a series of planar resistive networks coupled only to the radial permeance branches of the full three dimensional permeance network. The restricted network is chosen so that the losses due to and frequency dependence of the radial component of the core magnetic flux density can be determined. It is now shown that the power loss due to radial or cross-lamination flux is decoupled from the power loss due to parallel running or main flux and therefore their theoretical evaluations can be performed separately.

Induced currents within a lamination sheet are made up of the superposition of eddy currents due to flux that runs parallel to the lamination faces (or “main” flux) and eddy currents due to cross-lamination flux. Let the distribution of eddy currents due solely to a given distribution of parallel running flux be given by X and similarly, the distribution of eddy currents due solely to a given distribution of cross-lamination flux be given by Y. We now show that the power loss due to eddy current distribution X and that due to eddy current distribution Y are mutually independent and that the interaction between the two eddy current distributions contribute zero net additional power loss.

The power loss density D at any given point within a laminate is given by

$$D = \frac{J_{rp}^2}{\sigma_r} + \frac{(J_{\theta c} + J_{\theta p})^2}{\sigma_\theta} + \frac{(J_{zc} + J_{zp})^2}{\sigma_z}, \quad (4.1)$$

where J_{rp} , $J_{\theta p}$ and J_{zp} are the radial, circumferential and axial components of the induced current density due to parallel running flux, respectively, $J_{\theta c}$ and J_{zc} are the circumferential and axial components of the induced current density due to cross-lamination flux, respectively and σ_r , σ_θ and σ_z are the radial, circumferential and axial components of the material conductivity, respectively.

Expanding the right hand side of equation (4.1) results in

$$D = \frac{J_{rp}^2}{\sigma_r} + \frac{J_{\theta p}^2}{\sigma_\theta} + \frac{J_{zp}^2}{\sigma_z} + \frac{J_{\theta c}^2}{\sigma_\theta} + \frac{J_{zc}^2}{\sigma_z} + \frac{2J_{\theta c}J_{\theta p}}{\sigma_\theta} + \frac{2J_{zc}J_{zp}}{\sigma_z}. \quad (4.2)$$

The first three terms of equation (4.2) represent contributions to power loss density due to parallel running flux alone. The fourth and fifth terms represent contributions to power loss density due to cross-lamination flux alone. The last two terms represent contributions to power loss density which result from the interaction between the two sets of induced currents.

The following realistic assumptions are now made:

- 1) $J_{\theta c}$ and J_{zc} are constant along a radial line within a laminate; and
- 2) If x is measured radially from the laminate centre, as shown in Figure 4.1, then $J_{\theta p}(x) = -J_{\theta p}(-x)$ and $J_{zp}(x) = -J_{zp}(-x)$.

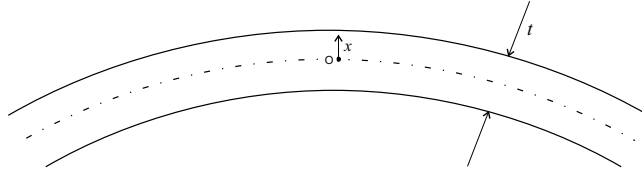


Figure 4.1: Cross-section of a lamination sheet.

Based on these assumptions, it is clear that the last two terms in equation (4.2) do not contribute to the total power loss in the lamination.

The decoupling between power loss due to the parallel running flux and that due to cross-lamination flux allows them to be calculated separately. There are well established methods for the calculation of power loss due to parallel running flux (Lammeraner & Staff, 1966) and these are applicable to the laminated cores of axial flux machines.

Here we will consider only the power loss due to cross-lamination flux. Although cross-lamination and parallel running flux are both present in the model, eddy currents due

to parallel running flux have been eliminated by assuming zero radial conductivity. Whilst this assumption makes power loss due to parallel running flux equal to zero, we have now shown that this will have no effect on the power loss due to cross-lamination flux.

4.2 Main Flux Loss Prediction

An expression for induced power losses due to the time varying main or parallel running flux is now derived. We begin with the following reasonable assumptions:

- a) $B_r = 0$,
- b) B_θ and B_z are independent of radius within a laminate,
- c) $E_r = 0$ (i.e. $\sigma_r = \infty$),
- d) $E_\theta(x) = -E_\theta(-x)$ and
- e) $E_z(x) = -E_z(-x)$,

where B is the magnetic flux density, E is the electric field intensity, σ is the material conductivity, the subscripts r , θ and z denote the radial, circumferential and axial directions, respectively and x represents the radial distance from the laminate centre, as shown in Figure 4.2.

Substituting $E_r = B_r = 0$ into the Maxwell equation

$$\nabla \times \vec{E} = -j\omega\vec{B} \quad (4.3)$$

and expanding results in the following system of equations

$$\frac{1}{r} \frac{\partial E_z}{\partial \theta} - \frac{\partial E_\theta}{\partial z} = 0 \quad (4.4)$$

$$j\omega B_\theta = \frac{\partial E_z}{\partial r} \quad (4.5)$$

$$-j\omega B_z = \frac{1}{r} \frac{\partial (rE_\theta)}{\partial r}. \quad (4.6)$$

Based on assumption b) equation (4.6) can be rewritten as

$$rE_{\theta} = -j\omega B_z \int r dr. \quad (4.7)$$

We now express E_{θ} in terms of x by making the substitution $r = r_c + x$ in equation (4.7) to give

$$\begin{aligned} E_{\theta}(r_c + x) &= -j\omega B_z \int_0^x (r_c + \bar{x}) d\bar{x} \\ &= -j\omega B_z x \left(r_c + \frac{x}{2} \right). \end{aligned} \quad (4.8)$$

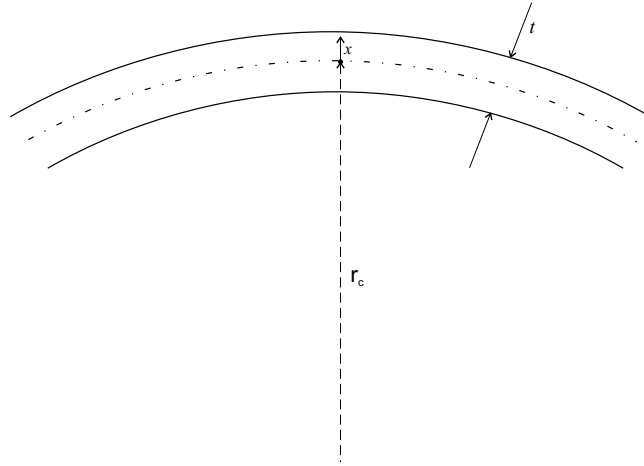


Figure 4.2: Lamination sheet cross-section.

Equation (4.8) is rearranged to give

$$E_{\theta} = -j\omega B_z x \frac{\left(r_c + \frac{x}{2} \right)}{\left(r_c + x \right)}. \quad (4.9)$$

Now $-t/2 \leq x \leq t/2$ and thus for any practical core $x \ll r_c$ which allows us to make the approximation

$$E_{\theta} \approx -j\omega B_z x. \quad (4.10)$$

Similarly, E_z is expressed in terms of x using equation (4.5) to give

$$\begin{aligned} E_z &= \int_0^x j\omega B_{\theta} d\bar{x} \\ &= j\omega B_{\theta} x. \end{aligned} \quad (4.11)$$

The current density within a laminate is found by substituting equations (4.10) and (4.11) into the constitutive relation $\vec{J} = \sigma \vec{E}$ to give

$$\vec{J} = J_r \hat{r} - \sigma_\theta j\omega B_z x \hat{\theta} + \sigma_z j\omega B_\theta x \hat{z}. \quad (4.12)$$

For isotropic material (i.e. $\sigma_\theta = \sigma_z = \sigma$) the power density D is given by

$$\begin{aligned} D &= \vec{E} \cdot \vec{J} \\ &= \sigma (j\omega x)^2 (B_\theta^2 + B_z^2) \\ &= -\sigma \omega^2 x^2 (B_\theta^2 + B_z^2) \end{aligned} \quad (4.13)$$

and the power density averaged in the thin direction of the laminate \tilde{D} is given by

$$\begin{aligned} \tilde{D} &= \frac{2}{t} \int_0^{\frac{t}{2}} D dx \\ &= -\frac{\sigma \omega^2 t^2 (B_\theta^2 + B_z^2)}{12}. \end{aligned} \quad (4.14)$$

From equation (4.14) the time averaged power loss density due to the main flux within a laminated core is found to be

$$F_p = \frac{\sigma \omega^2 t^2}{24} (B_\theta^2 + B_z^2). \quad (4.15)$$

This result is not surprising being the cylindrical co-ordinate form of the well known expression (Lammeraner & Staffl, 1966)

$$F_p = \frac{\sigma \omega^2 t^2}{24} |B|^2. \quad (4.16)$$

Using the 2D magnetic flux density distribution derived in Appendix C and equation (4.15), the main flux losses within a laminated core are given by

$$\begin{aligned} F_p &= \frac{\omega^2 t^2 \sigma}{24} \int_V \left[\left(P \sqrt{k_{z\theta}} \frac{\cosh\left(\frac{gz}{\delta}\right)}{\sinh(g)} \cos(l\theta) \right)^2 + \left(P \frac{\sinh\left(\frac{gz}{\delta}\right)}{\sinh(g)} \sin(l\theta) \right)^2 \right] dV \\ &= \frac{\omega^2 t^2 \sigma P^2 \delta \pi}{24 \cdot 4} \left[k_{z\theta} \int_a^b \frac{r'}{g \sinh^2(g)} [\sinh(2g) + 2g] dr' \right. \\ &\quad \left. + \int_a^b \frac{r'}{g \sinh^2(g)} [\sinh(2g) - 2g] dr' \right], \end{aligned} \quad (4.17)$$

where g , $k_{z\theta}$, a and b are defined in Appendix C. We now redefine g as

$$g = \frac{Gb\sqrt{k_{z\theta}}}{r'}, \quad (4.18)$$

where

$$G = \frac{\delta l}{b}. \quad (4.19)$$

Substituting equation (4.18) into equation (4.17) and rearranging gives

$$F_p = \frac{\omega^2 t^2 \sigma \pi P^2 \delta}{96} \left[\int_a^b \frac{r'^2 \sinh\left(2G\sqrt{k_{z\theta}}\frac{b}{r'}\right)}{Gb\sqrt{k_{z\theta}} \sinh^2\left(G\sqrt{k_{z\theta}}\frac{b}{r'}\right)} (k_{z\theta} + 1) dr' + \int_a^b \frac{2r'}{\sinh^2\left(G\sqrt{k_{z\theta}}\frac{b}{r'}\right)} (k_{z\theta} - 1) dr' \right]. \quad (4.20)$$

It can be seen from equation (4.20) that the core loss density distribution due to the main magnetic flux components are dependent on b/r' , the material permeability ratio $k_{z\theta} = \mu_\theta/\mu_z$ and G . Figure 4.3 shows plots of the integrand of equation (4.20) for varying values of G with $k_{z\theta} = 1$.

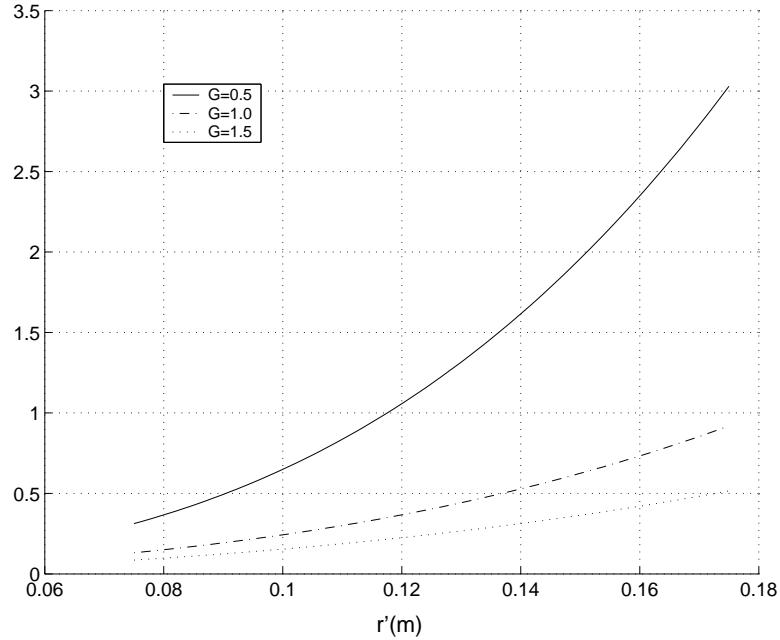


Figure 4.3: Plot of integrand of equation (4.20) for varying G and $k_{z\theta} = 1$.

Axial flux machine designers can use equation (4.20) to directly predict classical eddy current loss due to the main flux or to investigate the loss density distribution with radius for varying values of G . Figure 4.3 allows a machine designer to predict the radial variation in the loss density, averaged in the axial and circumferential directions, for varying physical dimensions and number of poles. The example shown in Figure 4.3 demonstrates that as G falls the loss density distribution tends to increase rapidly towards the outer radius. Integration of the curves given in Figure 4.3 can also be used to give total core loss due the main flux.

4.3 Coupled Network Loss Prediction

The axiperiodic coupled network formulation presented in Section 3.4 has been used to make predictions of the power loss due to curvature related cross-lamination flux. The assumed nominal core characteristics are: $r_i = 0.075$ m, $r_o = 0.175$ m, $\delta = (0.2/p)$ m, $\mu_r = 20\mu_o$, $\mu = \mu_\theta = \mu_z = 1000\mu_o$, $\sigma_r = 0$ S/m, $\sigma_\theta = \sigma_z = 5 \times 10^6$ S/m, $\omega = 100\pi$ rad/s, $t = 0.27$ mm and $\hat{B}_z = 0.7$ T. In practice it would be expected that the core back-iron length δ be progressively reduced with increasing number of poles p . For this reason δ has been chosen to be inversely proportional to the number of poles. Power loss predictions are shown in Table 4.1 and Figure 4.4.

Table 4.1: Power loss due to cross-lamination flux.

Number of poles	Losses (W) for $\mu = 1000\mu_o$	Losses (W) for $\mu = 5000\mu_o$
2	1.62	0.074
4	0.48	0.021
6	0.24	0.011
8	0.14	0.006

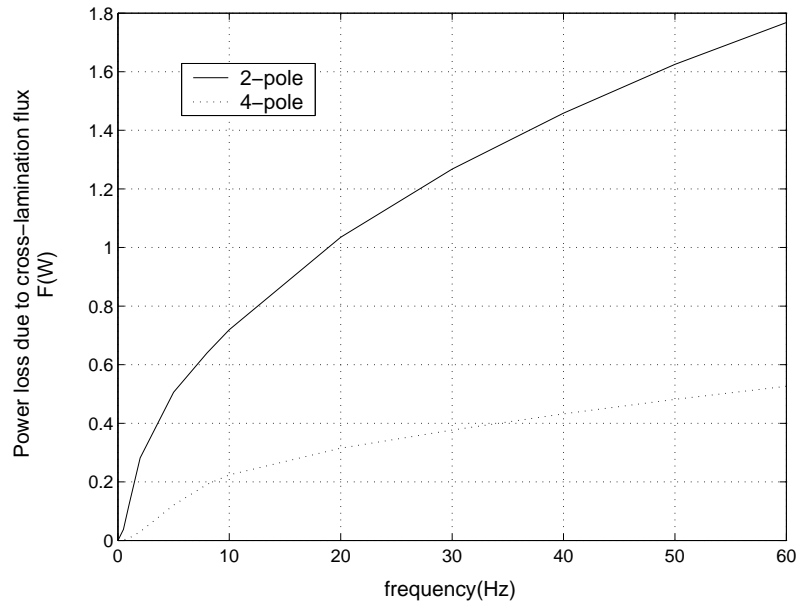


Figure 4.4: Dependence of power loss on frequency.

For comparison, classical eddy-current power loss due to the main flux, F_p , have been evaluated using equation (4.20). These values are given in Table 4.2.

Table 4.2: Power losses due to main flux.

Number of poles	2	4	6	8
$F_p(W)$	6.15	3.07	2.05	1.52

The following observations can be made:

- a) The power loss F has a strong dependence on the number of poles and on the relative permeability of the core.
- b) Except for the two-pole case and at low values of core permeability, the power loss due to cross-lamination flux is insignificant compared to the power loss due to the main flux.
- c) The power loss due to cross-lamination flux may be expressed as

$$F = k\sqrt{f}, \quad (4.21)$$

where k is independent of frequency but is a function of the core physical dimensions, material properties, number of poles and $\hat{B}_z(r)$. Good fits to the curves shown in Figure 4.4 were obtained with k chosen to be 0.2285 and 0.0691 for the 2- and 4- pole cases, respectively.

The explanation for observation c) is based on characteristics of the circumferential component of the induced current which is shown in Figures 4.5 and 4.6. The first point is that the induced current experiences high resistance circumferentially since it is restricted to flow through a thin layer near the flat surfaces of the core because of the skin-effect. The second point is that the total circumferential current (Figure 4.6) is practically independent of frequency. The high circumferential resistance, compared to the axial resistance, implies that practically all the power losses are associated with the circumferential component of current. Thus there exists a current, which is almost independent of frequency, flowing through a cross-sectional area that is proportional to the skin-depth. This implies that the power loss is proportional to the square root of

frequency.

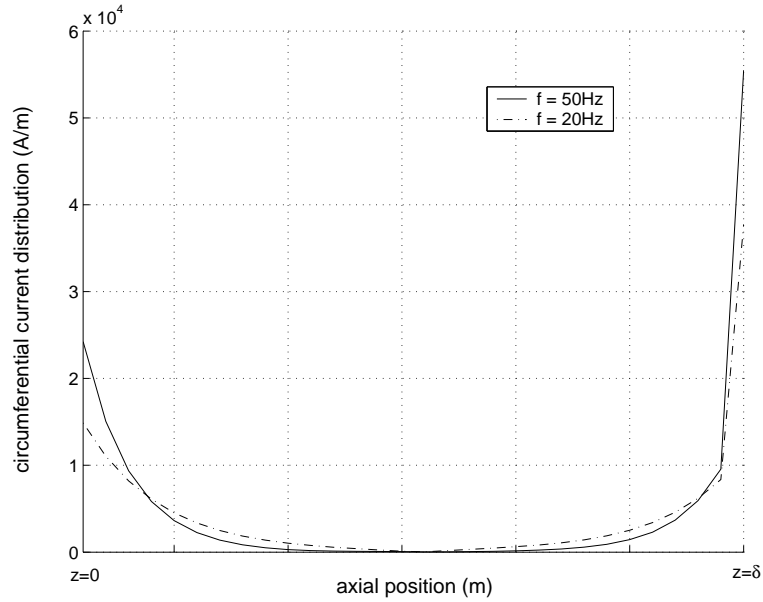


Figure 4.5: Circumferential current distribution (integrated from r_i to r_o) along a pole centre plane (2-pole machine).

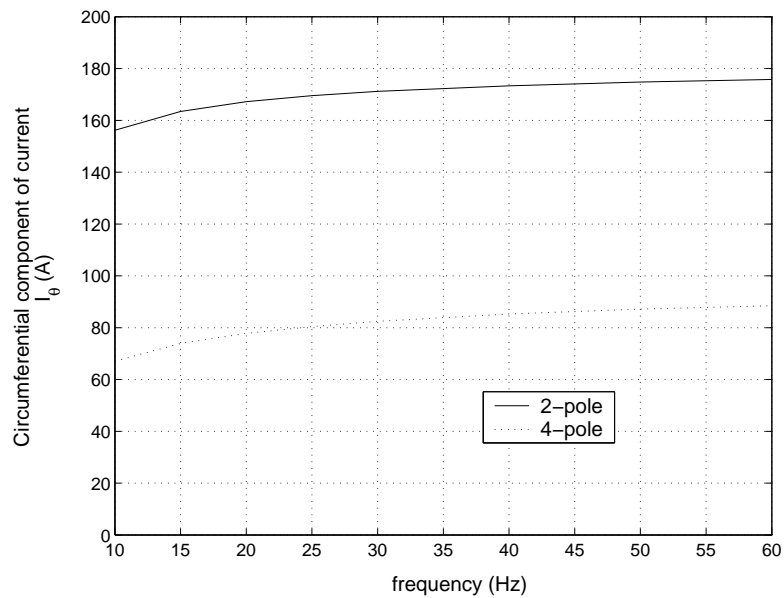


Figure 4.6: Circumferential current crossing the pole-centre plane in one direction.

4.4 Closed Form Expression for Power Loss

The relative significance of power loss due to cross lamination flux depends on several factors including the number of poles, material properties physical dimensions and operating frequency. A closed form expression for the power loss due to radial flux is now derived. This expression can be used by axial flux machine designers to make a quick assessment of the requirement to consider power loss due to curvature related cross lamination flux.

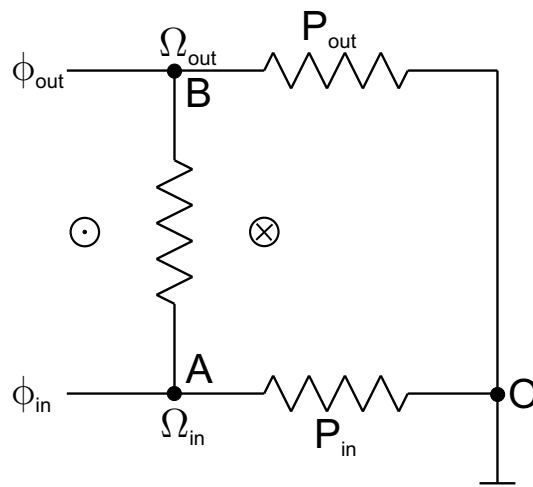


Figure 4.7: Simplified representation of an axial flux machine core.

As shown in Figure 4.7, the core is represented by a simplified equivalent coupled relative-resistive network. The relative circuit contains only three nodes. Nodes A and B are located on the pole centre plane at $(r_i + (r_o - r_i)/4, 0, \delta/2)$ and $(r_o - (r_o - r_i)/4, 0, \delta/2)$, respectively, where r_i and r_o are the core inner and outer radii, respectively and δ is the core axial length. The third node represents the plane of uniform magnetic potential which is equidistant from adjacent pole centre planes. The resistive circuit is a single loop linking the relative branch which represents permeance in the radial direction between nodes A and B.

The following assumptions are now made:

- a) Half of the flux per pole that enters the core from the air-gap between $r = r_i + (r_o - r_i)/2$ and $r = r_o$ flows through branch BO. This is represented by ϕ_{out} in Figure 4.7.
- b) Half of the flux per pole that enters the core from the air-gap between $r = r_i$ and $r = r_i + (r_o - r_i)/2$ flows through branch AO. This is represented by ϕ_{in} in Figure 4.7.
- c) The resistance of the resistive loop is sufficiently small such that the induced current cause the net flux flowing in the relative branch between nodes A and B to be practically zero.
- d) Reluctance in the axial direction is assumed to be zero.
- e) Branch BO represents flux paths between $r = r_i + (r_o - r_i)/2$ and $r = r_o$.
- f) Branch AO represents flux paths between $r = r_i$ and $r = r_i + (r_o - r_i)/2$.
- g) Due to the skin effect, the circumferential component of the loop current decays exponentially from the core flat surfaces with characteristic decay length equal to the skin depth.

Based on these assumptions and Figure 4.8 equations (4.22) through (4.27) are now derived. The flux exiting the core from the air-gap between $r = r_i + (r_o - r_i)/2$ and $r = r_o$ is given by

$$\begin{aligned}\phi_{out} &= \int_{\frac{(r_o+r_i)}{2}}^{r_o} \int_0^{\frac{\pi}{p}} \hat{B}_z \sin\left(\frac{p\theta}{2}\right) r \partial\theta \partial r \\ &= \frac{\hat{B}_z (3r_o + r_i)(r_o - r_i)}{4p},\end{aligned}\tag{4.22}$$

where \hat{B}_z is the peak air-gap magnetic flux density and p the number of machine poles.

The flux entering the core from the air-gap between $r = r_i$ and $r = r_i + (r_o - r_i)/2$ is

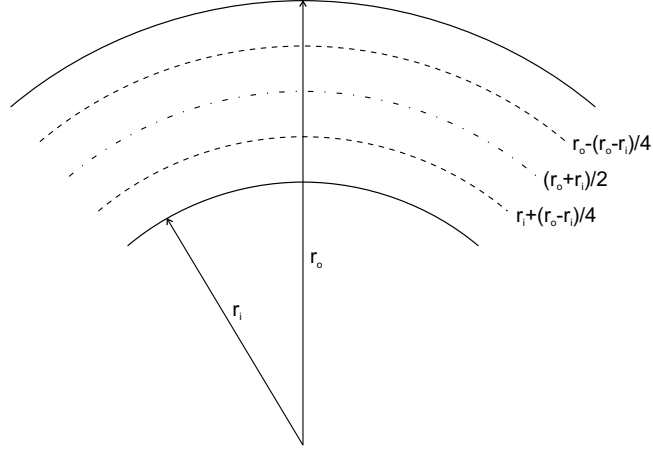


Figure 4.8: Core radial divisions used to derive a closed form loss equation.

given by

$$\begin{aligned}\phi_{in} &= \int_{r_i}^{\frac{(r_o+r_i)}{2}} \int_0^{\frac{\pi}{p}} \hat{B}_z \sin\left(\frac{p\theta}{2}\right) r \partial\theta \partial r \\ &= \frac{\hat{B}_z (3r_i + r_o) (r_o - r_i)}{4p}.\end{aligned}\quad (4.23)$$

The permeance of branch BO is given by

$$\begin{aligned}P_{out} &= \frac{\mu_\theta \delta \left(\frac{r_o - r_i}{2}\right)}{\pi \left(r_o - \frac{r_o - r_i}{4}\right)} \\ &= \frac{2p\mu_\theta \delta (r_o - r_i)}{\pi (3r_o + r_i)}.\end{aligned}\quad (4.24)$$

The permeance of branch AO is given by

$$\begin{aligned}P_{in} &= \frac{\mu_\theta \delta \left(\frac{r_o - r_i}{2}\right)}{\pi \left(r_i + \frac{r_o - r_i}{4}\right)} \\ &= \frac{2p\mu_\theta \delta (r_o - r_i)}{\pi (3r_i + r_o)}.\end{aligned}\quad (4.25)$$

The axial and circumferential components of the loop resistance are given by

$$\begin{aligned}R_z &= \frac{\delta}{\sigma_z \frac{(r_o - r_i) \pi \left(\frac{r_o + r_i}{2}\right)}{p}} \\ &= \frac{2p\delta}{\sigma_z \pi (r_o^2 - r_i^2)}\end{aligned}\quad (4.26)$$

and

$$\begin{aligned}
 R_\theta &= \frac{\pi \left(\frac{r_o + r_i}{2} \right)}{\sigma_\theta (r_o - r_i) S} \\
 &= \frac{\pi (r_o + r_i)}{2 \sigma_\theta p S (r_o - r_i)},
 \end{aligned} \tag{4.27}$$

respectively, where S is the skin depth defined by

$$S = \sqrt{\frac{2}{\omega \mu_r \sigma_\theta}}. \tag{4.28}$$

In accordance with assumption c), the loop current linking the permeance branch AB is given by

$$\begin{aligned}
 I &= \Omega_{out} - \Omega_{in} \\
 &= \frac{\phi_{out}}{P_{out}} - \frac{\phi_{in}}{P_{in}} \\
 &= \frac{\hat{B}_z \pi (r_o^2 - r_i^2)}{\mu_\theta \delta p^2}
 \end{aligned} \tag{4.29}$$

and thus the induced core loss F is found using

$$\begin{aligned}
 F &= pI^2 (R_z + 2R_\theta) \\
 &= \frac{\hat{B}_z^2 \pi^2 (r_o^2 - r_i^2)}{\mu_\theta^2 \delta^2 p^3} \left[\frac{2p\delta}{\pi \sigma_z} + \frac{\pi (r_o + r_i)^2}{Sp \sigma_\theta} \right].
 \end{aligned} \tag{4.30}$$

Loss predictions made using equation (4.30) and the axiperiodic coupled network formulations are given in Table 4.3.

Table 4.3: Comparison between power loss (F) predicted by equation (4.30) and that predicted by the axiperiodic coupled network method.

Loss prediction (W)	2-pole	4-pole	6-pole	8-pole
using equation(4.30)	2.66	0.672	0.308	0.171
using the axiperiodic coupled network method	1.62	0.482	0.236	0.144

Table 4.3 shows that equation (4.30) tends to over estimate power loss. This is to be expected given the fairly crude assumptions on which equation (4.30) is based on. For example, assumption c) results in an over estimation of the induced current while assumption g) means that the current will be forced to flow in a high resistance path. The nature of these assumptions are such that they lead to an overestimation of power loss. Although the predictions made by equation (4.30) may not be very accurate, predicted losses can still be used by machine designers to allow a quick decision to be made on whether or not there is a need for detailed investigation into power loss due cross-lamination flux.

4.4.1 Rotating Fields

The imposed magnetic flux boundary condition derived in Section 3.1.2 is for the case where the fields are stationary with respect to the core and pulsating at frequency ω . That is, the imposed magnetic flux density distribution $B(r, \theta, t)$ is given by $\hat{B}_z(r) \cos(\omega t) \cos(p\theta/2)$, where $\hat{B}(r)$ is the peak value of the magnetic flux density in time at the pole planes. In practice, a rotating air-gap magnetic field is more likely. It is now shown that, for any given $\hat{B}_z(r)$, the power loss for the rotating field case is twice that for the pulsating field case.

The power loss density D in the core is given by

$$D = [\vec{J} \cdot \vec{J}] \begin{bmatrix} \sigma_r & 0 & 0 \\ 0 & \sigma_\theta & 0 \\ 0 & 0 & \sigma_z \end{bmatrix}^{-1}, \quad (4.31)$$

where \vec{J} is the current density and σ_r , σ_θ and σ_z are the radial, circumferential and axial components of the core conductivity. For consistency with the coupled network formulation derived in Chapter 3, we express \vec{J} in terms of the electric vector potential \vec{T} using

$$\vec{J} = \nabla \times \vec{T}. \quad (4.32)$$

It was shown in Chapter 3 that, in order to predict the losses due only to the ra-

dial component of the magnetic flux density, the induced current density can be fully described by choosing an electric vector potential of the form

$$\vec{T} = T_r \hat{r} + 0\hat{\theta} + 0\hat{z}. \quad (4.33)$$

Substituting equation (4.33) into (4.32) gives

$$\vec{J} = 0\hat{r} + \frac{\partial T_r}{\partial z} \hat{\theta} - \frac{1}{r} \frac{\partial T_r}{\partial \theta} \hat{z}. \quad (4.34)$$

The core power loss density D given in equation (4.31) can thus be written in terms of \vec{T} as

$$D = \frac{1}{\sigma_\theta} \left(\frac{\partial T_r}{\partial z} \right)^2 + \frac{1}{\sigma_z r^2} \left(\frac{\partial T_r}{\partial \theta} \right)^2. \quad (4.35)$$

For the axiperiodic case presented in Section 3.4, the electric vector potential is of the form

$$T_r(r, \theta, z, t) = \hat{T}(r, z) \cos(\omega t + \varphi) \cos\left(\frac{p\theta}{2}\right), \quad (4.36)$$

where $\hat{T}(r, z)$ is the peak value of T_r in time on a pole-centre plane and φ is the phase angle between T_r and $B(r, \theta, z)$. Substituting equation (4.36) into (4.35) results in

$$D = \frac{1}{\sigma_\theta} \left(\frac{\partial \hat{T}}{\partial z} \right)^2 \cos^2(\omega t + \varphi) \cos^2\left(\frac{p\theta}{2}\right) + \frac{1}{\sigma_z r^2} \left(\frac{p}{2}\right)^2 \hat{T}^2 \cos^2(\omega t + \varphi) \sin^2\left(\frac{p\theta}{2}\right). \quad (4.37)$$

Based on equation (4.37), the instantaneous power loss $F(t)$ in the core is given by

$$\begin{aligned} F(t) &= \int_0^\delta \int_{r_i}^{r_o} \int_0^{2\pi} D r \partial\theta \partial r \partial z \\ &= \pi \cos^2(\omega t + \varphi) \int_0^\delta \int_{r_i}^{r_o} \left[\frac{1}{\sigma_\theta} \left(\frac{\partial \hat{T}}{\partial z} \right)^2 + \frac{1}{\sigma_z r^2} \left(\frac{p}{2}\right)^2 \hat{T}^2 \right] r \partial r \partial z, \end{aligned} \quad (4.38)$$

where δ is the core axial length and r_i and r_o are the core inner and outer radii, respectively. From equation (4.38), the power loss in the core F is given by

$$\begin{aligned} F &= \frac{1}{P} \int_0^P F(t) \partial t \\ &= \frac{\pi}{2} \int_0^\delta \int_{r_i}^{r_o} \left[\frac{1}{\sigma_\theta} \left(\frac{\partial \hat{T}}{\partial z} \right)^2 + \frac{1}{\sigma_z r^2} \left(\frac{p}{2}\right)^2 \hat{T}^2 \right] r \partial r \partial z, \end{aligned} \quad (4.39)$$

where $P = 1/f$ is the period of the field.

The T_r given in equation (4.36) and used to derive equation (4.39) is for the case where the field is stationary with respect to the core and pulsating at frequency ω . For a rotating field the electric vector potential will be of the form

$$T_r(r, \theta, z, t) = \hat{T}(r, z) \cos\left(\omega t + \varphi - \frac{p\theta}{2}\right), \quad (4.40)$$

where $\hat{T}(r, z)$ is the peak value of T_r in time. This was demonstrated using the principle of superposition in Section 2.1.2 for a three phase system. Substituting equation (4.40) into (4.35) results in

$$D_R = \frac{1}{\sigma_\theta} \left(\frac{\partial \hat{T}}{\partial z}\right)^2 \cos^2\left(\omega t + \varphi - \frac{p\theta}{2}\right) + \frac{1}{\sigma_z r^2} \left(\frac{p}{2}\right)^2 \hat{T}^2 \sin^2\left(\omega t + \varphi - \frac{p\theta}{2}\right), \quad (4.41)$$

where the subscript R denotes a rotating field. The instantaneous power loss $F_R(t)$ in the core due to the rotating field is given by

$$\begin{aligned} F_R(t) &= \int_0^\delta \int_{r_i}^{r_o} \int_0^{2\pi} D_R r \partial\theta \partial r \partial z \\ &= \pi \int_0^\delta \int_{r_i}^{r_o} \left[\frac{1}{\sigma_\theta} \left(\frac{\partial \hat{T}}{\partial z}\right)^2 + \frac{1}{\sigma_z r^2} \left(\frac{p}{2}\right)^2 \hat{T}^2 \right] r \partial r \partial z. \end{aligned} \quad (4.42)$$

From equation (4.42), the power loss in the core F_R is given by

$$\begin{aligned} F_R &= \frac{1}{P} \int_0^P F_R(t) \partial t \\ &= \pi \int_0^\delta \int_{r_i}^{r_o} \left[\frac{1}{\sigma_\theta} \left(\frac{\partial \hat{T}}{\partial z}\right)^2 + \frac{1}{\sigma_z r^2} \left(\frac{p}{2}\right)^2 \hat{T}^2 \right] r \partial r \partial z. \end{aligned} \quad (4.43)$$

Comparing equations (4.39) and (4.43) it can be seen that the core loss due to a rotating field is twice that due to the pulsating field. Thus the coupled network formulation of Chapter 3 can be used with the imposed magnetic flux boundary given in Section 3.1.2 and the power loss for a rotating field of the same peak amplitude will be twice that of the pulsating field case.

4.5 Laboratory Tests

The theory and loss predictions presented in Sections 4.3 and 4.4 point to the likelihood of increased core loss due to the curvature of the core in axial flux machines. Curvature related loss cannot be separately measured as it is part of the total input power to the machine. Its extraction from total measured core loss could, however, be based on its relationship with frequency. Total core loss, P_T , can be expressed as

$$P_T = F + k_1 f + k_2 f^{3/2} + k_3 f^2, \quad (4.44)$$

where F represents loss due to cross-lamination flux, $k_1 f$ represents hysteresis loss, $k_2 f^{3/2}$ represents excess loss (Barbisio et al., 2004; Fiorillo & Novikov, 1990) and $k_3 f^2$ represents classical eddy-current loss due to main or parallel running flux.

As shown in Figure 4.9, if there is a significant amount of eddy current loss due to cross-lamination flux, then the axiperiodic model predicts a non-linear relationship between P_T/f and f , irrespective of the value of k_2 . The non-linearity is characterised by a minimum turning point occurring at frequency f_m . The more significant the loss due to cross-lamination flux, compared to classical eddy current and excess loss, the higher the value of f_m and the easier it would be to locate using test data. The practical identification of the turning point at f_m requires tests to be performed over a frequency range extending sufficiently below f_m . Indication of the existence of a turning point by test data would signify the presence of a significant amount of power loss due to cross-lamination flux. Conversely, it can be shown that if F is equal to zero, no turning point exists in the P_T/f against f graph.

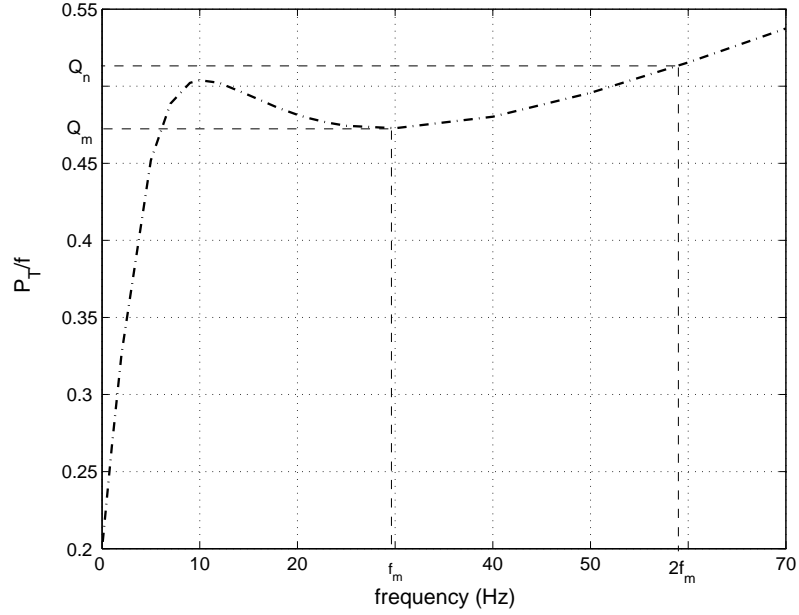


Figure 4.9: Determination of k from hypothetical experimental data.

Equation (4.45), which is obtained by substituting equation (4.21) into (4.44), is now used to show how loss due to cross lamination flux can be separated from the other core loss components.

$$\frac{P_T}{f} = \frac{k}{\sqrt{f}} + k_1 + k_2\sqrt{f} + k_3f \quad (4.45)$$

The turning point located at $f = f_m$ in Figure 4.9 is found by differentiating equation (4.45) with respect to f and equating to zero, that is

$$-\frac{k}{2}f_m^{-3/2} + \frac{k_2}{2\sqrt{f_m}} + k_3 = 0. \quad (4.46)$$

Equation (4.46) is then be rearranged to give

$$k = k_2f_m + 2k_3f_m^{3/2}. \quad (4.47)$$

Using equation (4.45) at points Q_m and Q_n in conjunction with equation (4.47), it can be shown that

$$k = \frac{2\sqrt{f_m}(Q_n - Q_m) + k_2f_m(3 - 2\sqrt{2})}{(\sqrt{2} - 1)} \quad (4.48)$$

where Q_m and Q_n are defined in Figure 4.9. Equation (4.48) allows k to be estimated from experimental data. If accurate estimation of k_2 is not possible, and it is assumed

to be equal to zero (resulting in k_3 assuming its maximum possible value), equation (4.48) returns the lower bound for k . Equation (4.49), which is based the assumption of k_3 being equal to zero (which results in k_2 assuming its maximum possible value), gives the upper bound for k :

$$k = \frac{\sqrt{2f_m}(Q_n - Q_m)}{(3 - 2\sqrt{2})} \quad (4.49)$$

By comparing equations (4.48) and (4.49), it can be deduced that the maximum error from assuming a zero value for k_2 in equation (4.48) is 41%. However, such a high error is unlikely in practice as classical eddy-current loss will always be relatively significant compared to excess loss.

Figure 4.10 shows experimental data for test cores with physical dimensions $r_i = 0.075\text{m}$, $r_o = 0.175\text{m}$ and $\delta = 0.1\text{m}$. The test set-up is shown in Figure 4.11. Core loss, for both cores, was obtained by subtracting copper loss from the total measured power.

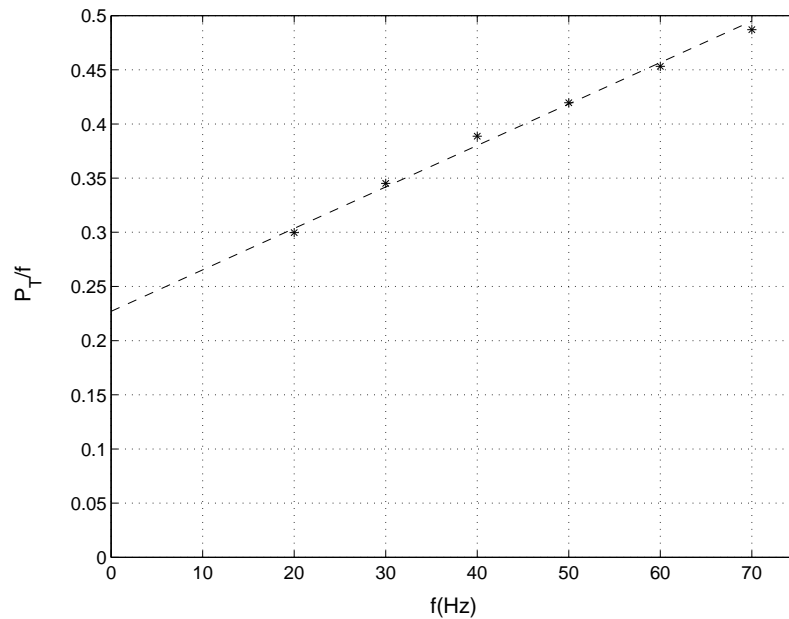


Figure 4.10: Experimental results ($\hat{B}_z = 0.5\text{T}$).

Experimental results suggest that core loss due to cross-lamination flux is not significant. That is, there is no indication of the existence of a turning point for varying

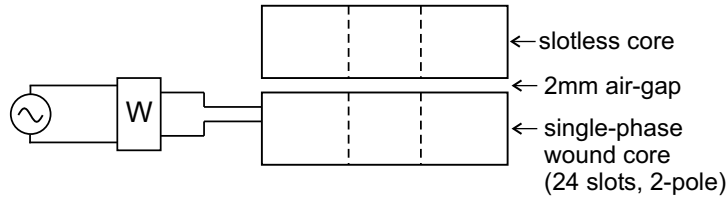


Figure 4.11: Experimental set-up for measuring core losses.

test frequencies. From measurements made with one of the cores wound as a toroidal transformer, the core permeability was estimated to be greater than $5000\mu_o$. From manufacturer's data σ_θ was estimated to be about $4.5 \times 10^6 \text{ S/m}$. Based on these values the axiperiodic model predicts the losses due to cross-lamination flux to be 0.311W at 50Hz. This is relatively small compared to the total measured core loss of approximately 21W of which 10W is estimated to be hysteresis loss. It is not surprising, therefore, that the experimental data points in Figure 4.10 do not indicate the existence of a significant amount of power loss due to cross-lamination flux.

4.6 Flux Density Distribution

It was predicted in Chapter 2 that curvature related radial flux density is relatively small compared to the peak axial and circumferential flux densities even when the shielding effect of induced eddy currents is ignored. The model used to make this prediction was a magnetostatic one and thus could not be used to investigate the frequency dependence of the radial component.

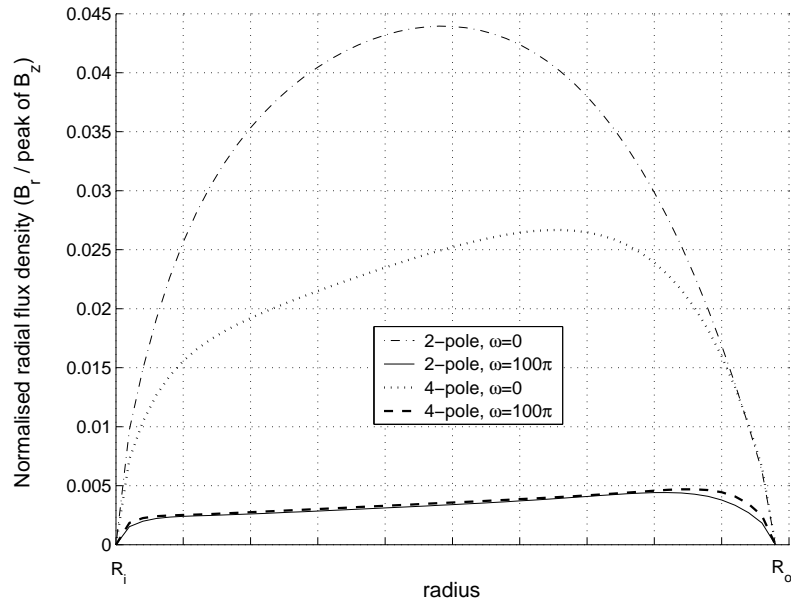
The axiperiodic coupled network model developed in Section 3.4 has been used to analyse the flux density distribution in a core with the following nominal characteristics: $r_i = 0.075 \text{ m}$, $r_o = 0.175 \text{ m}$, $\delta = (0.2/p) \text{ m}$, $\mu_r = 20\mu_o$, $\mu_\theta = \mu_z = 1000\mu_o$, $\sigma_r = 0 \text{ S/m}$, $\sigma_\theta = \sigma_z = 5 \times 10^6 \text{ S/m}$, $\omega = 100\pi \text{ rad/s}$ and $\hat{B}_z = 0.7 \text{ T}$.

Figure 4.12 shows theoretical predictions for the normalised radial flux density as a

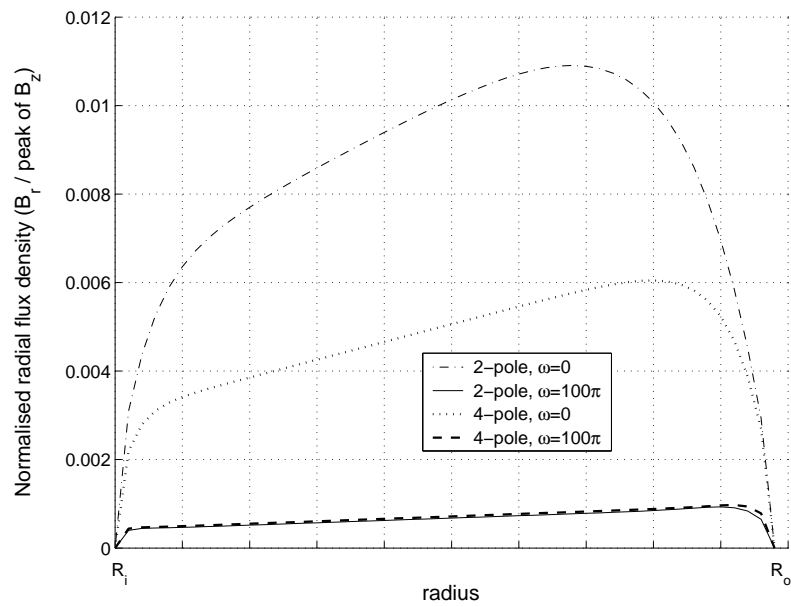
function of radius, and averaged over the core axial length. Similarly, Figure 4.13 shows the normalised circumferential flux density as a function of radius, averaged over the core axial length.

Based on these results the following observations can be made:

- a) The peak radial flux density is much smaller than the peak axial or circumferential flux densities.
- b) The radial component of the magnetic flux density is almost non-existent under a.c. conditions. This is theoretical confirmation of what was already postulated in Chapter 2 based on magnetostatic analysis and experimental results.
- c) The amount of radial flux, although small, is a strong function of core permeability.
- d) The circumferential flux density is greatest near the outer radius of the core. As stated Chapter 2, this must be accounted for when sizing the back-iron of axial flux machines.

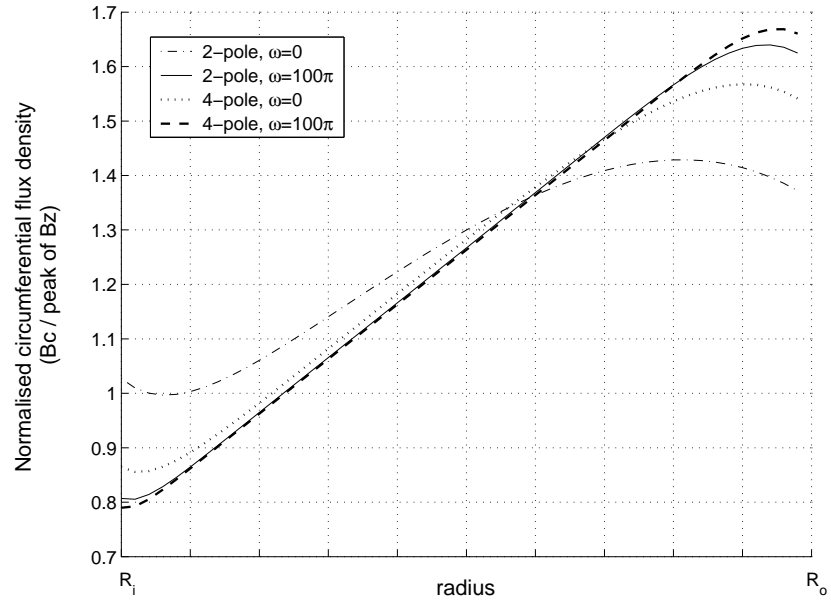


(a) $\mu_\theta = \mu_z = 1000\mu_o$

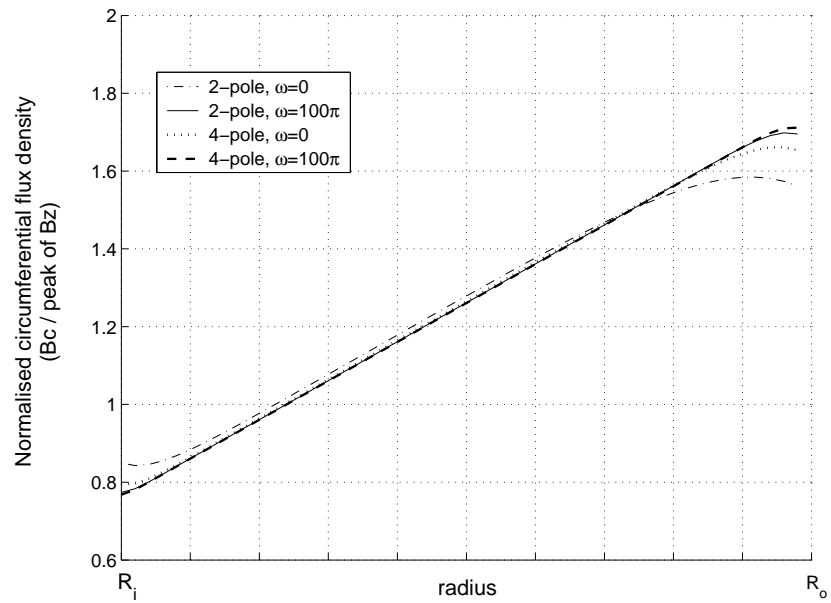


(b) $\mu_\theta = \mu_z = 5000\mu_o$

Figure 4.12: Normalised average radial flux density along a pole-centre plane.



(a) $\mu_\theta = \mu_z = 1000\mu_o$



(b) $\mu_\theta = \mu_z = 5000\mu_o$

Figure 4.13: Normalised average circumferential flux density half way between pole-centre planes.

4.7 Practical Axial Flux Machines

It has been the aim of this research to predict the magnetic flux density distribution and power loss due to curvature related radial flux in the back-iron of axial flux machines. Whilst these aims have been achieved, the assumptions upon which the models have been based does limit their practicality. In practice, core losses and the magnetic flux density distribution will be affected by material non-linearities, end effects, air-gap length, magnet shape in the case of permanent magnet machines and the presence of slots. Further to the work carried out here, the influence of these factors should be investigated.

In order to relax some of our assumptions it would be necessary to include the air-gap region in the core model. This in itself may present additional difficulties when using techniques such as the Finite Element Method (FEM). Whilst FEM is now a well accepted tool for the design and analysis of practically all types of electrical machines (Binns et al., 1992; Salon, 1995) it does struggle with the small air gap length of electrical machines (Salon, 1995). This is fundamentally due to the increase in the number of nodes or elements required to mesh sub-domains of poor aspect ratio. This situation is common when modeling electrical machines which incorporate narrow air gap regions relative to other dimensions.

A scaling technique is developed in Chapter 5 which provide one way of reducing the number of nodes required when performing finite element analysis of electrical machines with narrow air-gap regions. Whilst this technique does not directly contribute to the work presented here, it does provide a tool which could be used to extend the work beyond its current limitations.

Chapter 5

Sub-domain Scaling for Finite Element Analysis of Electrical Machines

We will now develop a scaling technique which can be used when performing electromagnetic finite element analysis. This technique has the ability to overcome problems associated with meshing domains of poor aspect ratio. Such a situation occurs commonly when modeling electrical machines which incorporate narrow air-gap regions with respect to dimensionally much greater steel cores. Here we will develop the scaling technique with a focus on scaling in the axial direction for the finite element analysis of axial flux machines.

Although not of direct application to the work presented previously, it will be shown that the scaling technique is a general tool for the finite element analysis of electrical machines. As such it has the ability to permit further analysis which would allow some of the assumptions made in this project to be relaxed. For this reason and because of its general usefulness, sub-domain scaling for finite element analysis of electrical machine is now presented.

5.1 Finite Element Analysis and Scaling

Finite element analysis is now a well accepted tool for the design and analysis of practically all types of electrical machines (Binns et al., 1992; Salon, 1995). Finite element magnetostatic analysis allows machine designers to investigate phenomena such as saturation and magnetic torque, while quasi-static analysis can be used to predict eddy current losses and associated heating.

The small air gap length of an electrical machine compared to its other dimensions can, however, make it difficult or even impossible to obtain accurate field solutions (Salon, 1995). Techniques based on the use of shell elements (Guerin et al., 1994), specialist air-gap elements (Abdel-Razek et al., 1982; Feliachi et al., 1983) or the coupling of finite element analysis with an analytical solution (DeBortoli et al., 1991), have been proposed to overcome this problem. There have also been other techniques (Choi et al., 2001; Henrotte et al., 1999; Melissen & Simkin, 1990; Ouazzani et al., 1999), not specifically related to electrical machines, on geometry transformations and for overcoming meshing difficulties in the finite element method. All of these techniques require some form of modification to the finite element formulation. The method proposed here is based on a rescaling of the air gap region. The original problem, with the narrow air gap, is mapped onto a scaled problem with an improved aspect ratio.

Compared to previous techniques, a major advantage of the proposed method is that, when applied to axial flux machines, it can be simply implemented using any standard finite element package. In addition, techniques such as shell elements do not permit the user to investigate the fields in the air gap region whereas the scaling method provides the user with field solutions in all sub-domains.

5.1.1 The Finite Element Mesh

The Finite Element Method (FEM) is based on the discretization of the domain under consideration. The mesh quality or element aspect ratio can have a significant effect on

the solution accuracy (Adams & Askenazi, 1999; Chari & Salon, 2000). When meshing geometries of poor aspect ratio, or where adjacent sub-domains of large scale differences exist, the mesh quality can deteriorate if the number of elements is insufficient. Maintaining good element quality often requires vast numbers of elements and their associated nodes. This can be most easily seen in a two dimensional example. Consider the domain represented in Figure 5.1 where a large sub-domain is adjacent a much smaller one and triangular elements have been chosen.

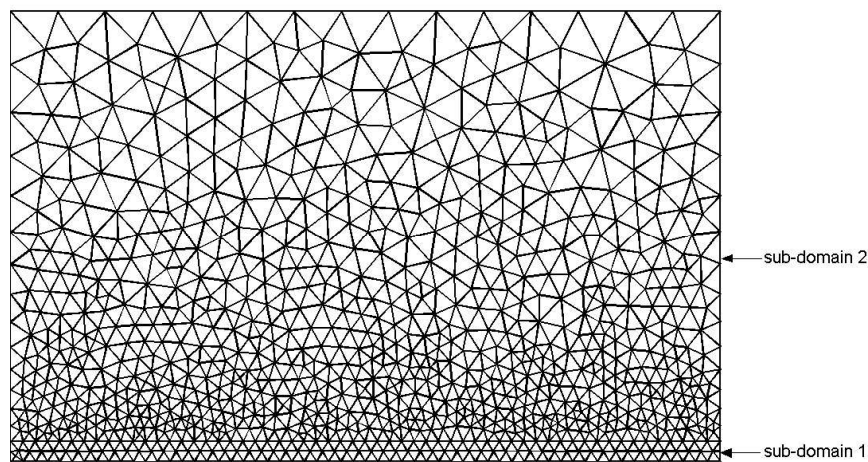


Figure 5.1: Finite element 2D mesh .

The nodes at the boundary between the two sub-domains are common to the elements on either side and thus the element sizes are comparable near the boundary. Due to the thinness of Sub-domain 1 the maximum characteristic size (d) of an element in this region is equal to the region's height. Ideally, the element shape is an equilateral triangle. This restriction alone requires a significant number of elements to mesh a region which is thin in one direction and significantly larger in the other (i.e. poor aspect ratio). At the boundary, the elements in Sub-domain 2 have edges of the same lengths as those in Sub-domain 1 because of their common nodes. Away from the boundary the elements can grow in size, however, this requires a gradual transition in order to maintain an acceptable element aspect ratio. In these circumstances the number of elements required to mesh the domain rapidly increases as d decreases. Depending on desired accuracy of the solution in Sub-domain 1, the maximum element size may not be desirable which

will further exaggerate the problem. This problem is considerably worse when performing three-dimensional meshing on geometries containing sub-domains with poor aspect ratios. Such a situation occurs when modeling electrical machines which incorporate a small air gap region compared to other dimensions. The number of nodes determines the computing resources required to solve a finite element problem and thus it is highly desirable to reduce this number whilst retaining the desired solution accuracy.

Sub-domain rescaling provides one way of overcoming this problem. The rescaling technique can be regarded as a transformation of the problem domain into another domain in which meshing can more readily be achieved. The transformation generally involves changes in dimensions, material properties and source current densities. Such a transformation is useful where the flux density in the transformed sub-domain, $B'(r', \theta', z')$, can be calculated and thus the flux density in the original sub-domain, $B(r, \theta, z)$, found.

The reduction in the number of nodes due to the scaling process will be problem dependent. At one extreme, scaling a problem which has an already large air gap region may not produce any benefit. On the other hand there will be instances where, due to very poor aspect ratios in the geometry, an acceptable finite element solution may not be possible without the use of some form of scaling. An excessively small air gap may even cause generic meshing algorithms to fail or produce a poor quality mesh.

It may seem, particularly in cases where there are regions in which the field variables change rapidly in space, that the coarser mesh produced by the scaling process will result in increased solution errors. However, if adaptive meshing methods are used this will not be the case. Even where adaptive meshing is not available manually controlled mesh refinement can be used to improve solution accuracy (Hewitt & Ahfock, 2005).

5.1.2 Quasi-Static Formulation

There are a number of different quasi-static finite element formulations, two of the more common being the magnetic vector potential-electric scalar potential ($A - \phi$) and

electric vector potential-magnetic scalar potential ($T - \Omega$) formulations (Ratnajeevan & Hoole, 1995). Regardless of the formulation type all are based on the quasi-static approximation to Maxwell's equations:

$$\nabla \cdot \vec{B} = 0 \tag{5.1}$$

$$\nabla \times \vec{H} = \vec{J} \tag{5.2}$$

$$\nabla \times \vec{E} = -\frac{\partial \vec{B}}{\partial t} \tag{5.3}$$

where \vec{B} is the magnetic flux density, \vec{H} the magnetic field intensity, \vec{J} the current density, \vec{E} the electric field intensity and t is time.

The scaling technique developed here is based on these equations and not a finite element formulation. This has the advantage of not requiring specialist finite element formulations or element types.

5.2 Scaling Equations

Scaling in the axial direction is desirable when modeling axial flux machines in which the air gap length is defined in the axial (or z) direction. Scaling in the radial direction is equally attractive when modeling radial flux machines. Transformations for radial scaling have been presented in Hewitt & Ahfok (2005).

The focus here is on the development of an axial scaling technique for the finite element analysis of axial flux machines with narrow air gap regions. Whether modeling the entire machine or some part of it which includes the air-gap, scaling has the potential to reduce the number of elements required to mesh the domain. This also means a reduction in the total computational cost of solving the problem.

5.2.1 Axial Scaling

Consider an axial flux machine (AFM) with its domain divided into the three sub-domains

- a) Sub-domain 1 : $-z_l < z < 0$
- b) Sub-domain 2 : $0 < z < z_a$
- c) Sub-domain 3 : $z_a < z < z_u$

as shown in Figure 5.2.

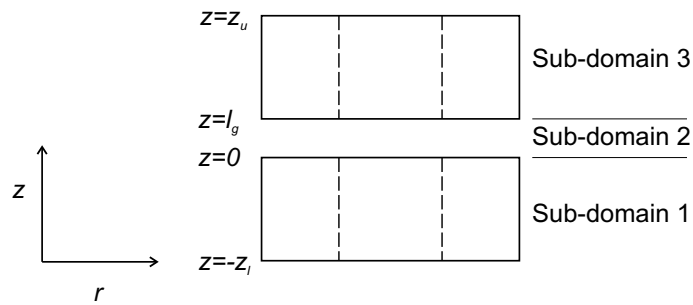


Figure 5.2: Axial scaling sub-domains.

It is proposed that Sub-domain 2 be scaled by a scale factor k_s in the axial direction so that it then occupies the extended region $0 < z < k_s l_g$. Sub-domains 1 and 3 have none of their dimensions scaled and thus their respective field variables are unchanged. Sub-domain 3 does however undergo a translation of its axial position as defined by

$$z^T = z + l_g (k_s - 1) \tag{5.4}$$

in order to permit the expansion of Sub-domain 2. As Sub-domains 1 and 3 are not scaled, the boundary conditions between them and the scaled region remain invariant.

The transformation that maps the physical dimensions of the original problem onto the dimensions of the transformed problem are fully defined by k_s . Based on this

transformation, the relationships between the field variables in the original problem and the corresponding field variables in the transformed problem can be found. In general these take the form of

$$G^T(r^T, \theta^T, z^T) = y(k_s) G(r, \theta, z)$$

where G^T represents a transformed quantity in the transformed domain, G is the corresponding quantity in the original domain and $y(k_s)$ defines the relationship between them. The functions represented by $y(k_s)$ are derived by ensuring that if G^T satisfied Maxwell's equations in the transformed domain, then G satisfied Maxwell's equations in the original domain. In other words, $y(k_s)$ permits the field solutions obtained in the transformed problem to be converted into the corresponding field solutions to the original problem. Having derived the $y(k_s)$ functions for all the field variables, the relationships between the material properties of the original problem and those of the transformed one can be deduced.

5.2.2 Axial Scaling Transformations

In the scaled sub-domain, let the coordinate system be transformed according to

$$\begin{aligned} r^T &= r, \\ \theta^T &= \theta, \\ z^T &= k_s z. \end{aligned} \tag{5.5}$$

Let the magnetic flux density \vec{B} and the magnetic field intensity \vec{H} in this region be transformed by

$$B_r^T = f_r B_r, \tag{5.6}$$

$$B_\theta^T = f_\theta B_\theta, \tag{5.7}$$

$$B_z^T = f_z B_z, \tag{5.8}$$

$$H_r^T = g_r H_r, \tag{5.9}$$

$$H_\theta^T = g_\theta H_\theta, \tag{5.10}$$

$$H_z^T = g_z H_z, \tag{5.11}$$

where all scale factors are functions of z only. Expanding $\nabla \cdot \vec{B} = 0$ in cylindrical coordinates results in

$$\frac{1}{r} \frac{\partial (rB_r)}{\partial r} + \frac{1}{r} \frac{\partial B_\theta}{\partial \theta} + \frac{\partial B_z}{\partial z} = 0. \quad (5.12)$$

In the scaled region equation (5.12) becomes

$$\frac{1}{r} \frac{\partial (rf_r B_r)}{\partial r} + \frac{1}{r} \frac{\partial f_\theta B_\theta}{\partial \theta} + \frac{1}{k_s} \frac{\partial f_z B_z}{\partial z} = 0. \quad (5.13)$$

For both equations (5.12) and (5.13) to hold for all (r, θ, z) it is required that

$$B_z \frac{\partial f_z}{\partial z} = 0 \quad (5.14)$$

and

$$f_r = f_\theta = \frac{f_z}{k_s}. \quad (5.15)$$

Equation (5.14) requires that $f_z = k$, where k is independent of z , and thus

$$\begin{aligned} f_r &= \frac{k}{k_s}, \\ f_\theta &= \frac{k}{k_s}, \\ f_z &= k. \end{aligned} \quad (5.16)$$

The unknown constant k in (5.16) is found by considering the boundary condition between Sub-domains 1 and 2. In order to satisfy the continuity of the normal component of \vec{B} across the boundary it is required that $f_z = k = 1$. Substituting $k = 1$ in equation (5.16) and in accordance with equations (5.6), (5.7) and (5.8) the resulting transformations for the magnetic flux density components are

$$\begin{aligned} B_r^T &= \frac{B_r}{k_s}, \\ B_\theta^T &= \frac{B_\theta}{k_s}, \\ B_z^T &= B_z. \end{aligned} \quad (5.17)$$

It should be noted that $f_z = 1$ also satisfies the continuity of the normal component of \vec{B} across the boundary between Sub-domains 2 and 3.

The quasi-static approximation of equation (5.2) guarantees the solenoidal condition $\nabla \cdot \vec{J} = 0$. As both \vec{B} and \vec{J} are defined through the same divergence condition, \vec{J}

will have the same transformation functions as that of \vec{B} , that is:

$$\begin{aligned} J_r^T &= \frac{J_r}{k_s}, \\ J_\theta^T &= \frac{J_\theta}{k_s}, \\ J_z^T &= J_z. \end{aligned} \quad (5.18)$$

The transformation functions for the magnetic field intensity \vec{H} can be found by expanding equation (5.2) in a cylindrical coordinate system to obtain

$$\vec{J} = \hat{r} \left[\frac{1}{r} \frac{\partial H_z}{\partial \theta} - \frac{\partial H_\theta}{\partial z} \right] + \hat{\theta} \left[\frac{\partial H_r}{\partial z} - \frac{\partial H_z}{\partial r} \right] + \hat{z} \left[\frac{1}{r} \frac{\partial (r H_\theta)}{\partial r} - \frac{1}{r} \frac{\partial H_r}{\partial \theta} \right] \quad (5.19)$$

In the transformed region the radial component of the current density J_r^T can be expressed in terms of the magnetic field intensity H^T by substituting equations (5.10) and (5.11) into (5.19) to give

$$\begin{aligned} J_r^T &= \frac{1}{r} \frac{\partial H_z^T}{\partial \theta} - \frac{\partial H_\theta^T}{\partial z^T} \\ &= \frac{1}{r} \frac{\partial (g_z H_z)}{\partial \theta} - \frac{\partial (g_\theta H_\theta)}{k_s \partial z} \\ &= \frac{g_z}{r} \frac{\partial H_z}{\partial \theta} - \frac{1}{k_s} \frac{\partial (g_\theta H_\theta)}{\partial z}. \end{aligned} \quad (5.20)$$

At $z = 0$ the boundary condition $H_{t1} = H_{t2}$ where the subscripts t_1 and t_2 represent the tangential components of the magnetic field intensity \vec{H} in Sub-domains 2 and 3, respectively, must be fulfilled. Sub-domain 3 is unscaled and thus \vec{H} is unchanged in this region. At the boundary this requires $H_{r2} = H_{r3}$ and $H_{\theta2} = H_{\theta3}$. This will also be the case at the $z = k_s l_g$ boundary (i.e. between Sub-domains 1 and 2). These boundary conditions are satisfied by setting $g_r = g_\theta = 1$ in equations (5.9) and (5.10), respectively. Substituting $J_r^T = J_r/k_s$ and $g_\theta = 1$ in equation (5.20) results in

$$\begin{aligned} \frac{J_r}{k_s} &= \frac{g_z}{r} \frac{\partial H_z}{\partial \theta} - \frac{1}{k_s} \frac{\partial H_\theta}{\partial z} \\ \Rightarrow J_r &= k_s g_z \frac{1}{r} \frac{\partial H_z}{\partial \theta} - \frac{\partial H_\theta}{\partial z}. \end{aligned} \quad (5.21)$$

Comparing equations (5.21) and (5.19) it can be seen that $k_s g_z = 1$ and thus $g_z = 1/k_s$.

The transformations for the magnetic field intensity \vec{H} are thus

$$\begin{aligned} H_r^T &= H_r, \\ H_\theta^T &= H_\theta, \\ H_z^T &= \frac{H_z}{k_s}. \end{aligned} \tag{5.22}$$

The transformations for \vec{H} given in (5.22) are now tested in the circumferential and axial terms of equation (5.19). From equation (5.19) the circumferential component of the current density J_θ^T in terms of \vec{H}^T is given by

$$\begin{aligned} J_\theta^T &= \frac{\partial H_r^T}{\partial z^T} - \frac{\partial H_z^T}{\partial r} \\ &= \frac{1}{k_s} \frac{\partial (g_r H_r)}{\partial z} - g_z \frac{\partial H_z}{\partial r}. \end{aligned} \tag{5.23}$$

Substituting $J_\theta^T = J_\theta/k_s$, $g_r = 1$ and $g_z = 1/k_s$ into (5.23) results in

$$\begin{aligned} \frac{J_\theta}{k_s} &= \frac{1}{k_s} \frac{\partial H_r}{\partial z} - \frac{1}{k_s} \frac{\partial H_z}{\partial r} \\ \Rightarrow J_\theta &= \frac{\partial H_r}{\partial z} - \frac{\partial H_z}{\partial r}, \end{aligned} \tag{5.24}$$

which is in agreement with equation (5.19). Similarly, the axial component of the current density J_z^T is given by

$$\begin{aligned} J_z^T &= \frac{1}{r} \frac{\partial (r H_\theta^T)}{\partial r} - \frac{1}{r} \frac{\partial H_r^T}{\partial \theta} \\ &= \frac{g_\theta}{r} \frac{\partial (r H_\theta)}{\partial r} - \frac{g_r}{r} \frac{\partial H_r}{\partial \theta}. \end{aligned} \tag{5.25}$$

Substituting equation $J_z^T = J_z$ and $g_\theta = g_r = 1$ into equation (5.25) results in

$$J_z = \frac{1}{r} \frac{\partial (r H_\theta)}{\partial r} - \frac{1}{r} \frac{\partial H_r}{\partial \theta}, \tag{5.26}$$

which is also in agreement with equation (5.19).

The transformation function for the coordinate components of the electric field intensity \vec{E} can be found in the same way as that for the magnetic field intensity \vec{H} . In fact, as both \vec{E} and \vec{H} share common boundary conditions and can be defined through their

curl operators (i.e. equations (5.3) and (5.2), respectively) where \vec{J} and \vec{B} share the same transformation functions, their transformations are also the same, that is:

$$\begin{aligned} E_r^T &= E_r, \\ E_\theta^T &= E_\theta, \\ E_z^T &= \frac{E_z}{k_s}. \end{aligned} \tag{5.27}$$

The transformations for the magnetic permeability and electric conductivity are now found using the constitutive relations

$$\vec{B} = \mu \vec{H} \tag{5.28}$$

$$\vec{J} = \sigma \vec{E}. \tag{5.29}$$

Using equations (5.22), (5.17) and (5.28) the permeability transformations are

$$\begin{aligned} \mu_r^T &= \frac{B_r^T}{H_r^T} = \frac{1}{k_s} \frac{B_r}{H_r} = \frac{\mu_r}{k_s}, \\ \mu_\theta^T &= \frac{B_\theta^T}{H_\theta^T} = \frac{1}{k_s} \frac{B_\theta}{H_\theta} = \frac{\mu_\theta}{k_s}, \\ \mu_z^T &= \frac{B_z^T}{H_z^T} = k_s \frac{B_z}{H_z} = k_s \mu_z. \end{aligned} \tag{5.30}$$

Similarly from equations (5.18), (5.27) and (5.29) the conductivity transformations are given by

$$\begin{aligned} \sigma_r^T &= \frac{J_r^T}{E_r^T} = \frac{1}{k_s} \frac{J_r}{E_r} = \frac{\sigma_r}{k_s}, \\ \sigma_\theta^T &= \frac{J_\theta^T}{E_\theta^T} = \frac{1}{k_s} \frac{J_\theta}{E_\theta} = \frac{\sigma_\theta}{k_s}, \\ \sigma_z^T &= \frac{J_z^T}{E_z^T} = k_s \frac{J_z}{E_z} = k_s \sigma_z. \end{aligned} \tag{5.31}$$

A complete list of all field variable and material property transformations for the scaled Sub-domain are presented in Tables 5.1 and 5.2.

Table 5.1: Axial Scaling Transformations

Quantity/Property	Symbol	Sub-domain 2
Radial component of the current density	J_r	$J_r^T = \frac{J_r}{k_s}$
Angular component of the current density	J_θ	$J_\theta^T = \frac{J_\theta}{k_s}$
Axial component of the current density	J_z	$J_z^T = J_z$
Radial component of the magnetic field intensity	H_r	$H_r^T = H_r$
Angular component of the magnetic field intensity	H_θ	$H_\theta^T = H_\theta$
Axial component of the magnetic field intensity	H_z	$H_z^T = \frac{H_z}{k_s}$
Radial component of the magnetic flux density	B_r	$B_r^T = \frac{B_r}{k_s}$
Angular component of the magnetic flux density	B_θ	$B_\theta^T = \frac{B_\theta}{k_s}$
Axial component of the magnetic flux density	B_z	$B_z^T = B_z$

Table 5.2: Axial Scaling Transformations continued

Quantity/Property	Symbol	Sub-domain 2
Radial component of the electric field intensity	E_r	$E_r^T = E_r$
Angular component of the electric field intensity	E_θ	$E_\theta^T = E_\theta$
Axial component of the electric field intensity	E_z	$E_z^T = \frac{E_z}{k_s}$
Radial component of the permeability	μ_r	$\mu_r^T = \frac{\mu_r}{k_s}$
Angular component of the permeability	μ_θ	$\mu_\theta^T = \frac{\mu_\theta}{k_s}$
Axial component of the permeability	μ_z	$\mu_z^T = k_s \mu_z$
Radial component of the conductivity	σ_r	$\sigma_r^T = \frac{\sigma_r}{k_s}$
Angular component of the conductivity	σ_θ	$\sigma_\theta^T = \frac{\sigma_\theta}{k_s}$
Axial component of the conductivity	σ_z	$\sigma_z^T = k_s \sigma_z$

5.2.3 Energy and Power Invariance

The magnetic energy stored per unit volume (W) in an unscaled region is given by

$$W = \frac{1}{2} \vec{B} \cdot \vec{H} \quad (5.32)$$

and in the corresponding scaled region it becomes

$$\begin{aligned} W^T &= \frac{1}{2} \vec{B}^T \cdot \vec{H}^T \\ &= \frac{1}{2} (f_r g_r B_r H_r + f_\theta g_\theta B_\theta H_\theta + f_z g_z B_z H_z). \end{aligned} \quad (5.33)$$

Inspection of Table 5.1 shows that in the scaled region the equality

$$f_r g_r = f_\theta g_\theta = f_z g_z \quad (5.34)$$

always holds. This means that

$$W^T = fg W = \frac{W}{k_s}, \quad (5.35)$$

where $fg = f_r g_r = f_\theta g_\theta = f_z g_z = 1/k_s$. An elementary volume in the scaled region is related to the same volume in the unscaled region by

$$dV^T = \frac{dV}{fg} = k_s dV. \quad (5.36)$$

Equations (5.35) and (5.36) show that a volume integration of the transformed magnetic energy over the scaled region will result in the same stored magnetic energy as that of the unscaled region. This result also holds for Ohmic power dissipation ($\vec{E} \cdot \vec{J}$).

The invariance in the magnetic energy and power dissipation greatly simplifies post processing as there is no need to transform these quantities. It also implies that torque and inductance are also invariant under the transformation.

5.2.4 Material Non-Linearity

When using the axial scaling technique to scale the air gap region of axial flux machines, the air is normally the only material type occupying the region. Even where components

such as end-shields are included, it is reasonable to assume that these parts remain magnetically unsaturated. Material properties for the air gap region are easily deduced from Table 5.2, since μ and σ in this region are independent of the field quantities. Saturation in the stator or rotor iron region is modeled as if scaling was not performed as these regions are not affected by the transformation.

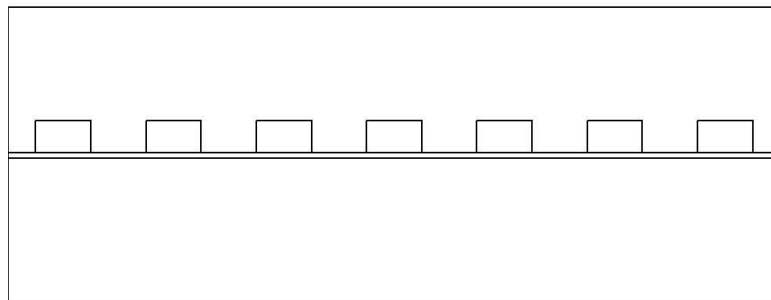
Whilst the assumption of linear behaviour in the scaled region does simplify the application of the scaling technique, it is not restricted to linear analysis. An example of scaling for non-linear finite element analysis of electrical machines can be found in Hewitt & Ahfock (2005).

5.3 Node and Element Reduction using the Axial Scaling Technique

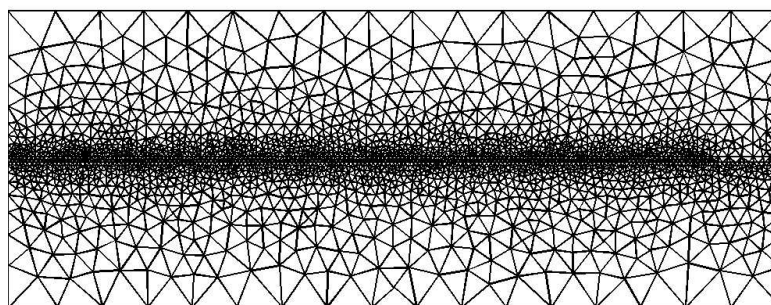
For AFMs with air gaps of poor aspect ratio or with large iron regions adjacent to narrow air gaps, the scaling technique has the potential to significantly reduce the number of elements required to perform finite element analysis. This will result in reduced computational costs (i.e. time and memory requirements).

It was demonstrated in Hewitt & Ahfock (2005) that whilst element savings for 2D models are significant, they are even greater when performing 3D analysis. For axial flux machines, even further savings will be made if the machine has multiple air gap regions.

An example of node and element savings when using a scaled air gap region for 2D finite element analysis is shown in Figures 5.3 and 5.4. The meshes shown in Figures 5.3(b) and 5.4(b) were generated using the finite element package FEMLAB (COMSOL, 2004). The mesh of Figure 5.3(b) required 2822 nodes and 5574 elements whereas that of Figure 5.4(b) only required 637 nodes and 1220 elements.

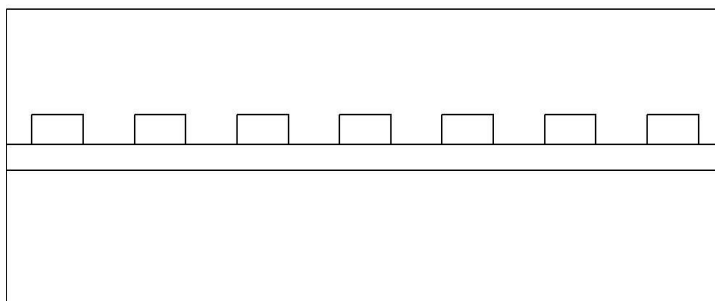


(a) 2D geometry with narrow air-gap region.

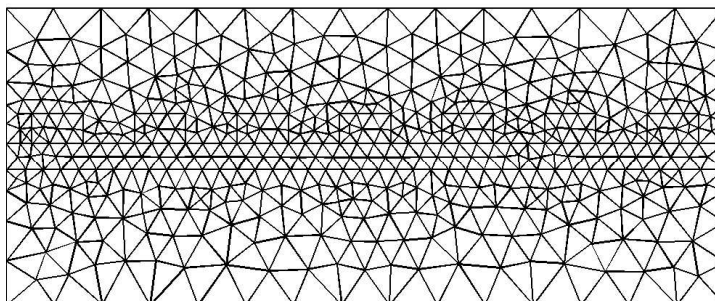


(b) Finite element mesh of the 2D geometry of Figure 5.3(a).

Figure 5.3: Finite element mesh of a 2D geometry with narrow air-gap region.



(a) 2D geometry of Figure 5.3(a) with a scaled ($\times 5$) air gap region.



(b) Finite element mesh of the 2D geometry of Figure 5.4(a).

Figure 5.4: Finite element mesh of a 2D geometry with scaled ($\times 5$) air-gap region.

When performing 3D finite element analysis of both the iron cores and air-gap region, as shown in Figure 5.5, the scaling technique can be used to improve the air-gap aspect ratio and thus significantly reduce the number of elements required to mesh the domain.

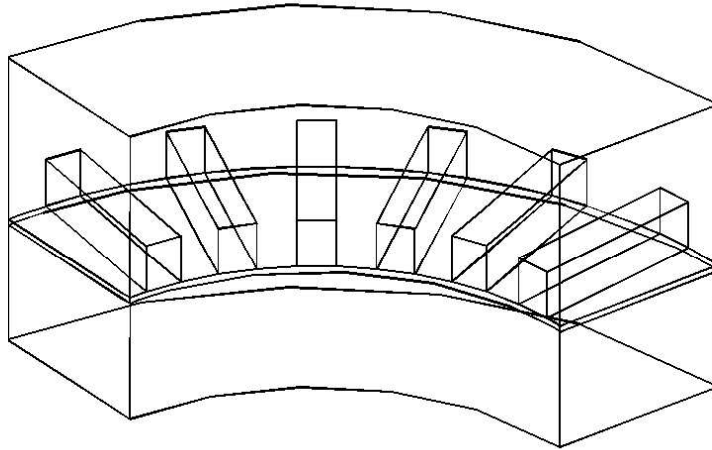


Figure 5.5: 3D model of the iron cores and air-gap region.

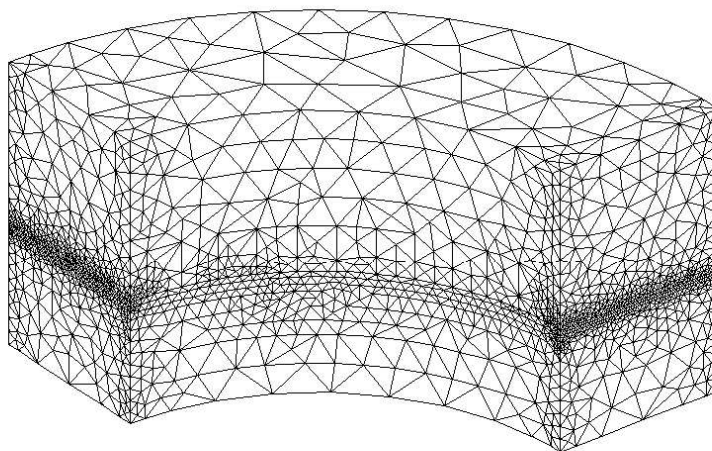


Figure 5.6: Finite element mesh of the geometry of Figure 5.5.

Figures 5.5 and 5.7 represent sections of a stator core, air gap and rotor for an unscaled and scaled problem, respectively. A general rotor region has been chosen for demonstration purposes. In practice the rotor geometry may include slots and the conductor cage for induction machines or a surface mounted magnet for a permanent magnet (PM) machine. The finite element meshes shown in Figures 5.6 and 5.8 were generated using

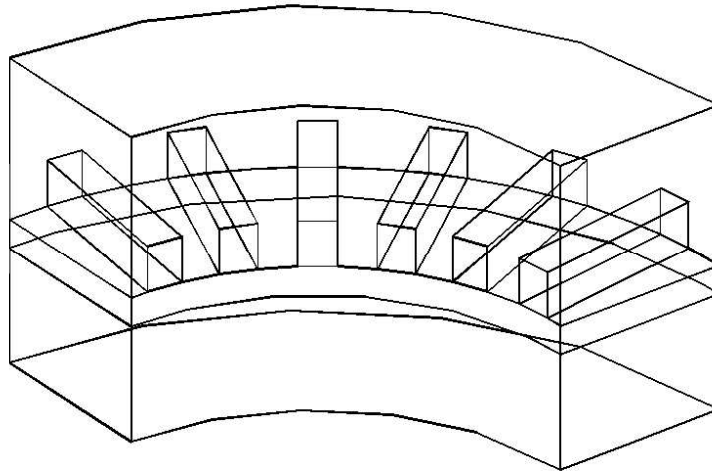


Figure 5.7: 3D model of the iron cores and scaled ($\times 5$) air-gap region.

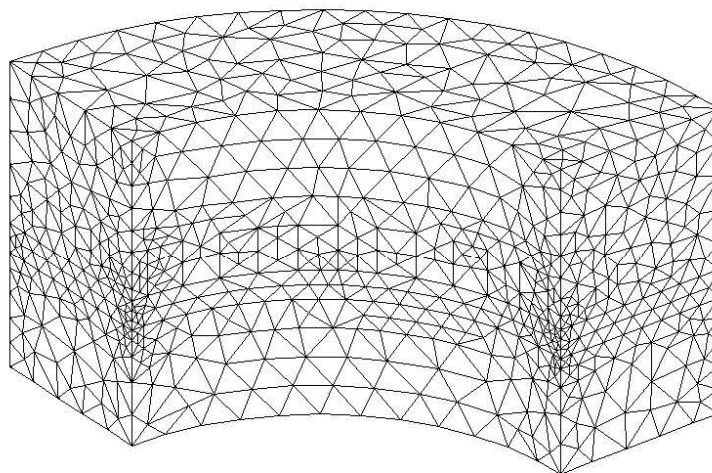


Figure 5.8: Finite element mesh of the geometry of Figure 5.7.

FEMLAB (COMSOL, 2004). The number of elements required to mesh the domains shown in Figures 5.5 and 5.7 were 44234 and 14119, respectively.

As stated earlier, the use of a coarser mesh may imply reduced solution accuracy, however if adaptive meshing or manual mesh refinement is used then the desired solution accuracy can be attained with fewer nodes. This was shown to be the case in Hewitt & Ahfock (2005).

Chapter 6

Conclusions

It is now well recognized that energy and natural resource conservation will play a vital role if sustainable development is to be achieved. Design of efficient electric machines requires a thorough understanding of the loss and flux density distributions within the machine. This knowledge allows a machine designer to both minimize losses and usage of core material.

Here we have predicted the presence of a radial component of the magnetic flux density distribution in the core of axial flux machines. The question then is what effect does this component have on core power loss and flux density distribution.

It is the aim of this research to answer this question and in doing so provide axial flux machine designers with a better understanding of the electromagnetic and thermal behaviour of these machines. An improved understanding of the loss and magnetic flux density distributions in the back-iron of axial flux machine cores will allow designers to design more efficient and economical AFMs.

In the following sections the key findings of the work presented here are briefly reviewed. Possible further work based on these findings are also discussed.

6.1 Curvature Related Radial Flux

The analytical model developed in Chapter 2 confirmed the presence of a radial component of the magnetic flux density in AFM cores. The magnitude of this component is dependent on the core permeability, physical dimensions and number of poles. While the model confirmed the presence of a radial component of the flux density, it also showed that the magnitude of this component is significantly less than that of the main flux components. This conclusion was further reinforced in Chapter 4 where it was shown that the radial component of the flux density is almost non-existent under a.c. conditions. In practice, this means that the radial component can be ignored with respect to its influence on the distribution of the circumferential and axial components of the flux density distribution in axial flux machine cores.

It was also concluded that, while the magnitude of the radial flux component is significantly less than that of the main flux components, the question of induced losses caused by this component still needs to be addressed. The need to address this question arises from the fact that radial flux flow is in the cross-laminate direction and thus has the potential to cause significant loss.

6.2 Losses due to Radial Flux

An axiperiodic coupled network model was developed in Chapter 3 to evaluate power loss due to curvature related radial flux in the laminated cores of axial flux machines. This model was used in Chapter 4 to evaluate these losses and to investigate the frequency dependence of the radial component of the flux density. It was found that if the core permeability, core conductivity and number of poles are high enough ($\mu > 1000\mu_o$, $\sigma > 10^6$, $p > 2$) then power loss due to curvature related cross-lamination flux is negligible compared to normal eddy current losses.

A closed form expression for power loss due to cross-lamination flux was also derived

in Chapter 4. This expression can be used to help axial flux machine designers make a quick assessment on whether or not power loss due curvature related radial flux is likely to be significant. If these losses are deemed significant, the axiperiodic model can be used to predict the losses more accurately.

Direct measurement of power loss due to cross-lamination flux is not possible. However, if values of total core loss are obtainable from laboratory tests, then, the component of power loss due cross-lamination flux can be isolated based on its frequency dependence. The technique to achieve this was developed in Chapter 4.

6.3 Magnetic Flux Density Distribution

The static model developed in Chapter 2 predicts peak back-iron flux density in the laminations near the outer radius of the core. Under the assumption of zero radial flux, which is justifiable in practice, flux redistribution in the core cannot occur and thus the lamination near the outer radius will experience the greatest overall circumferential flux density. Experimental data was presented which confirmed these predictions. It was also shown that the circumferential flux density near the outer radius is much higher than the average core back-iron circumferential flux density. This should be taken into consideration when sizing the core back iron if excessive saturation in this region is to be avoided.

The predictions made in Chapter 2 were further tested in Chapter 4. Here a quasi-static model was used and it was found that:

- a) The radial component of the magnetic flux density is almost non-existent under a.c. conditions.
- b) The amount of radial flux, although small, is a strong function of core permeability.
- c) The circumferential flux density is greatest near the outer radius of the core.

As discussed previously, finding c) has important practical implications for axial flux machine designers when sizing the core back-iron. Finding a) means that two-dimensional models can be used to predict both loss and flux density distributions in the back-iron of AFMs. An equation for main flux power loss was derived in Chapter 4 based on a two-dimensional model of the core. Finding a) also means that, in practical machines, the radial component does not influence the the flux density distribution in the core.

6.4 Sub-domain Scaling for Finite Element Analysis of Electric Machines

A sub-domain scaling technique for electromagnetic finite element analysis of electric machines was developed in Chapter 5. This technique can be used to overcome meshing difficulties when modeling axial flux machines with narrow air-gap regions. Whilst the technique does not directly contribute to the work presented in the previous chapters, it does provide a tool which could be used to extend the work beyond its current limitations.

The ability to include the air-gap region in a finite element analysis of an AFM would allow the effect of iron saturation and that of end-region flux to be investigated. It is likely that these effects will influence the electromagnetic and thermal behaviour of AFMs and thus are important areas of further research. It is proposed that the scaling technique presented here has the ability to overcome the problem of limited computing resources faced by anyone who intends to perform these types of analysis using the finite element method. Possible areas of further research are discussed in the following section.

6.5 Further Work

The work completed here has addressed three main issues. These can be broadly described as, the detection of a curvature related radial flux density component, prediction of core losses due to the radial flux component and determination of the magnetic flux density distribution in the back-iron of axial flux machines.

The use of Soft Magnetic Composites (SMC) in the construction of axial flux machine cores is an area of great interest. In SMC cores radial flux is not inhibited nor does it incur additional eddy current loss. The resultant magnetic flux density redistribution would mean that the axial length of the core back iron could be reduced. The analysis presented here would allow machine designers using SMC to investigate this possibility.

The presence of a radial flux density component also has potentially significant impact on solid rotor designs. In a solid core the radial flux is not inhibited, however the shielding effect is likely to be significant. Additionally, harmonics introduced by variable speed drives are likely to affect core losses. An investigation into these phenomena would be of great interest and complement the work presented here.

The models developed in the dissertation are based on the assumption of linear material properties and have neglected the influence of end effects. Both material non-linearity and end-effects would have some influence on the conclusions presented.

Using finite element analysis, a preliminary investigation of the influence of end effects on the radial flux density was made. The flux density entering the core along a radial line was based on that given in Bumby et al. (2004), where it was shown that the magnetic flux density entering the core increases at the core edges. Not surprisingly, the total radial flux increased and, compared with Figure 2.6, the peak radial flux density occurs closer to the outer radius. In other words, radial flux due to end-effects adds to that caused by core curvature. Further investigation into additional power loss due to end effect related radial flux needs to be carried out. It also seems likely that the additional flux entering the core at the radial ends due to end effects will cause the

laminations toward the outer radius to become magnetically saturated. Thus the flux entering the core due to end effects may need to be considered when sizing the core back-iron.

Effective use of core iron in electrical machines generally requires some regions of the core to be pushed toward magnetic saturation. As shown in the preceding chapters, this may occur in the laminations near the outer radius of the core. For a slotted machine tooth saturation may also occur at the inner radius of the core. Three-dimensional non-linear analysis would be required for a rigorous study of iron saturation and its effect on the core and air-gap flux density distributions. Such an analysis would require both the iron and air-gap regions to be modeled, which would be computationally expensive even when the scaling technique is used. Thus further research needs to be carried out on possible techniques that could be used to model the effects of saturation within the limitations of available computing resources.

References

- Abdel-Razek, A., Coulomb, J., Feliachi, M. & Sabonnadiere, J. (1982), ‘Conception of an air-gap element for the dynamic analysis of the electromagnetic field in electric machines’, *IEEE Transactions on Magnetics* **MAG-18**(2), 655–659.
- Adams, V. & Askenazi, A. (1999), *Building Better Products with Finite Element Analysis*, OnWord Press, Santa Fe NM. USA.
- Balchin, M. J. & Davidson, J. A. M. (1980), ‘Numerical method for calculating magnetic-flux and eddy-current distributions in three dimensions’, *IEE Proceedings* **127**(1), 46–53. Part A.
- Balchin, M. J. & Davidson, J. A. M. (1983), ‘3-dimensional eddy-current calculation by the network method’, *Proceedings of the IEE* **130**(2), 88–92. Part A.
- Barbisio, E., Fiorillo, F. & Ragusa, C. (2004), ‘Predicting loss in magnetic steels under arbitrary induction waveform and with minor hysteresis loops’, *IEEE Transactions on Magnetics* **40**(4), 1810–1819.
- Binns, B. J., Lawrenson, P. J. & Trowbridge, C. W. (1992), *The Analytical and Numerical Solution of Electric and Magnetic Fields*, Wiley and Sons.
- Boldea, I., Rahman, A. & Nasar, S. A. (1975), ‘Finite-width, finite-thickness, and saturation effects in solid-rotor induction machines’, *IEEE Transactions on Power Apparatus and Systems* **PAS-94**(5), 1500–1507.
- Brown, N., Haydock, L. & Bumby, J. R. (2002), An idealised geometric approach to

- electromagnetically comparing axial and radial PM machines, *in* 'ICEM', Bruges, Belgium.
- Bumby, J. R., Martin, R., Mueller, M. A., Spooner, E., Brown, N. L. & Chalmers, B. J. (2004), 'Electromagnetic design of axial-flux permanent magnet machines', *IEE Proceedings - Electric Power Applications* **151**(2), 151–160.
- Campbell, P. (1974), 'Principles of a permanent-magnet axial-field d.c. machine', *Proceedings of the IEE* **121**(12), 1489–1494.
- Carpenter, C. J. (1975*a*), 'Finite-element network models and their application to eddy-current problems', *Proceedings of the IEE* **122**(4), 455–462.
- Carpenter, C. J. (1975*b*), 'A network approach to the numerical solution of eddy-current problems', *IEEE Transactions on Magnetics* **Mag-11**(5), 1517–1522.
- Carpenter, C. J. (1975*c*), 'Three-dimensional numerical solution of eddy currents in thin plates', *Proceedings of the IEE* **122**(6), 681–688.
- Carpenter, C. J. (1977), 'Theory of flux penetration into laminated iron and associated losses', *Proceedings of the IEE* **124**(7), 659–664.
- Chan, C. C. (1987), 'Axial-field electrical machines – design and applications', *IEEE Transactions on Energy Conversion* **EC-2**(2), 294–300.
- Chan, C. C. & Leung, W. S. (1980), 'A new design approach for axial-field electrical machines', *IEEE Transactions on Power Apparatus and Systems* **PAS-99**(4), 1679–1685.
- Chandler, P. L. & Patterson, D. J. (2001), 'Counting the losses in very high efficiency machine design - contemporary computer simulation techniques and results encountered in very high efficiency electric machine design for renewable energy applications', *Renewable Energy* **22**, 143–150.
- Chari, M. & Salon, S. (2000), *Numerical Methods in Electromagnetism*, Academic Press.

- Choi, H. S., Kim, D. H., Park, I. H. & Hahn, S. Y. (2001), ‘A new design technique of magnetic systems using space mapping algorithm’, *IEEE Transactions on Magnetics* **37**(5), 3627–3630.
- COMSOL (2004), *FEMLAB 3 Electromagnetics Module User’s Guide*, FEMLAB 3.0 edn, COMSOL AB.
- Davidson, J. A. M. & Balchin, M. J. (1981), ‘Experimental verification of network methods for calculating flux and eddy-current distributions in three dimensions’, *IEE Proceedings* **128**(7), 492–496. Part A.
- Davidson, J. & Balchin, M. (1983), ‘Three dimensional eddy current calculation using a network method’, *IEEE Transactions on Magnetics* **MAG-19**(6), 2325–2328.
- DeBortoli, M., Lee, M., Salon, S. & Lee, K. (1991), ‘Coupling finite elements and analytical solution in the airgap of electric machines’, *IEEE Transactions on Magnetics* **27**(5), 3955–3957.
- Demenko, A. (2000), ‘Three dimensional eddy current calculation using reluctance-conductance network formed by means of FEM method’, *IEEE Transactions on Magnetics* **36**(4), 741–745.
- Demenko, A., Nowak, L. & Szelag, W. (1998), ‘Reluctance network formed by means of edge element method’, *IEEE Transactions on Magnetics* **34**(5), 2485–2488.
- Feliachi, M., Coulomb, J. & Mansir, H. (1983), ‘Second order air-gap element for the dynamic finite-element analysis of the electromagnetic field in electric machines’, *IEEE Transactions on Magnetics* **MAG-19**(6), 2300–2303.
- Fiorillo, F. & Novikov, A. (1990), ‘An improved approach to power losses in magnetic laminations under nonsinusoidal induction waveform’, *IEEE Transactions on Magnetics* **26**(5), 2904–2910.
- Fitzgerald, A. E., Jr., C. K. & Umans, S. D. (1992), *Electric Machinery*, fifth edn, McGraw Hill, Singapore.

- Guerin, C., Tanneau, G., Meunier, G., Brunotte, X. & Albertini, J. (1994), 'Three dimensional magnetostatic finite elements for gaps and iron shells using magnetic scalar potentials', *IEEE Transactions on Magnetics* **30**(5), 2885–2888.
- Guo, Y. & Zhu, J. (2002), 'Magnetic field calculation of claw pole permanent magnet machines using magnetic network method', *Journal of Electrical and Electronics Engineering* **22**(1), 69–75.
- Henrotte, F., Meys, B., Hedia, H., Dular, P. & Legros, W. (1999), 'Finite element modelling with transformation techniques', *IEEE Transactions on Magnetics* **35**(3), 1434–1437.
- Hewitt, A. J. & Ahfock, A. (2005), 'Sub-domain scaling for finite element analysis of electrical machines', *IEE Proceedings - Electric Power Applications* **152**(2), 149–156.
- Hewitt, A. J., Ahfock, A. & Suslov, S. A. (2005), 'Magnetic flux density distribution in axial flux machine cores', *IEE Proceedings - Electric Power Applications* **152**(2), 292–296.
- Huang, S., Aydin, M. & Lipo, T. A. (2002), A direct approach to electrical machine performance evaluation: Torque density assessment and sizing optimisation, *in* 'ICEM', Bruges, Belgium.
- Huang, S., Luo, J., Leonardi, F. & Lipo, T. A. (1999), 'A comparison of power density for axial flux machines based on general purpose sizing equations', *IEEE Transactions on Energy Conversion* **14**(2), 185–192.
- King, E. I. (1966a), 'Equivalent circuits for two-dimensional magnetic fields: I - the static field', *IEEE Transactions on Power Apparatus and Systems* **PAS-85**(9), 927–935.
- King, E. I. (1966b), 'Equivalent circuits for two-dimensional magnetic fields: II - the sinusoidally time-varying field', *IEEE Transactions on Power Apparatus and Systems* **PAS-85**(9), 936–945.

- Lammeraner, J. & Staff, M. (1966), *Eddy Currents*, ILIFFE Books Ltd., London.
- Melissen, J. B. M. & Simkin, J. (1990), ‘A new coordinate transform for the finite element solution in magnetostatics’, *IEEE Transactions on Magnetics* **26**(2), 391–394.
- Ouazzani, W. E., Rioux-Damidau, F., Brunotte, X. & Meunier, G. (1999), ‘Finite element modelling of unbounded problems: Use of geometric transformation and comparison with boundary integral method’, *IEEE Transactions on Magnetics* **32**(3), 1401–1404.
- Patterson, D. J. & Spee, R. (1995), ‘The design and development of an axial flux permanent magnet brushless DC motor for wheel drive in a solar powered vehicle’, *IEEE Transactions on Industry Applications* **31**(5), 1054–1061.
- Ratnajeevan, S. & Hoole, H. (1995), *Finite Elements, Electromagnetics and Design*, Elsevier Science B. V., Amsterdam.
- Reece, A. & Preston, T. (2000), *Finite Element Methods in Electrical Power Engineering*, Oxford University Press Inc., New York.
- Roisse, H., Hecquet, M. & Brochet, P. (1998), ‘Simulation of synchronous machines using a electric-magnetic coupled network model’, *IEEE Transactions on Magnetics* **34**(5), 3656–3659.
- Salon, S. (1995), *Finite Element Analysis of Electrical Machines*, Kluwer Academic Publishers, 101 Philip Drive, Assinippi Park, Norwell, Massachusetts 02061.
- Sykulski, J. K. (1995), *Computational Magnetism*, James & James Ltd. and Chapman & Hall, London.
- Varga, J. S. (1986), ‘Magnetic and dimensional properties of axial induction motors’, *IEEE Transactions on Energy Conversion* **EC-1**(2), 137–144.
- Zhang, Z., Profumo, F. & Tenconi, A. (1996), ‘Axial-flux versus radial-flux permanent-magnet motors’, *Electromotion* **3**, 134–140.

- Zhilichev, Y. N. (1998), 'Three-dimensional analytic model of permanent magnet axial flux machine', *IEEE Transactions on Magnetics* **34**(6), 3897–3901.

Appendix A

Bessel Function Orthogonality

We now prove the orthogonality property of Bessel functions with respect to a scaling coefficient within the fixed region $r \in [s; 1]$ when homogeneous derivative boundary conditions are imposed.

Consider the Bessel Differential Equation (BDE)

$$r^2 R'' + rR' + (r^2 k_n^2 - m^2)R = 0 \quad (\text{A.1})$$

where k_n ($n = 1, 2, 3, \dots$) is the eigenvalue ensuring the existence of a nontrivial solution of equation (A.1) with the following derivative boundary conditions

$$R_1'(k_n s) = R_1'(k_n) = 0. \quad (\text{A.2})$$

Let

$$R_1 = A_1 J_m(k_n r) + B_1 Y_m(k_n r) \quad (\text{A.3})$$

and

$$R_2 = A_2 J_m(k_l r) + B_2 Y_m(k_l r) \quad (\text{A.4})$$

be two distinct solutions of equation (A.1) with boundary conditions (A.2). Here J_m and Y_m are Bessel functions of the first and second kind, respectively, of order m , A_1 , A_2 , B_1 and B_2 are undefined constants and $n \neq l$. Then

$$r \left(r R_1' \right)' + (k_n^2 r^2 - m^2) R_1 = 0 \quad (\text{A.5})$$

and

$$r \left(r R_2' \right)' + (k_l^2 r^2 - m^2) R_2 = 0. \quad (\text{A.6})$$

Multiply equation (A.5) by R_2 , equation (A.6) by R_1 and subtract the results to give

$$(k_n^2 - k_l^2) r R_1 R_2 = R_1 \left(r R_2' \right)' - R_2 \left(r R_1' \right)' . \quad (\text{A.7})$$

Now integrate both sides of equation (A.7) over the region to obtain

$$(k_n^2 - k_l^2) \int_s^1 r R_1 R_2 \, dr = \int_s^1 \left[R_1 \left(r R_2' \right)' - R_2 \left(r R_1' \right)' \right] dr. \quad (\text{A.8})$$

Since

$$R_1 \left(r R_2' \right)' - R_2 \left(r R_1' \right)' = \frac{d}{dr} \left[r R_1 R_2' - r R_1' R_2 \right] \quad (\text{A.9})$$

equation (A.8) becomes

$$(k_n^2 - k_l^2) \int_s^1 r R_1 R_2 \, dr = \left[r R_1 R_2' - r R_1' R_2 \right]_s^1. \quad (\text{A.10})$$

The right hand side of equation (A.10) is equal to zero according to the boundary conditions (A.2) and thus

$$\int_s^1 r R_1(k_n r) R_2(k_l r) \, dr = 0 \quad \text{for } n \neq l \quad (\text{A.11})$$

which demonstrates orthogonality.

For the case $n = l$ multiply the BDE (A.1) by $2R'$ to obtain

$$2r^2 R' R'' + 2r \left(R' \right)^2 + 2 \left(r^2 k_n^2 - m^2 \right) R R' = 0$$

or equivalently

$$\left(r^2 \left(R' \right)^2 \right)' + \left(r^2 k_n^2 - m^2 \right) \left(R^2 \right)' = 0.$$

Integrating over the region gives

$$\int_s^1 \left[\left(r^2 \left(R' \right)^2 \right)' - \left(m^2 R^2 \right)' + r^2 k_n^2 \left(R^2 \right)' \right] dr = 0$$

or

$$\left[r^2 (R')^2 - m^2 R^2 \right]_s^1 + k_n^2 \int_s^1 r^2 (R^2)' dr = 0. \quad (\text{A.12})$$

Using the homogeneous boundary conditions (A.2) in equation (A.12) and integrating by parts results in

$$m^2 [R^2(k_n) - R^2(k_n s)] - k_n^2 \left[r^2 [R^2(k_n) - R^2(k_n s)] - 2 \int_s^1 r R^2(k_n r) dr \right] = 0 \quad (\text{A.13})$$

which can be rearranged to obtain

$$\int_s^1 r R^2(k_n r) dr = \frac{1}{2k_n^2} [(m^2 - k_n^2 s^2) R^2(k_n s) - (m^2 - k_n^2) R^2(k_n)]. \quad (\text{A.14})$$

Appendix B

Air-Gap Flux Density Distribution

B.1 Air-Gap Magnetic Flux Density

The separation of variables technique used to produce the analytical solution for the core of an axial flux machine (see Section 2.1) can also be applied to the air-gap region to investigate the behaviour of the axial component of the magnetic flux density in the radial direction at the air-iron boundary. The assumption of constant axial magnetic flux density with radius used in Section 2.1 is also shown to be valid for narrow air-gaps.

The analytical solution for the air-gap magnetic flux density is obtained as follows.

- a) The air-gap boundaries are formed by the stator and rotor regions with magnetic insulation assumed elsewhere. Our analysis is restricted to the effects of the magnetising currents in the stator. These currents can be represented by a uniformly distributed current sheet in the $r - \theta$ plane at the stator air-gap boundary. The current sheet is defined such that it produces the same fundamental component of the air-gap mmf wave as the physical windings (Fitzgerald et al., 1992). The

current sheet equation is found by considering a purely radial current with sinusoidal variation in the angular direction θ . For a p -pole machine this produces the equation

$$\int_0^{\frac{2\pi}{p}} J(r, \theta) r d\theta = I \quad (\text{B.1})$$

where I is the total imposed current flowing in one pole pitch, and $J(r, \theta)$ is the surface current density.

Let

$$J(r, \theta) = J'(r) \sin\left(\frac{p}{2}\theta\right). \quad (\text{B.2})$$

Substituting (B.2) into (B.1) we obtain

$$\begin{aligned} \int_0^{\frac{2\pi}{p}} J'(r) \sin\left(\frac{p}{2}\theta\right) r d\theta &= I \\ \Rightarrow \frac{4r}{p} J'(r) &= I \end{aligned} \quad (\text{B.3})$$

and upon substituting (B.3) into (B.2) the current density is expressed in terms of the imposed current per pole pitch by

$$J(r, \theta) = \frac{Ip}{4r} \sin\left(\frac{p\theta}{2}\right). \quad (\text{B.4})$$

- b) The magnetostatic problem is formulated in the same way as that used to model the core (see Section 2.1) and thus the defining equation is

$$\nabla \cdot (M' \nabla \phi') = 0. \quad (\text{B.5})$$

The permeability matrix in the air-gap is given by

$$M' = \begin{bmatrix} \mu_o & 0 & 0 \\ 0 & \mu_o & 0 \\ 0 & 0 & \mu_o \end{bmatrix}, \quad (\text{B.6})$$

where μ_o is the permeability of free space. This simplifies equation (B.5) to the Laplace equation

$$\nabla^2 \phi' = 0. \quad (\text{B.7})$$

In coordinate form equation (B.7) becomes

$$\frac{\partial^2 \phi'}{\partial r'^2} + \frac{1}{r'} \frac{\partial \phi'}{\partial r'} + \frac{1}{r'^2} \frac{\partial^2 \phi'}{\partial \theta^2} + \frac{\partial^2 \phi'}{\partial z'^2} = 0. \quad (\text{B.8})$$

Non-dimensionalising the problem using (2.8) we obtain

$$\frac{\partial^2 \phi}{\partial r^2} + \frac{1}{r} \frac{\partial \phi}{\partial r} + \frac{1}{r^2} \frac{\partial^2 \phi}{\partial \theta^2} + \frac{b^2}{\delta^2} \frac{\partial^2 \phi}{\partial z^2} = 0. \quad (\text{B.9})$$

c) We now introduce the following boundary conditions:

- 1) at $z' = 0$ the air-gap adjoins the iron and the conservation of the tangential components of the magnetic field intensity \vec{H} must be adhered to. If the iron is assumed to have infinite permeability, then the tangential components of \vec{H} are zero. This results in the boundary conditions

$$\begin{aligned} B'_r|_{z'=0} &= B'_\theta|_{z'=0} = 0 \\ \Rightarrow \frac{\partial \phi}{\partial r}|_{z=0} &= \frac{\partial \phi}{\partial \theta}|_{z=0} = 0; \end{aligned} \quad (\text{B.10})$$

- 2) magnetic insulation is assumed at the inner and outer radii boundaries to produce the radial boundary conditions

$$\begin{aligned} B'_r|_{r'=a \text{ and } r'=b} &= 0 \\ \Rightarrow \frac{\partial \phi}{\partial r}|_{r=s \text{ and } r=1} &= 0, \end{aligned} \quad (\text{B.11})$$

where $s = (a/b)$;

- 3) at $z' = \delta$ the radial current sheet of equation (B.3) is assumed. The boundary condition is modeled using the continuity condition of the magnetic field intensity

$$\hat{n} \times (\vec{H}'_1 - \vec{H}'_2) = \vec{J}_n \quad (\text{B.12})$$

where \hat{n} is a unit vector normal to the boundary plane, \vec{H}'_1 and \vec{H}'_2 are the magnetic field intensity vectors on either side of the boundary and \vec{J}_n is the normal component of the boundary current density. The current sheet

is defined to have only a radial current component, and thus the current density will also only have a radial component (i.e. $\vec{J}_n = (J_r, 0, 0)$). Imposing this condition on equation (B.12) and assuming the stator iron is of infinite permeability results in

$$H'_\theta = -J_r \quad (\text{B.13})$$

and thus

$$\begin{aligned} B'_\theta|_{z'=\delta} &= -\mu_0 \frac{IP}{4r} \sin\left(\frac{p\theta}{2}\right) \\ \Rightarrow \frac{\partial\phi}{\partial\theta}|_{z=1} &= \frac{-IP}{4\phi_0} \sin\left(\frac{p\theta}{2}\right). \end{aligned} \quad (\text{B.14})$$

We choose

$$\phi_0 = \frac{IP}{4} \quad (\text{B.15})$$

which results in

$$\frac{\partial\Phi}{\partial\theta}|_{z=1} = -\sin\left(\frac{p\theta}{2}\right). \quad (\text{B.16})$$

d) Upon applying the separation of variables technique equation (B.9) becomes

$$\frac{R''}{R} + \frac{1}{r} \frac{R'}{R} + \frac{1}{r^2} \frac{\varphi''}{\varphi} + \frac{b^2}{\delta^2} \frac{Z''}{Z} = 0, \quad (\text{B.17})$$

where the primes denote the respective derivatives. Consistency of equation (B.17) requires that

$$\frac{Z''}{Z} = k_n^2 \frac{\delta^2}{b^2}, \quad n = 1, 2, 3, \dots \quad (\text{B.18})$$

and

$$\varphi = \cos(l\theta) \quad (\text{to ensure angular periodicity}), \quad (\text{B.19})$$

where k_n are real constants and $l = (p/2)$. Substituting (B.18) and (B.19) into (B.17) results in

$$r^2 R'' + r R' + (r^2 k_n^2 - l^2) R = 0. \quad (\text{B.20})$$

Equation (B.20) is a Bessel Differential Equation (BDE), the solution of which is of the form $R_l(k_n r) = c_1 J_l(k_n r) + c_2 Y_l(k_n r)$ where J_l and Y_l are Bessel functions of the first and second kind, respectively, of order l . Enforcing the radial boundary

conditions defined in equation (B.11) leads to the nonlinear eigenvalue problem for k_n

$$J'_l(k_n s) Y'_l(k_n) = J'_l(k_n) Y'_l(k_n s). \quad (\text{B.21})$$

Equation (B.18) is now solved using the boundary conditions defined in equation (B.10) and the periodicity condition defined in equation (B.19) as follows. Let

$$\begin{aligned} \frac{Z''}{Z} &= k_n^2 \frac{\delta^2}{b^2} = g_n^2 \\ \Rightarrow Z &= A \cosh(g_n z) + B \sinh(g_n z). \end{aligned} \quad (\text{B.22})$$

The boundary conditions (B.10) and the periodicity condition (B.19) requires that

$$\begin{aligned} R' \cos(l\theta) Z|_{z=0} &= 0 \\ \Rightarrow R' Z|_{z=0} &= 0, \end{aligned} \quad (\text{B.23})$$

and

$$\begin{aligned} -Rl \sin(l\theta) Z|_{z=0} &= 0 \\ \Rightarrow RZ|_{z=0} &= 0. \end{aligned} \quad (\text{B.24})$$

The non-trivial solution to (B.23) and (B.24) is

$$Z|_{z=0} = 0$$

and thus

$$Z = B \sinh(g_n z), \quad (\text{B.25})$$

where B is some constant and $g_n = [(k_n \delta) / b]$.

The solution for ϕ is then

$$\phi = \sum_{n=1}^{\infty} C_n \left[J_l(k_n r) - \frac{J'_l(k_n s)}{Y'_l(k_n s)} Y_l(k_n r) \right] \cos(l\theta) \sinh(g_n z). \quad (\text{B.26})$$

For algebraic simplicity of the solution we redefine the coefficient C_n so that

$$\phi = \sum_{n=1}^{\infty} C_n \left[J_l(k_n r) - \frac{J'_l(k_n s)}{Y'_l(k_n s)} Y_l(k_n r) \right] \frac{\cos(l\theta)}{l} \frac{\sinh(g_n z)}{\sinh(g_n)}. \quad (\text{B.27})$$

Applying boundary condition (B.16) to (B.27) results in the following infinite series

$$\sum_{n=1}^{\infty} C_n \left[J_l(k_n r) - \frac{J'_l(k_n s)}{Y'_l(k_n s)} Y_l(k_n r) \right] = 1. \quad (\text{B.28})$$

Using the orthogonality relationships derived in Appendix A, the unknown coefficients in (B.27) are found to be

$$C_n = \frac{2k_n^2 \int_s^1 r \left[J_l(k_n r) - \tilde{k} Y_l(k_n r) \right] dr}{l^2 (R_l^2(k_n s) - R_l^2(k_n)) + k_n^2 (R_l^2(k_n) - s^2 R_l^2(k_n s))} \quad (\text{B.29})$$

where

$$\tilde{k} = \frac{J'_l(k_n s)}{Y'_l(k_n s)}$$

and

$$R_l(s) = J_l(k_n s) - \tilde{k} Y_l(k_n s).$$

In accordance with (B.5), (B.6), (2.1) and (2.8) the components of the dimensional magnetic flux density within the air-gap region are given by

$$B'_r = \mu_0 \frac{I_p}{4b} \frac{\partial \phi}{\partial r}, \quad (\text{B.30})$$

$$B'_\theta = \mu_0 \frac{I_p}{4r'} \frac{\partial \phi}{\partial \theta}, \quad (\text{B.31})$$

$$B'_z = \mu_0 \frac{I_p}{4\delta} \frac{\partial \phi}{\partial z}. \quad (\text{B.32})$$

B.2 Narrow Air-Gaps

In the limit $\delta \rightarrow 0$ equation (B.9) can be rewritten as

$$\frac{\delta^2}{b^2} \frac{\partial^2 \Phi}{\partial r^2} + \frac{\delta^2}{b^2} \frac{1}{r} \frac{\partial \Phi}{\partial r} + \frac{\delta^2}{b^2} \frac{1}{r^2} \frac{\partial^2 \Phi}{\partial \theta^2} + \frac{\partial^2 \Phi}{\partial z^2} = 0 \quad (\text{B.33})$$

which has terms of order unity and (δ^2/b^2) only. Let

$$\Phi = \Phi_0 + \epsilon^2 \Phi_2 + \dots \quad (\text{B.34})$$

where $\epsilon = \delta/b$, and substitute (B.34) into (B.33) to give

$$\frac{\partial^2 \Phi_0}{\partial z^2} + \epsilon^2 \left(\frac{\partial^2 \Phi_0}{\partial r^2} + \frac{1}{r} \frac{\partial \Phi_0}{\partial r} + \frac{1}{r^2} \frac{\partial^2 \Phi_0}{\partial \theta^2} + \frac{\partial^2 \Phi_2}{\partial z^2} \right) + \dots = 0. \quad (\text{B.35})$$

In the limit $\epsilon \rightarrow 0$ equation (B.35) becomes

$$\begin{aligned} \frac{\partial^2 \Phi_0}{\partial z^2} &= 0 \\ \Rightarrow \Phi_0 &= z f_1(r, \theta) + f_2(r, \theta) \end{aligned} \quad (\text{B.36})$$

where f_1 and f_2 are undetermined functions of r and θ .

Enforcing boundary conditions (B.10), (B.11) and (B.16) we obtain

$$\Phi = z \frac{2}{p} \cos\left(\frac{p\theta}{2}\right)$$

and thus

$$B_z = \frac{\partial \Phi}{\partial z}$$

is a function of angular displacement θ only, and is independent of radius r . This validates the assumption of uniform axial magnetic flux density in the radial direction at the air-iron boundary for narrow air-gaps. However, boundary condition (B.11) eliminates end effects and thus this assumption is only valid away from the radial ends of the core. Work performed by Zhilichev (1998) confirms that this is the case in practice.

Appendix C

Two-Dimensional Magnetostatic Model

If the radial component of the magnetic flux density can be neglected the magnetostatic solution for the simplified core given in section 2.1 can be reduced to a simpler two-dimensional solution. The assumptions stated in Section 2.1.1 are applied and the defining model equation is

$$\nabla \cdot (M' \nabla \phi') = 0, \quad (\text{C.1})$$

where M' is the permeability tensor given by

$$M' = \begin{bmatrix} 0 & 0 & 0 \\ 0 & \mu_\theta & 0 \\ 0 & 0 & \mu_z \end{bmatrix}. \quad (\text{C.2})$$

The boundary conditions are defined by:

- a) Magnetic insulation located at the lower z -plane boundary,

$$B'_z|_{z'=0} = 0 \quad (\text{C.3})$$

b) The magnetic flux injection boundary,

$$B'_z|_{z'=\delta} = P \sin\left(\frac{p\theta}{2}\right) \quad (\text{C.4})$$

where B'_z is the axial component of the magnetic flux density, P is the peak imposed flux density, δ is the core axial length, and $0 \leq \theta \leq 2\pi$ is the angular coordinate.

In coordinate form equation (C.1) becomes

$$\frac{\mu_\theta}{r'^2} \frac{\partial^2 \phi'}{\partial \theta^2} + \mu_z \frac{\partial^2 \phi'}{\partial z'^2} = 0. \quad (\text{C.5})$$

The problem is non-dimensionalised as follows

$$\begin{aligned} \phi' &= \phi \phi_o \\ z' &= z \delta \end{aligned} \quad (\text{C.6})$$

where δ is the iron thickness and ϕ_o is the characteristic value of the potential. The permeability tensor (C.2) becomes

$$M = \begin{bmatrix} 0 & 0 & 0 \\ 0 & k_{z\theta} & 0 \\ 0 & 0 & 1 \end{bmatrix}, \quad (\text{C.7})$$

where $k_{z\theta} = \mu_\theta / \mu_z$. The non-dimensional form of equation (C.5) is

$$\frac{\partial^2 \phi}{\partial \theta^2} + \frac{r'^2}{k_{z\theta} \delta^2} \frac{\partial^2 \phi}{\partial z^2} = 0. \quad (\text{C.8})$$

Comparing equations (C.8) and (2.10) it can be seen that in the limit $\mu_r = 0$ the 3D equation is reduced to that of the 2D problem. The non-dimensional boundary conditions corresponding to (C.3) and (C.4), respectively, are given by

$$\left. \frac{\partial \phi}{\partial z} \right|_{z=0} = 0 \quad (\text{C.9})$$

and

$$\begin{aligned} \mu_z \frac{\phi_o}{\delta} \left. \frac{\partial \phi}{\partial z} \right|_{z=1} &= P \sin\left(\frac{p\theta}{2}\right) \\ \Rightarrow \left. \frac{\partial \phi}{\partial z} \right|_{z=1} &= \sin\left(\frac{p\theta}{2}\right). \end{aligned} \quad (\text{C.10})$$

and we choose

$$\phi_o = \frac{P\delta}{\mu_z} \quad (\text{C.11})$$

to simplify the boundary condition (C.10).

Separation of variables is now used to solve (C.8). Substitution of

$$\phi = \varphi(\theta) \cdot Z(z; r'),$$

where r' enters only as a parameter, in equation (C.8) gives

$$\frac{\varphi''}{\varphi} + \frac{r'^2}{k_{z\theta}\delta^2} \frac{Z_{zz}}{Z} = 0, \quad (\text{C.12})$$

where primes denote derivatives with respect to θ and Z_{zz} is the second derivative of Z with respect to z . To ensure angular periodicity it is required that

$$\frac{\varphi''}{\varphi} = -l^2 \quad (\text{C.13})$$

where $l = (p/2)$. Substituting (C.13) into (C.12) we obtain

$$\frac{Z_{zz}}{Z} = k_{z\theta} \left(\frac{\delta l}{r'} \right)^2. \quad (\text{C.14})$$

Equation (C.14) is now solved using boundary conditions (C.9) and (C.10) as follows.

Let

$$\begin{aligned} \frac{Z_{zz}}{Z} &= k_{z\theta} \left(\frac{\delta l}{r'} \right)^2 = g^2 \\ \Rightarrow Z &= Ae^{gz} + Be^{-gz}. \end{aligned} \quad (\text{C.15})$$

Boundary condition (C.9) requires that

$$A = B, \quad (\text{C.16})$$

and boundary condition (C.10) requires that

$$\begin{aligned} Age^g - Bge^{-g} &= 1 \\ \Rightarrow Ag [e^g - e^{-g}] &= 1 \\ \Rightarrow A &= \frac{1}{g(e^g - e^{-g})}. \end{aligned} \quad (\text{C.17})$$

Substituting (C.16) and (C.17) into equation (C.15) results in

$$Z = \frac{e^{zg} + e^{-zg}}{g(e^g - e^{-g})} \quad (\text{C.18})$$

and thus the solution to equation (C.8) is

$$\begin{aligned}\phi &= \frac{(e^{zg} + e^{-zg})}{g(e^g - e^{-g})} \sin(l\theta) \\ &= \frac{1 \cosh(gz)}{g \sinh(g)} \sin(l\theta),\end{aligned}\tag{C.19}$$

where $g = \delta l \sqrt{k_{z\theta}}/r'$. In accordance with equations (2.1), (C.1), (C.2) and (C.6), the non-zero components of the dimensional magnetic flux density within the core are given by

$$B'_\theta = \frac{\mu_\theta P \delta}{\mu_z r'} \frac{\partial \phi}{\partial \theta},\tag{C.20}$$

$$B'_z = P \frac{\partial \phi}{\partial z}.\tag{C.21}$$

As a simple test of the validity of equation C.20, it is easy to show that

$$\frac{1}{\delta} \int_0^1 B'_\theta \partial z = \frac{4Pr'}{p}\tag{C.22}$$

which demonstrates that B'_θ averaged in the axial direction is proportional to r , as we would expect from the excitation boundary condition.

Appendix D

Proof of Sinusoidal Periodicity in the Circumferential Direction

We now show that the assumption of sinusoidal periodicity in the circumferential direction used in Section 3.4 is valid. This assumption is based on the angular periodicity in the core-air gap boundary condition and the uniformity of the core in the circumferential direction.

We begin our proof with the partial differential equations given in (3.43) and (3.44). For convenience these equations are restated here as (D.1) and (D.2), respectively.

$$\nabla \times (\sigma^{-1} \nabla \times \vec{T}) = -j\omega [\mu (\vec{T} \times \nabla \Omega)] \quad (\text{D.1})$$

$$\nabla \cdot \mu \vec{T} - \nabla \cdot \mu \nabla \Omega = 0 \quad (\text{D.2})$$

Substituting $\vec{T} = (T_r, 0, 0)$ into equation (D.2) gives

$$\frac{\mu_r}{r} \frac{\partial (rT_r)}{\partial r} - \mu_r \frac{\partial^2 \Omega}{\partial r^2} - \frac{\mu_r}{r} \frac{\partial \Omega}{\partial r} - \frac{\mu_\theta}{r^2} \frac{\partial^2 \Omega}{\partial \theta^2} - \mu_z \frac{\partial^2 \Omega}{\partial z^2} = 0 \quad (\text{D.3})$$

and similarly the radial components of equation (D.1) are given by

$$-\frac{1}{r^2 \sigma_z} \frac{\partial^2 T_r}{\partial \theta^2} - \frac{1}{\sigma_\theta} \frac{\partial^2 T_r}{\partial z^2} + j\omega \mu_r \left(T_r - \frac{\partial \Omega}{\partial r} \right) = 0. \quad (\text{D.4})$$

Equations (D.3) and (D.4) together with the boundary conditions fully define the problem. These are the only two equations needed to solve for the two scalar unknowns T_r and Ω . Equation (D.1) does however yield two other equations. These are obtained by considering the circumferential and axial components of this equation. These two additional equations are automatically satisfied by the solution to equations (D.3) and (D.4). However, as a result of the physical condition $\sigma_r = 0$, they serve no practical purpose and thus have not been given consideration nor used in the Chapter 3. In fact, as shown in the Appendix E, some of the terms in these equations can be easily overlooked and if this happens, not surprisingly, they can lead to incorrect conclusions.

Due to the core geometry, periodicity in the circumferential direction must be satisfied.

Thus in general we can express T_r as

$$T_r = \sum_i T_{ci} \cos\left(i\frac{p\theta}{2}\right) + \sum_i T_{si} \sin\left(i\frac{p\theta}{2}\right) \quad (\text{D.5})$$

and Ω as

$$\Omega = \sum_i \Omega_{ci} \cos\left(i\frac{p\theta}{2}\right) + \sum_i \Omega_{si} \sin\left(i\frac{p\theta}{2}\right). \quad (\text{D.6})$$

Substituting expressions (D.5) and (D.6) into equations (D.3) and (D.4) leads to

$$\begin{aligned} & \sum_i \left[\frac{\mu_r}{r} \frac{\partial(rT_{ci})}{\partial r} - \mu_r \frac{\partial^2 \Omega_{ci}}{\partial r^2} - \frac{\mu_r}{r} \frac{\partial \Omega_{ci}}{\partial r} + \frac{\mu_\theta}{r^2} \left(i\frac{p}{2}\right)^2 \Omega_{ci} - \mu_z \frac{\partial^2 \Omega_{ci}}{\partial z^2} \right] \cos\left(i\frac{p\theta}{2}\right) + \\ & \sum_i \left[\frac{\mu_r}{r} \frac{\partial(rT_{si})}{\partial r} - \mu_r \frac{\partial^2 \Omega_{si}}{\partial r^2} - \frac{\mu_r}{r} \frac{\partial \Omega_{si}}{\partial r} + \frac{\mu_\theta}{r^2} \left(i\frac{p}{2}\right)^2 \Omega_{si} - \mu_z \frac{\partial^2 \Omega_{si}}{\partial z^2} \right] \sin\left(i\frac{p\theta}{2}\right) = 0 \end{aligned} \quad (\text{D.7})$$

and

$$\begin{aligned} & \sum_i \left[\frac{1}{r^2 \sigma_z} \left(i\frac{p}{2}\right)^2 T_{ci} - \frac{1}{\sigma_\theta} \frac{\partial^2 T_{ci}}{\partial z^2} + j\omega \mu_r \left(T_{ci} - \frac{\partial \Omega_{ci}}{\partial r}\right) \right] \cos\left(i\frac{p\theta}{2}\right) + \\ & \sum_i \left[\frac{1}{r^2 \sigma_z} \left(i\frac{p}{2}\right)^2 T_{si} - \frac{1}{\sigma_\theta} \frac{\partial^2 T_{si}}{\partial z^2} + j\omega \mu_r \left(T_{si} - \frac{\partial \Omega_{si}}{\partial r}\right) \right] \sin\left(i\frac{p\theta}{2}\right) = 0, \end{aligned} \quad (\text{D.8})$$

respectively. Since Fourier terms of one spatial frequency are orthogonal to Fourier terms of any other frequency, equations (D.7) and (D.8) may be split into an infinite number of equations. Each one of these equations corresponding to a particular spatial

frequency. In other words, for the n^{th} spatial harmonic we would have

$$\frac{\mu_r}{r} \frac{\partial (rT_{cn})}{\partial r} - \mu_r \frac{\partial^2 \Omega_{cn}}{\partial r^2} - \frac{\mu_r}{r} \frac{\partial \Omega_{cn}}{\partial r} + \frac{\mu_\theta}{r^2} \left(\frac{np}{2}\right)^2 \Omega_{cn} - \mu_z \frac{\partial^2 \Omega_{cn}}{\partial z^2} = 0 \quad (\text{D.9})$$

$$\frac{\mu_r}{r} \frac{\partial (rT_{sn})}{\partial r} - \mu_r \frac{\partial^2 \Omega_{sn}}{\partial r^2} - \frac{\mu_r}{r} \frac{\partial \Omega_{sn}}{\partial r} + \frac{\mu_\theta}{r^2} \left(\frac{np}{2}\right)^2 \Omega_{sn} - \mu_z \frac{\partial^2 \Omega_{sn}}{\partial z^2} = 0 \quad (\text{D.10})$$

$$\frac{1}{r^2 \sigma_z} \left(\frac{np}{2}\right)^2 T_{cn} - \frac{1}{\sigma_\theta} \frac{\partial^2 T_{cn}}{\partial z^2} + j\omega \mu_r \left(T_{cn} - \frac{\partial \Omega_{cn}}{\partial r}\right) = 0 \quad (\text{D.11})$$

$$\frac{1}{r^2 \sigma_z} \left(\frac{np}{2}\right)^2 T_{sn} - \frac{1}{\sigma_\theta} \frac{\partial^2 T_{sn}}{\partial z^2} + j\omega \mu_r \left(T_{sn} - \frac{\partial \Omega_{sn}}{\partial r}\right) = 0. \quad (\text{D.12})$$

A formal way of deriving equation (D.9) to (D.12) from equations (D.7) and (D.8) could be based on the following steps:

- 1) Multiply each term of equation (D.7) and (D.8) by $\cos\left(\frac{np\theta}{2}\right)$ (or $\sin\left(\frac{np\theta}{2}\right)$).
- 2) Integrate each of the resulting product terms over one spatial period.

Applying these steps results in only the coefficients of $\cos\left(\frac{np\theta}{2}\right)$ (or $\sin\left(\frac{np\theta}{2}\right)$) remaining to form equations (D.9), (D.10), (D.11) and (D.12). Equations (D.9) to (D.12) imply that each of the Fourier terms describing T_r or Ω can be solved separately. In addition to these equations we require known boundary conditions in order to fully define the problem. For the case presented in Chapter 3 the boundary conditions are:

- a) the normal derivative of Ω is zero at all the core boundaries except at $z = \delta$ where

$$\sum_i \frac{\partial}{\partial z} \left[\Omega_{ci} \cos\left(i\frac{p\theta}{2}\right) + \Omega_{si} \sin\left(i\frac{p\theta}{2}\right) \right] = \sum_i \left[B_{ci} \cos\left(i\frac{p\theta}{2}\right) + B_{si} \sin\left(i\frac{p\theta}{2}\right) \right] \quad (\text{D.13})$$

- b) at the flat boundaries of the core (i.e. at $z = 0$ and $z = \delta$)

$$J_z = \frac{\partial T_r}{\partial \theta} = 0 \quad (\text{D.14})$$

Equation (D.14) need not be considered as it does not contribute to the system excitation. Just as equations (D.7) and (D.8) were split into an infinite number of equations the same can be done with equation (D.13). For example, for the n^{th} spatial harmonic we have

$$\left. \frac{\partial \Omega_{cn}}{\partial z} \right|_{z=\delta} = B_{cn} \quad (\text{D.15})$$

and

$$\left. \frac{\partial \Omega_{sn}}{\partial z} \right|_{z=\delta} = B_{sn}. \quad (\text{D.16})$$

It is now clear that the solution for each harmonic component of T_r and Ω can be sought separately. In other words, the principle of superposition applies. For example, to solve for T_{s7} and Ω_{s7} we would use

$$\frac{\mu_r}{r} \frac{\partial (rT_{s7})}{\partial r} - \mu_r \frac{\partial^2 \Omega_{s7}}{\partial r^2} - \frac{\mu_r}{r} \frac{\partial \Omega_{s7}}{\partial r} + \frac{\mu\theta}{r^2} \left(\frac{7p}{2} \right)^2 \Omega_{s7} - \mu_z \frac{\partial^2 \Omega_{s7}}{\partial z^2} = 0 \quad (\text{D.17})$$

and

$$\frac{1}{r^2 \sigma_z} \left(\frac{7p}{2} \right)^2 T_{s7} - \frac{1}{\sigma_\theta} \frac{\partial^2 T_{s7}}{\partial z^2} + j\omega \mu_r \left(T_{s7} - \frac{\partial \Omega_{s7}}{\partial r} \right) = 0. \quad (\text{D.18})$$

with boundary conditions

$$\left. \frac{\partial T_{s7}}{\partial \theta} \right|_{z=0} = \left. \frac{\partial T_{s7}}{\partial \theta} \right|_{z=\delta} = 0 \quad (\text{D.19})$$

and

$$\left. \frac{\partial \Omega_{s7}}{\partial z} \right|_{z=\delta} = B_{s7}. \quad (\text{D.20})$$

However, in the case presented in Chapter 3, $B_{s7} = B_{c7} = 0$. Thus we can conclude that there is no seventh harmonic component in T_r or Ω . Since only the spatial fundamental component of the flux density is present in the imposed boundary condition, the above arguments prove that there can only be spatial fundamental components present in T_r and Ω . In other words, the system is linear and therefore only those spatial harmonics present in the excitation will appear in T_r and Ω . It should also be noted that the above arguments also prove that T_r and Ω are in spatial phase with the excitation. That is T_r and Ω reach their respective peak values at the same value of θ at which the excitation reaches its peak value.

Appendix E

The Circumferential and Axial Components of:

$$\nabla \times \sigma^{-1} \nabla \times \vec{T} = -j\omega \left[\mu \left(\vec{T} \times \nabla \Omega \right) \right]$$

The vector equation

$$\nabla \times \left(\sigma^{-1} \nabla \times \vec{T} \right) = -j\omega \left[\mu \left(\vec{T} \times \nabla \Omega \right) \right] \quad (\text{E.1})$$

when expanded and resolved into its coordinate components yields three scalar partial differential equations. These being

$$\frac{1}{r^2 \sigma_z} \frac{\partial^2 r T_\theta}{\partial \theta \partial z} - \frac{1}{r^2 \sigma_z} \frac{\partial^2 T_r}{\partial \theta^2} - \frac{1}{\sigma_\theta} \frac{\partial^2 T_r}{\partial z^2} + \frac{1}{\sigma_\theta} \frac{\partial^2 T_z}{\partial z \partial r} = -j\omega \mu_r \left(T_r - \frac{\partial \Omega}{\partial r} \right) \quad (\text{E.2})$$

$$\begin{aligned} \frac{1}{r \sigma_r} \frac{\partial^2 T_z}{\partial z \partial \theta} - \frac{1}{\sigma_r} \frac{\partial^2 T_\theta}{\partial z^2} - \frac{1}{r \sigma_z} \frac{\partial^2 r T_\theta}{\partial r^2} + \frac{1}{r^2 \sigma_z} \frac{\partial r T_\theta}{\partial r} + \\ \frac{1}{r \sigma_z} \frac{\partial^2 T_r}{\partial r \partial \theta} - \frac{1}{r^2 \sigma_z} \frac{\partial T_r}{\partial \theta} = -j\omega \mu_\theta \left(T_\theta - \frac{1}{r} \frac{\partial \Omega}{\partial \theta} \right) \end{aligned} \quad (\text{E.3})$$

$$\begin{aligned} \frac{1}{\sigma_\theta} \frac{\partial^2 T_r}{\partial r \partial z} + \frac{1}{r \sigma_\theta} \frac{\partial T_r}{\partial z} - \frac{1}{\sigma_\theta} \frac{\partial^2 T_z}{\partial r^2} - \frac{1}{r \sigma_\theta} \frac{\partial T_z}{\partial r} - \\ \frac{1}{r^2 \sigma_r} \frac{\partial^2 T_z}{\partial \theta^2} + \frac{1}{r \sigma_r} \frac{\partial^2 T_\theta}{\partial \theta \partial z} = -j\omega \mu_z \left(T_z - \frac{\partial \Omega}{\partial z} \right). \end{aligned} \quad (\text{E.4})$$

For $\vec{T} = (T_r, 0, 0)$ and $\sigma_r = 0$ some of the terms in equations (E.2), (E.3) and (E.4) will become equal to zero. However, as will be shown, one must be cautious when neglecting terms.

In Chapter 3 we used

$$-\frac{1}{r^2 \sigma_z} \frac{\partial^2 T_r}{\partial \theta^2} - \frac{1}{\sigma_\theta} \frac{\partial^2 T_r}{\partial z^2} + j\omega \mu_r \left(T_r - \frac{\partial \Omega}{\partial r} \right) = 0 \quad (\text{E.5})$$

together with

$$\frac{\mu_r}{r} \frac{\partial (r T_r)}{\partial r} - \mu_r \frac{\partial^2 \Omega}{\partial r^2} - \frac{\mu_r}{r} \frac{\partial \Omega}{\partial r} - \frac{\mu_\theta}{r^2} \frac{\partial^2 \Omega}{\partial \theta^2} - \mu_z \frac{\partial^2 \Omega}{\partial z^2} = 0 \quad (\text{E.6})$$

to find the solution for T_r and Ω . The two other scalar partial differential equations yielded from equation (E.1) are given in (E.3) and (E.4). Removing those terms equal to zero reduces these equations to

$$\frac{1}{r \sigma_z} \frac{\partial^2 T_r}{\partial r \partial \theta} - \frac{1}{r^2 \sigma_z} \frac{\partial T_r}{\partial \theta} - j\omega \frac{\mu_\theta}{r} \frac{\partial \Omega}{\partial \theta} + \lim_{\sigma_r \rightarrow 0} \left[\frac{1}{r \sigma_r} \frac{\partial^2 T_z}{\partial z \partial \theta} - \frac{1}{\sigma_r} \frac{\partial^2 T_\theta}{\partial z^2} \right] = 0 \quad (\text{E.7})$$

and

$$\frac{1}{\sigma_\theta} \frac{\partial^2 T_r}{\partial r \partial z} + \frac{1}{r \sigma_\theta} \frac{\partial T_r}{\partial z} - j\omega \mu_z \frac{\partial \Omega}{\partial z} + \lim_{\sigma_r \rightarrow 0} \left[\frac{1}{r \sigma_r} \frac{\partial^2 T_\theta}{\partial \theta \partial z} - \frac{1}{r^2 \sigma_r} \frac{\partial^2 T_z}{\partial \theta^2} \right] = 0, \quad (\text{E.8})$$

respectively. It is quite easy to overlook the limit terms of equations (E.7) and (E.8). This is because T_θ and T_z are taken to be equal to zero implying that their derivatives are also equal to zero. It is also easy to make the wrong assumption that any product which contains the derivatives of T_θ or T_z is equal to zero. But a derivative of T_θ or T_z when multiplied by $1/\sigma_r$ may result in a non-zero-value and in the case of equations (E.7) and (E.8) this is exactly what happens.

Equations (E.5) and (E.6) are sufficient to find solutions for T_r and Ω . Once T_r and Ω are found, they can be substituted into equations (E.7) and (E.8) to evaluate the limit terms of these equations. Generally then, these terms will have non-zero values and thus equations (E.7) and (E.8) are automatically satisfied. It is important not to ignore the limit terms of equations (E.7) and (E.8) if those equations are to be used. Failure to include them will result in erroneous conclusions.

As was shown in Chapter 3, equations (E.5), (E.7) and (E.8) are electrical loop equations. Each of the terms in these equations represent a resistive branch voltage (per m) or and electromagnetically induced EMF (per m). In the case of equation (E.5) the plane in which the loop lies is in the radial direction. In the case of equation (E.7) the plane in which the loop lies is in the circumferential direction. In the case of equation (E.8) the plane in which the loop lies is in the axial direction.

A physical interpretation for the limit terms in equations (E.7) and (E.8) can be based on the idea that these equations are loop equations. In equation (E.5) all the branch voltage terms relate to voltages across branches of finite resistance. In equations (E.7) and (E.8) all the branch voltage terms relate to the voltage across branches of finite resistance, except for the limit terms. The loops represented by equation (E.7) and (E.8) contain open-circuits because σ_r is equal to zero. Therefore these loops contain branches whose resistance is infinite. The limit term in each of equations (E.7) and (E.8) represent the sum of the voltages across the open-circuit branches forming part of their respective loops.

Appendix F

Published Papers

The following publications were produced as part of this work;

- A. J. Hewitt, A. Ahfock and S. A. Suslov, “Magnetic flux density distribution in axial flux machine cores,” *IEE Proceedings - Electric Power Applications*, Vol. 152, No. 2, March 2005, pp 292-296.
- A. Hewitt and A. Ahfock, “Sub-domain scaling for finite element analysis of electrical machines,” *IEE Proceedings - Electric Power Applications*, Vol. 152, No. 2, March 2005, pp 149-156.
- A. Ahfock and A. Hewitt, “Curvature related eddy current losses in laminated axial flux machine cores,” *IEE Proceedings - Electric Power Applications*, Vol. 152, No. 5, September 2005, pp 1350-1358.

These papers can be accessed online through the Institute of Electrical Engineers (IEE) web site (<http://www.ieedl.org/IP-EPA>).